Design, Fabrication, and Validation of a Highly Miniaturized Wirelessly Powered Neural Implant

by

Adam Khalifa

A dissertation submitted to The Johns Hopkins University
in conformity with the requirements for the degree of
Doctor of Philosophy

Baltimore, Maryland
February, 2019

Abstract

We have recently witnessed an explosion in the number of neurons that can be recorded and/or stimulated simultaneously during neurophysiological experiments. Experiments have progressed from recording or stimulation with a single electrode to Micro-Electrode Array (MEA) such as the Utah Array. These MEAs can be instrumented with current drivers, neural amplifiers, digitizers and wireless communication links. The broad interest in these MEAs suggests that there is a need for large scale neural recording and stimulation. The ultimate goal is to coordinate the recordings and stimulation of potentially thousands of neurons from many brain areas. Unfortunately, current state-of-the-art MEAs are limited by their scalability and long-term stability because of their physical size and rigid configuration. Furthermore, some applications prioritize a distributed neural interface over one that offers high resolution. Examples of biomedical applications that necessitate an interface with neurons from many sites in the brain include: *i)* understanding and treating neurological disorders that affect distributed locations throughout the CNS; *ii)* revolutionizing our understanding of the brain by studying the correlations between neural networks from different regions of the brain and the mechanisms of cognitive functions; and *iii)* covering larger area in the sensorimotor cortex of amputees to more accurately control robotic prosthetic limbs or better evoke a sense of touch.

One solution to make large scale, fully specifiable, electrical stimulation and recording possible, is to disconnect the electrodes from the base, so that they can be arbitrarily placed, using a syringe, freely in the nervous system. To overcome the challenges of system miniaturization, we propose the “microbead”, an ultra-small neural stimulating implant, that is currently implemented in a 130nm CMOS technology with the following characteristics: 200 µm × 200 µm × 80 µm size; optimized wireless powering, all micro-electronics on single chip; and integrated electrodes and coil. The stimulating microbead is validated in a sciatic nerve by generating leg movements. A recording microbead is also investigated with following characteristics: wireless powering using steerable phased coil array, miniaturized front-end, and backscattering telemetry. These microbeads could eventually replace the rigid arrays that are currently the state-of-the-art in electrophysiology set-ups.

Primary Reader: Dr. Ralph Etienne-Cummings, Johns Hopkins University

Secondary Reader: Dr. Andreas Andreou, Johns Hopkins University

Acknowledgement

Foremost, I would like to thank my advisor, Dr. Ralph Etienne-Cummings, for his patient and generous supervision. He gave me the priceless opportunity to be an independent researcher pursuing various interdisciplinary tasks. While challenging me to push my limits, Ralph has always been open to my innovative and risky ideas. He has been an example mentor that I want to be.

I am also deeply indebted to my labmates, Jamal Molin, Jack Zhang, John Rattray, Adebayo Eisape, Tao Xiong, Sherry Chiu, Martina Leistner, and Chetan Thakur, who are always willing to share their knowledge and experience. They are part of the greatest memories I formed during my stay at JHU.

I would like to extend my appreciation to Dr. Andreas Andreou and his lab for their help and for sharing their tools with me, and Dr. Philippe Pouliquen, the person who always had an answer to my difficult questions.

In the in-vivo experiments, I thank my collaborators, Dr. Nitish Thakor and Dr. Qihong Wang for their guidance in the rat experiments. A special thanks must be given to Dr.

Milutin Stanacevic and his student Yasha Karimi who both provided invaluable insight in the development of a wireless system. I am also grateful to Milad Alemohamed who has helped me in my work in various ways.

And finally, I thank my family (Sonia, Mohamed, and Yassine). Their encouragements and support were instrumental for my Ph.D. study. I want to thank my better-half, Dr. Faiza Rahim for giving me endless love and support.

Contents

List of Tables

List of Figures

Chapter 1

Introduction

1.1 Neural interfacing Applications and Methods

Neuromodulation started with Galvani's electrical stimulation experiments in 1780. Today, deep brain stimulation (DBS) is often relied upon to treat neurological disorders [1], cochlear implants widely utilized to restore hearing [2] and pacemakers implanted to help control abnormal heart rhythms. Neural recording has also gone a long way since the discovery that the nervous system has electrical properties. It is now an important method for understanding the mechanisms and functions of the nervous system. Furthermore, combined with neural stimulation, electrical recording helps improve the efficacy and power efficiency of DBS devices. The neural stimulation and recording applications that are most commonly used today are shown in Table 1.1. As can be noticed from the table, many of

Table 1.1: Neural stimulation and recording applications

Neural interface	Application	Area
Stimulation	Restoration of movement	**Cortex** / Spinal cord / Peripheral nerve
	Restoration of touch	**Cortex** / Spinal cord / Peripheral nerve
	Restoration of sight	**Cortex** / Retina
	Restoration of hearing / balance	Cochlea
	Regulation of heart rate, depression, insulin secretion	Vagus nerve
	Understanding and treating neurological disorders	**Cortex / Sub-cortex / Cerebellum**
Recording	Understanding and treating neurological disorders	**Cortex / Sub-cortex / Cerebellum**
	Understanding the mechanisms of cognitive functions	**Cortex / Sub-cortex / Cerebellum**
	Control of prosthetic limbs	**Cortex** / Spinal cord / Peripheral nerve

the applications are only possible when interfacing directly with the brain. This leads to the question, what are the different methods of interfacing with neurons in the brain?

Neural activity can be recorded using non-invasive and invasive methods. The biggest examples of non-invasive methods are functional magnetic resonance imaging (fMRI) and electroencephalography (EEG). fMRI provides an average spatial resolution (1-3 mm) and a poor temporal resolution (1-10 s). EEG has a better temporal resolution, but due to the filtering effect of the skull, has a very limited spatial resolution (1-10 cm). fMRI relies on an MRI machine and stationary user, while EEG electrode can be easily worn without constricting the user. Invasive methods involve placing electrodes in or on brain tissue. ECoG achieves better resolution than EEG by placing the electrode within a few mm of the neurons, but still provides an aggregate population level recording like EEG. At the present moment, the direct recording or initiation of action potentials (APs) of a single neuron can only be done using extracellular or intracellular interface. Although it is the most invasive technique, it covers significantly more applications than any other neural interfacing technique. Indeed, implantable medical devices (IMDs) that can electrically stimulate neurons and record extracellular neural activities in the central nervous system (CNS) play a crucial role in today's neuroscience and neuro-prosthetic field [3]. For this reason, the work presented in this thesis relies on invasive neural interfacing methods.

1.2 Motivation

1.2.1 The Need for Wirelessly-Powered Neural Interfaces

To reduce the risk of infection caused by percutaneous wired connections to the IMD, a battery can be integrated with the system. However, this leads to periodic surgeries to carry out the replacement of the discharged battery. Thus, an alternative solution is to use a wireless powering system. Examples of recent wirelessly-powered brain implants [4, 5, 6, 7] are shown in Fig. 1.1. Remotely-powered IMDs that enables safer and smaller neural interfaces are especially useful to freely moving animals and human subjects. Even more so for chronic applications since rigid tethered electrodes suffer from micromotion, which results in tissue inflammation and scar formation (caused by astrogliosis) around the electrodes [8, 9, 10]. Tissue damage can be alleviated by using flexible electrodes, however, these types of electrodes are often not stiff enough to pierce brain tissue on their own.

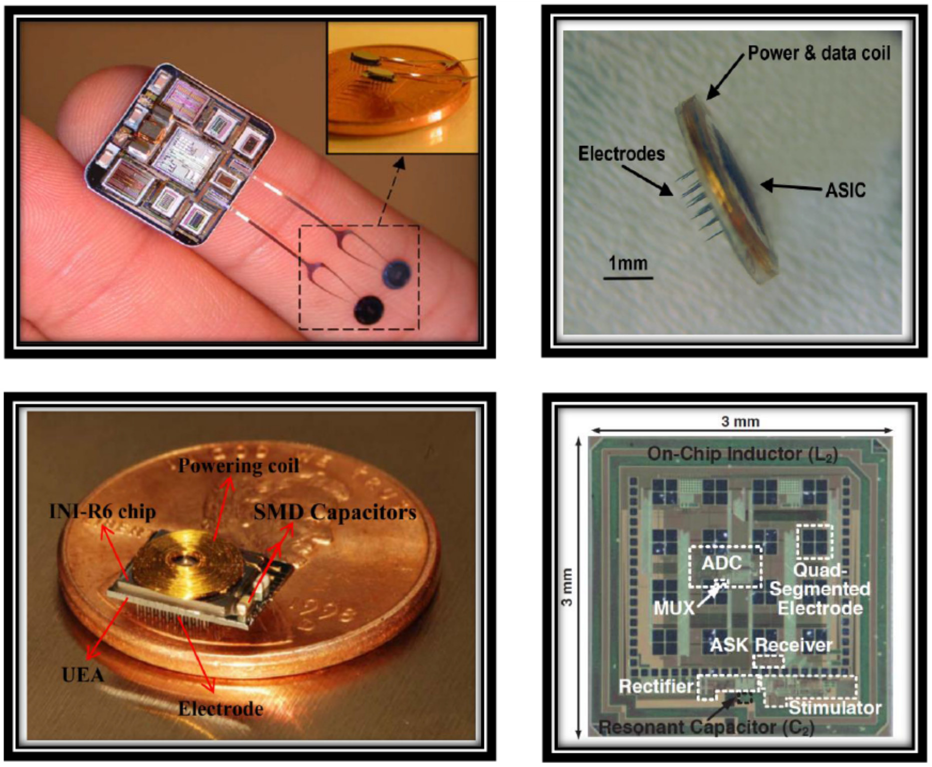

Figure 1.1: State-of-the-art wirelessly-powered brain implants.

1.2.2 The Need for Single-Channel Free-Floating Neural Interfaces

The importance of investigating population codes played a major role in the development of multielectrode arrays (MEA) [11]. Currently, the MEA most commonly employed is the Utah array. It consists of up to 100 silicon needles all of which are connected to a rigid base to form an electrode array. The spacing between the needles can vary, but is on a grid, separated by hundreds of micrometers. However, the majority of currently available MEA designs share significant shortcomings:

1. Limits on recording/stimulation configuration and location: MEAs offer high-resolution but localized coverage of the cerebral cortex, thus a single MEA can't be used to record/stimulate multiple regions. Regarding applications with large mammals (including humans) with folded cortices, MEAs are not easily inserted between the folds and ridges of the brain surface. Furthermore, if the MEA is integrated into a wirelessly powered implant and successfully placed between the folds of the cortex, then a large rotational misalignment would occur, leading to a significant decrease in power transfer efficiency.

2. Limits on long-term stability [12, 13]: The longevity of high-density rigid MEAs is not as high as what neuroscientists and clinicians would have hoped for. MEAs, even when not tethered, can cause strain and micromotions.

3. Limit on density: As the number of electrodes increases on a single chip, the routing of signals from the current sources to the electrode becomes increasingly difficult. Furthermore, high densities MEA suffer from signal crosstalk.

Most of the fabricated wirelessly-powered implants rely on MEAs for a high spatiotemporal resolution interface with the brain [14, 5, 15, 6, 4]. However, some applications prioritize a distributed neural interface over one that offers high resolution. MEAs are bulky and too invasive to be implanted in multiple regions of the brain. Examples of biomedical applications that necessitate an interface with neurons from many sites in the brain include:

1. Revolutionizing our understanding of the brain by studying the correlations between neural networks from different regions of the brain and the mechanisms of cognitive functions (e.g., memory, emotions, perception, reasoning, etc.) [16, 17]. Early on, it was shown that the neural codes underlying behavior cannot be explained by the responses of single cortical neurons, but instead rely on the population activity across multiple neurons. The power of recording and stimulating from multiple electrodes lies not only in the increased yield in the number of neurons that can be studied but also in that it allows for the investigation of temporal interactions between neurons. These interactions include spike count correlations or spike synchrony codes that have been shown to convey significant information about how the nervous system binds and links information between and across cortical regions [18].

2. Understanding and treating neurological disorders that affect distributed locations throughout the CNS (Alzheimer, epilepsy, Pick's disease, etc.) [19]. Diseases of the brain are complex and can progressively affect multiple parts of the nervous system.

3. Covering a larger area in the sensorimotor cortex of amputees to more accurately control robotic prosthetic limbs (e.g., finer motor control of the individual fingers) or better evoke a sense of touch [20]. The movement of a limb is the result of complex activities in the brain, and thus a large number of stimulating electrodes is needed at different locations in order to activate the brain in patterns that mimic natural activation.

Getting rid of the centralized and anchored MEA base results in free-floating electrodes that substantially increase the anatomical locations for recording/stimulation. These single-channel implants trade lower spatial resolution for more cortical coverage and can thus be placed anywhere in the brain allowing clinicians and researchers to be more specific in their treatments or experiments. Examples of such devices are shown in the following section.

1.3 Prior work

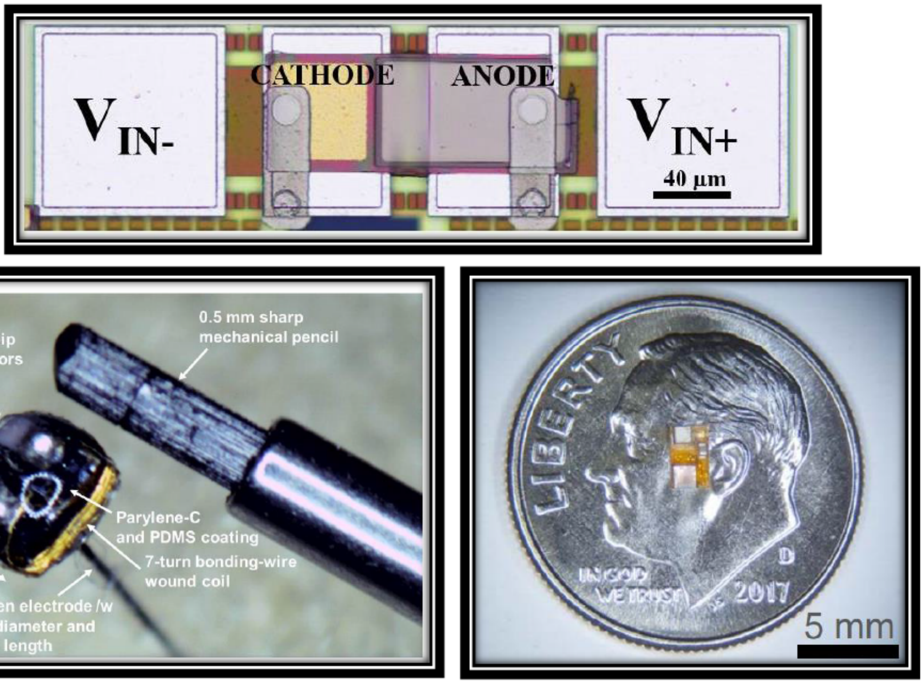

Figure 1.2: State-of-the-art single channel wirelessly-powered neural implants.

Some researchers have demonstrated wirelessly-powered single-channel implants [21, 22, 23, 24, 25, 26, 27] that have the potential to be scattered all over the brain (Fig. 1.2).

The “Neural Dust” [28], tries to offer a solution to the problem of interfacing large neural populations at different areas of the brain. The group has successful shown neural recordings in the peripheral nervous system by utilizing ultrasonic technology for powering and communications. However, even with the use of extremely small crystals, their current prototype remains bulky (2.4 mm^3), and thus remains too invasive as a great number of Neural Dust sensors needs to be surgically implanted into the CNS. The same is true for the StimDust (2.2 mm^3) [29], which is a stimulating mote version of the Neural dust.

By placing the implant approximately one wavelength away from the source, the IMD can be powered in the midfield region. In [22], this region has been fully exploited in order to surpass the challenges of near-field wireless powering. Furthermore, the authors developed a patterned metal plate to focus the output field to dimensions smaller than the vacuum wavelength. To experimentally validate the power transfer efficiency, the implant was implanted in the brain and placed 5.5 cm away from the source. Although the large source-receiver distance achieved by midfield powering is promising, the device has yet to be miniaturized down to scales useful to applications requiring distributed brain interface.

Another example of next-generation instrumented micro-electrode is the microscale opto-electrically transduced electrode (MOTE) [26]. With the use of its integrated AlGaAs diode that functions as both a photovoltaic and light emitting diode, the MOTE is powered by an optical interface which is also used to communicate recorded neural signals. Although the ultra-low power MOTE is considered to be one of the smallest IMDs (i.e, 250 µm × 57 µm) to date, the optical interface prevents it from being implanted deep in tissue, moreover, the MOTE is unlikely to work when powered through the skull which severely limits its usefulness for the majority of neuroscience and neuroprosthetic applications.

A good example of a miniaturized IMD that can be powered at practical depths is the free-floating wireless implantable neural recording system (FF-WINeR) by [30]. The FF-WiNeR utilizes a four-coil inductive link for back telemetry, shared with a three-coil link for wireless power transmission. Unfortunately, the surgical invasiveness has to be significantly increased in order to implant one of the large coils below the dura (almost in the same plane with FF-WINeR). Furthermore, the prototype is still too big (i.e, >1 mm^3) to be fully implanted into a dense brain at different desired depths. Tissue damage is minimized by only having the tungsten electrode penetrate the cortex, but this makes the system less attractive as it does not offer the freedom to choose between different depths.

The above examples demonstrate tremendous progress in developing the next generation instrumented micro-electrode but requires further miniaturization in order to truly become practical in the neuroscience and neuro-prosthetic field. Continued miniaturization would allow: *i)* more of these floating IMDs to be inserted into the brain, *ii)* more precision when targeting specific brain regions, *iii)* compatibility with minimally invasive implantation procedures, and *iv)* a reduction in the body's foreign response [31, 32]. Unfortunately, even with the recent developments in integration and fabrication technologies, several factors such as the ASIC chip, the wireless link, and the assembly/packaging, still limit the extent of miniaturization of the implant.

1.4 Research Objectives

To address the need for a smaller distributed free-floating neural interface, we propose the next generation of IMDs, which we call the "microbead" (Fig. 1.3). The ultra-compact neural implant includes everything it needs (electrodes, coil, circuitry) on a single silicon chip.

The near-future vision of this work is to be able to implant hundreds of stable microbeads (with a volume of 0.0018 mm^3) in the CNS, providing a revolutionary neural interfacing tool for neuroscientists and clinicians. Furthermore, these disparately placed recording and stimulation electrodes can be synchronized to provide mechanisms for closed-loop experimentation. To alleviate the surgical challenges currently faced while implanting MEAs, the microbead is miniaturized to enable direct injection into the target brain region via a syringe needle with an inner diameter of 0.4 mm. The presented work in this thesis is to be seen as the initial steps taken in achieving these goals.

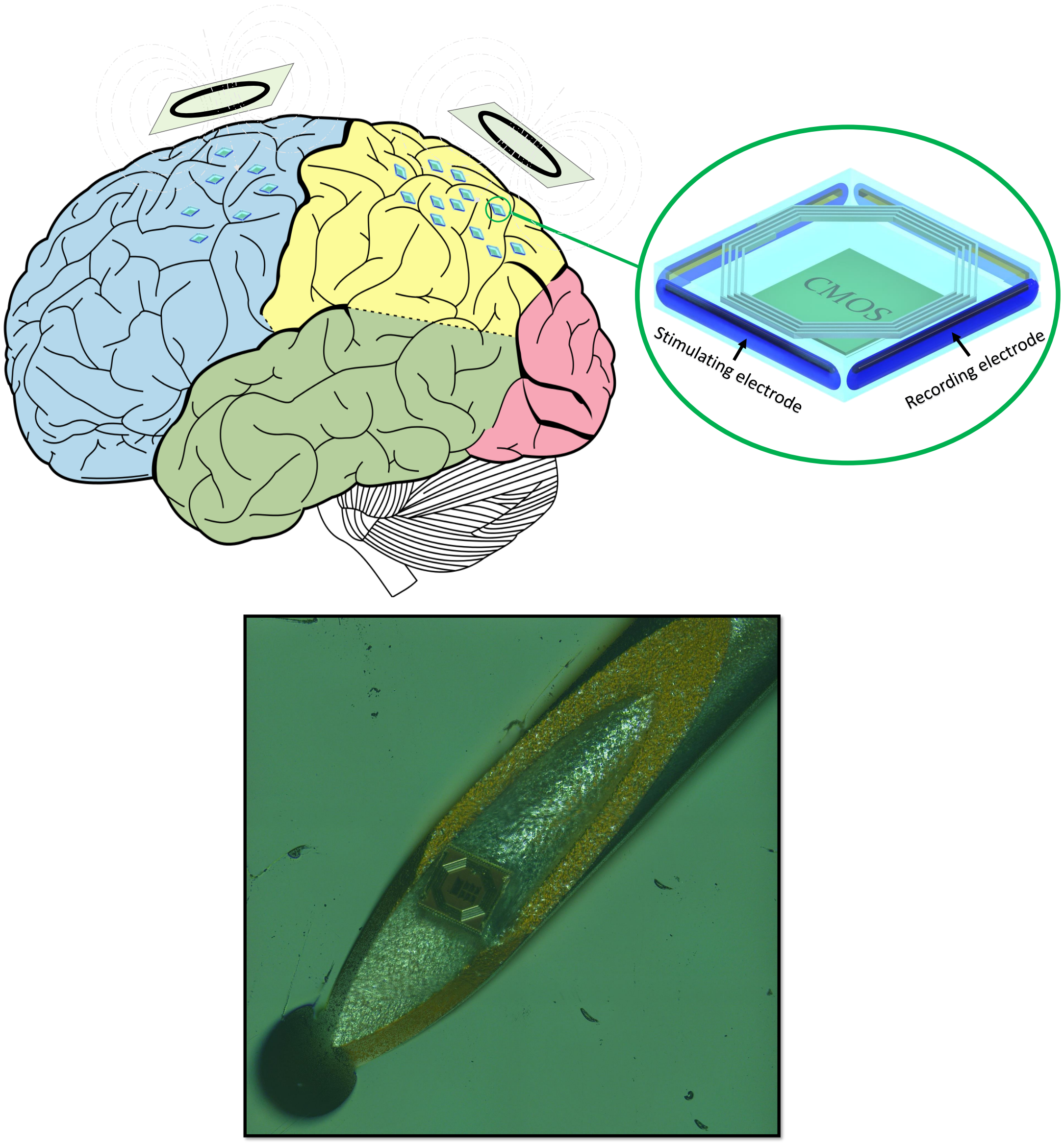

Figure 1.3: (Top) A drawing of scattered microbeads in the cerebral cortex, and the planned packaged wirelessly powered microbead with two electrodes for stimulation and two for recording. (Bottom) A micrograph of the microbead which can be entirely implanted into the brain by means of a syringe with a 22G needle.

1.5 Contributions

The work described in this thesis has led to the design, fabrication, and validation of the smallest stimulating IMD to date. The challenges of further miniaturization are tackled by:

1. **Simplifying the system architecture to lower the area and power consumption of the implant (Fig. 1.4) [33, 34]**. Innovative designs have been used at the circuit and system level. Many of the digital and analog blocks that are normally found in a conventional system architecture have been discarded (e.g, dedicated resonating capacitor, demodulator, digital controller, dedicated filtering block, and antenna) while still maintaining control over the microbead.

2. **Optimizing the power efficiency at every stage (Fig. 1.5) [35, 36, 37]**. Since the harvested power is scarce for ultra-small receiver (Rx) coils, power efficiencies that are found in every stage of the design process have to be maximized. Novel design procedures have been implemented that leads to the quick design a highly optimized 2-coil wireless link. Furthermore, a Tx coil array has been designed to allow beamforming in the near-field and achieves better power efficiencies compared to a 2-coil wireless link.

3. **Fully exploiting IC technology to avoid conventional bulky assembly methods [38, 34].** A standalone silicon chip that integrates an on-chip Rx coil and an electrode pair, has been fabricated and validated in animal experiments. This is the result of a

completely novel process flow that allows the CMOS chip to keep its initial volume after post-processing (needed for packaging and assembly).

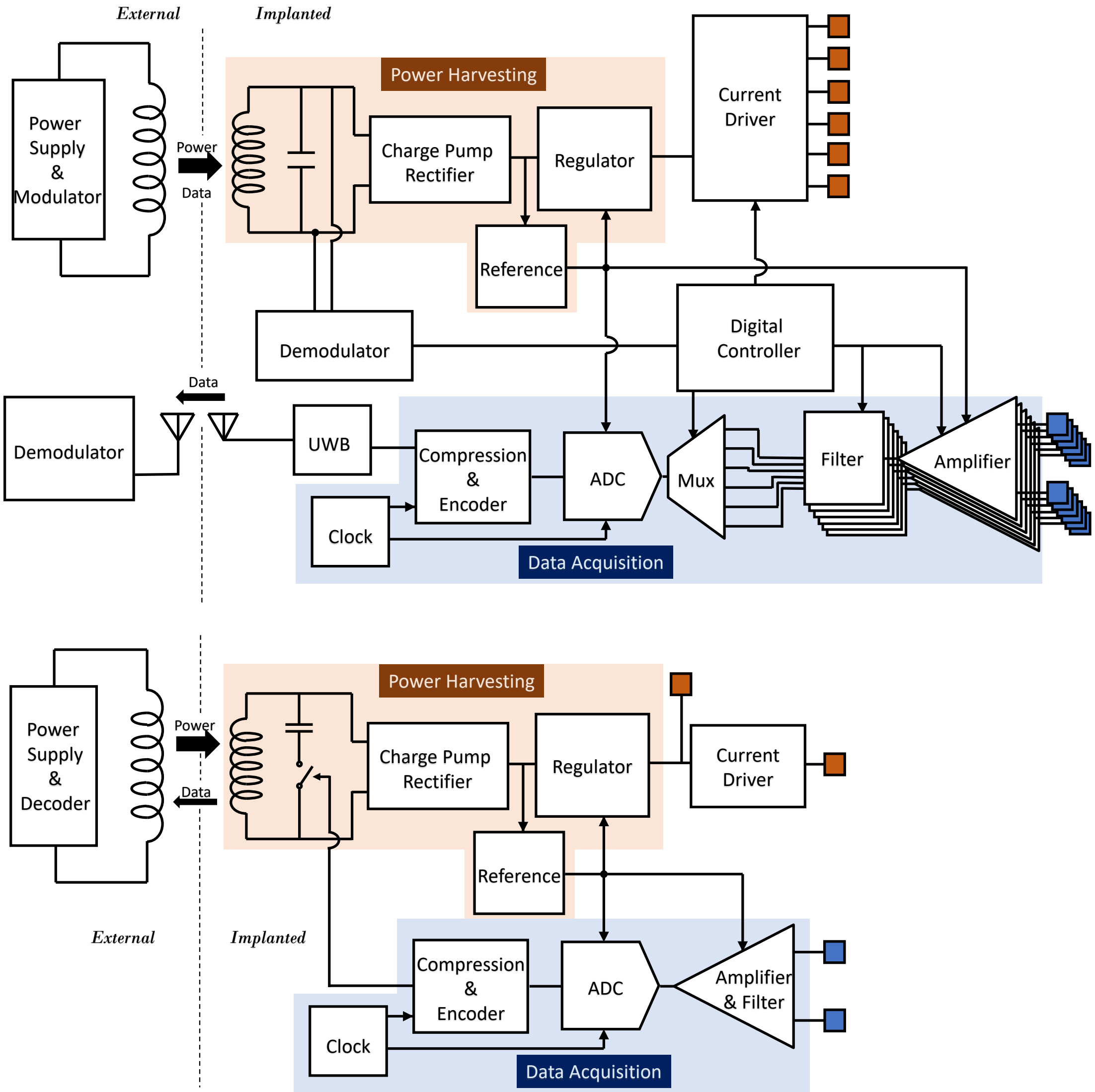

Figure 1.4: Drawing of the system architecture of a (top) conventional neural and stimulating wireless device, and (bottom) that of the microbead.

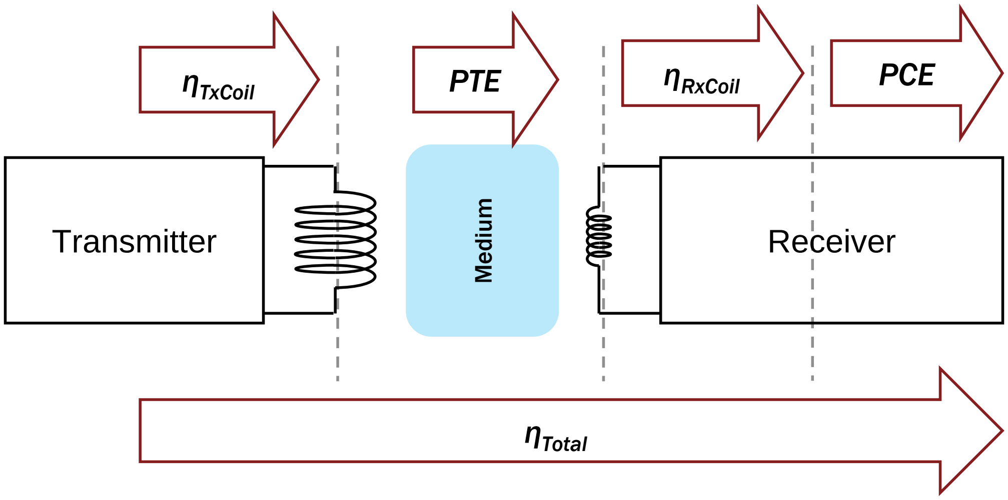

Figure 1.5: Power efficiencies at different stages of the wireless system.

1.6 Dissertation outline

The rest of the thesis is organized as follows. Chapter 2 introduces the wireless powering system. It provides the optimization design flow used to fabricate the transmitter and receiver coils, along with the challenges encountered when designing an on-chip silicon coil. Chapter 3 presents the harvesting system and the methods used to miniaturize the circuitry. The system architecture is explained and its efficiency characterized. Chapter 4 shows a proof-of-concept of an ultra-small IMD by describing the design and fabrication methods of a stimulating microbead. The electrode incorporation is described and the *in-vivo* experimental results are presented. Chapter 5 extends the work of Chapter 4 by providing details on a recording microbead and a phased transmitter coil array used to improve the power transfer efficiency of the wireless link. Finally, Chapter 6 concludes the thesis and important improvements that can made to the current prototype in the near future are discussed.

Chapter 2

Wireless Energy Transfer using µm-scale coils

This section includes details on the design and optimization of the printed circuit board (PCB) and on-silicon coil. Due to low capture efficiency of the applied fields by the implant's tiny cross-section, maximizing the power transfer efficiency (PTE) is critical and requires the careful design of the Tx and Rx coil.

2.1 Wireless powering techniques

The performance of the different wireless power transfer methods has been well summarized in [10] and is shown in Fig. 2.1. There are three methods currently used to energize implants wirelessly: light, electromagnetic wave (EM) and ultrasound (US). The most popular means to power IMDs is acoustic powering and magnetic powering in the near and midfield. Other types of energy harvesting systems such also exists [39, 40] but do not provide sufficient power to tiny stimulating IMDs.

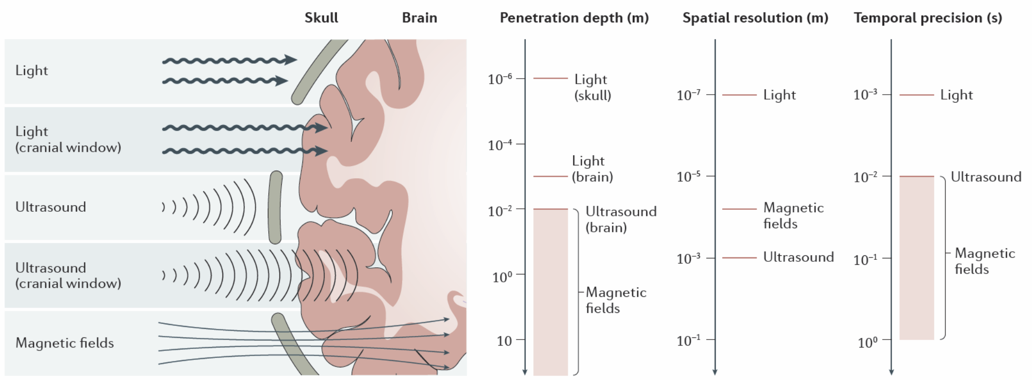

Figure 2.1: Performance comparison of different wireless powering techniques to energize implants in the central nervous system.

Acoustic waves are increasingly being investigated as a method for delivering power to miniaturized neural interfaces [41, 21]. The main advantage of ultrasonic wireless power transfer is the slow speed of propagation of the pressure wave, which makes it easier to focus on mm-sized spots in the tissue. However, severe limitations also exist. For instance, there is a significant mismatch between the acoustic impedance of piezoelectric material and tissue [42]. The boundary causes reflections, which deteriorates the energy coupling efficiency. Furthermore, bone has a very high attenuation coefficient to ultrasonic beams. An RF powered interrogator placed beneath the skull can alleviate the issue but adds complexity making the implantable device not truly wireless without the additional RF link.

Therefore, the most practical and efficient method to power IMDs at short ranges (<5 cm) and through the skull remains the resonating near/mid-field powering.

Inductive coupling has been used for several decades in RFID, biomedical, and industrial applications. In the biomedical field, it was first used to charge an artificial heart in 1961. Inductive coupling often involves two coils that are referred to as the transmitter (or primary) and receiver (or secondary) coils, but the concept can be also demonstrated using two wires. Two wires are inductively coupled when a change in current through one induces a voltage across the ends of the other wire. Inductive coupling can be proven using the following two equations:

- Ampère's circuital law (with Maxwell's addition) relates the magnetic field around a closed loop to the electric current passing through the loop:

$$\vec{\nabla} \times \vec{H} = \frac{\partial \vec{D}}{\partial t} + \vec{J}$$

where, $\vec{H}$ is the magnetic field strength, $\vec{D}$ is the electric displacement, and $\vec{J}$ the free electric current density.

- Maxwell–Faraday equation (also known as Faraday's law of induction) describes the fact that time-varying magnetic fields induce electric fields:

$$\vec{\nabla} \times \vec{E} = -\frac{\partial \vec{B}}{\partial t}$$

where, $\vec{E}$ is the electric field strength, and $\vec{B}$ the magnetic flux density.

Depending on the distance between the transmit and receive coils, only a fraction of the magnetic flux generated by the Tx coil penetrates the Rx coil and contributes to the power transmission. The more flux reaches the Rx, the better the coils are coupled. Since the microbead's coil is much smaller than the Tx coil, the link is termed a "loosely coupled system". Systems with a low coupling coefficient need a resonant Tx and Rx to improve the power transfer efficiency. This leads to the question, what is the optimal resonating frequency that leads to the largest PTE?

2.2 Operating frequency and Rx selectivity

Resonance occurs when the reactance of the inductor cancels with the reactance of the capacitor in a resonant tank circuit. This occurs at a certain frequency known as the resonant frequency $\mathrm{f_{res}}$.

The Tx and Rx coil both have the same resonant frequency which is given by:

$$f_{res} = \frac{1}{\sqrt{2\pi LC}}$$

It is important to remember that when a load is connected to the LC tank, the relationship remains the same for a series tank but changes for a parallel tank and becomes:

$$f = \sqrt{\frac{1}{2\pi LC} - \frac{1}{R^2C^2}}$$

The operating frequency has to be selected carefully as it is one of the most important design parameters for the wireless link. The majority of remotely-powered implants operate in the MHz range to minimize the dielectric loss in tissue. However, resonating at low frequencies requires a large capacitor which increases the size of the microbead. Therefore, two frequency limits have been set, one being 400 MHz so as to not impact the volume of the implant, and the other 3 GHz in order to keep losses in tissue to a manageable level.

The majority of biomedical applications require addressability of multiple different stimulating/recording sites. In this work, this is achieved by assigning a specific resonating capacitance to each microbead making the implants individually addressable like in a frequency division multiple access (FDMA) system. With 250 MHz spacing between the resonant frequencies, each Tx coil can individually control up to 10 different microbeads within a transmission frequency range of 0.5 GHz to 3 GHz. As shown in Fig. 2.2, less than 250 MHz spacing causes the microbeads to interfere with each other as shown in the simulated regulated voltage response of different resonating microbeads to an AC analysis. Two microbeads resonating at different frequencies (1.25 and 1.5 GHz) were individually selected to demonstrate the idea. They were wirebonded onto a PCB and wirelessly powered through tissue. The center of the Tx coil was placed in the middle of two dies in order to create a lateral misalignment of 2 mm for each of the Rx coils. This was done to simultaneously measure the voltage generated by both microbeads while the power transmitting frequency toggled between the two resonant frequencies. As shown in Table 2.1, the difference between the generated voltages are 700 mV when microbead#1 is selected and 850 mV when microbead#2 is selected. The cross-talk is small enough as long as the transmitted power is kept to a minimum. In other words, for the FDMA approach to work effectively, the transmitted power needs to be adjusted until the addressed microbead receives the minimum amount of power to generate the necessary current. This can be achieved by using a closed-loop system, in which the feedback (e.g., neural recording, backscattering, subject's behavior, etc.) notifies when the microbead has turned "ON".

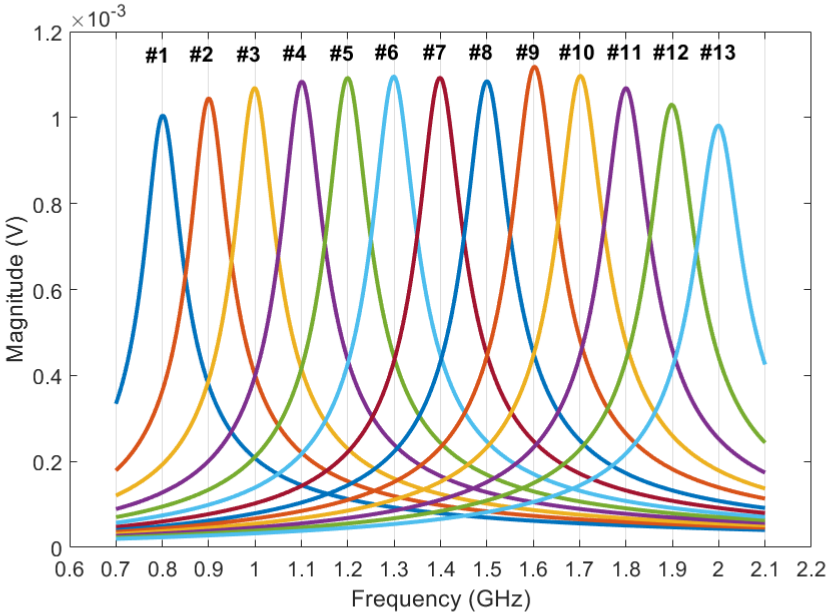

Figure 2.2: Simulated frequency response of 13 microbeads.

Table 2.1: Individually Addressable Microbeads

Microbead #	1	2
Rx resonant frequency (GHz)	1.25	1.5
Tx-Rx Distance (mm)	4.6	
Medium	Beef	
Lateral Misalignment Δx (mm)	+2	-2
Voltage (V) when f = 1.25 GHz	1	0.31
Voltage (V) when f = 1.5 GHz	0.15	1

Despite the fact that operating at higher frequencies increases the specific absorption limit (SAR), there are a couple of noticeable and proven advantages for small implants, such as:

- larger induced voltages and deeper penetration in tissue [43],
- higher Q for the Rx coil (due to a closer proximity to the peak Q), and
- smaller filtering capacitor needed since the peak-to peak voltage ripple after rectification is given by:

$$\triangle V_{pp} = \frac{I_{load}}{2 f_{RF} C_{filter}} \tag{2.1}$$

C_{filter} represents the output capacitor of the charge pump, which is used to smooth the signal between the waves.

Since the relative permittivity of brain tissue is much higher compared that of air, the wavelength at the operating frequency of the microbead is significantly reduced once it reaches tissue. For instance, for a transmitting power frequency of 2 GHz, the wavelength is 15 cm in air and around 2 cm in the grey matter. Depending on the implantation depth (d) and the frequency of the power signal, the microbead can either be in the reactive near-field ($d < \frac{\lambda}{2\pi}$), the radiating near-field ($\frac{\lambda}{2\pi} < d < \lambda$), or the mid-field ($d \approx \lambda$). The field variation impacts the PTE, but does not influence the Tx and Rx coil design methodology described in the following sections. As the overall efficiency improves, the implantation depths will increase over the years, but in this work the measurements in air and tissue are done using small Tx-Rx distances (< 1cm), thus keeping the microbead in the near-field region.

2.3 Transmitter Coil Design

2.3.1 Design flow

A system with a Tx and Rx coil can be modeled as a two port network. The efficiency of that network can be expressed as [44]:

$$\eta = \frac{Re(Z_l)}{Re(Z_{in})} \left| \frac{Z_{21}}{Z_{22} + Z_l} \right|^2 \tag{2.2}$$

where Z_{in}, Z_{22} are the input and output impedance of the network, respectively. Z_{l} is the load impedance, and Z_{21} is the forward transimpedance gain.

Since the Rx coil diameter is very small compared to that of the Tx, the effect of the Rx on the network can be neglected because Z_{in} and Z_{21} does not change significantly with L and Q for a fixed Rx coil diameter. When assuming $Z_{in} = Z_{11}$, η can be rearranged such as:

$$\eta = \frac{|Z_{21}|^2}{Re(Z_{11})} \frac{Re(Z_l)}{|Z_{22}+Z_l|^2} \tag{2.3}$$

where Z_{11} is the input impedance.

The optimal design of the Tx coil can then be expressed as the following figure-of-merit:

$$FOM_{Tx} = \frac{|Z_{21}|^2}{Re(Z_{11})} \tag{2.4}$$

Two different design procedures are shown in Fig. 2.3. In step 1, the constraints are considered. It is important to first consider the neural interface application before designing the optimal Tx coil since the brain target region will determine the distance between the Tx and the microbead. Since SRF_{Tx_min} is set to twice the resonant frequency, a single turn Tx coil has to be used, eliminating the option between the different number of turns, and thus simplifying the optimization flowchart. The surrounding medium has to be determined as well and included in the simulations from the beginning.

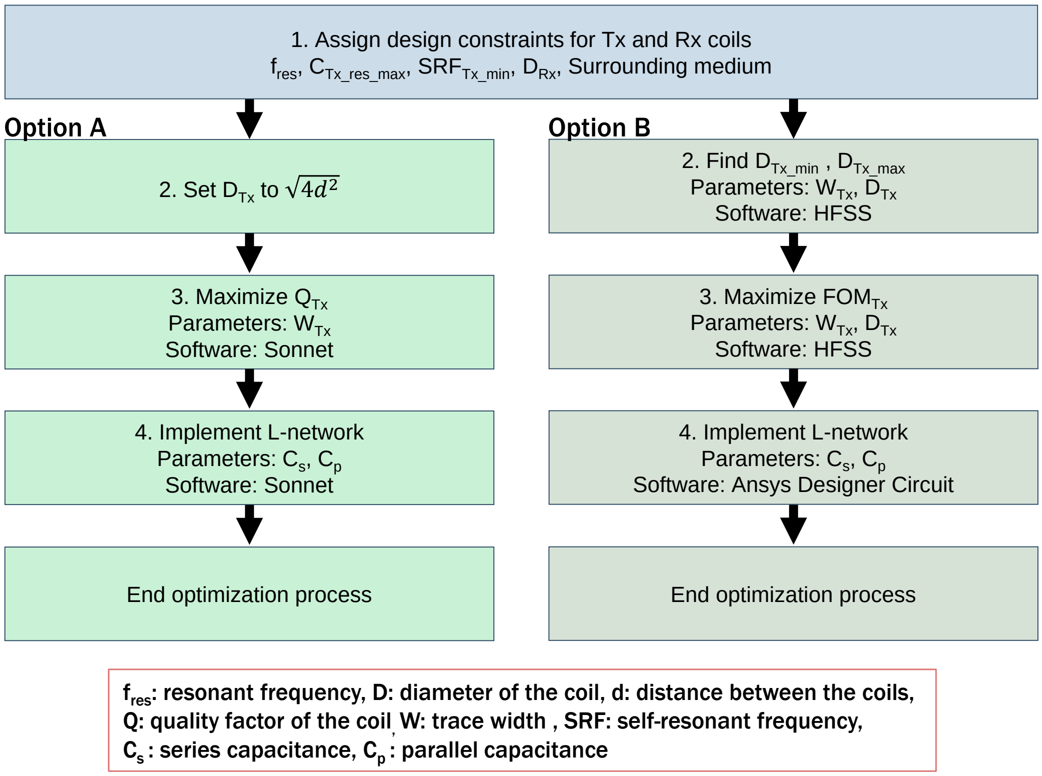

Figure 2.3: Two different iterative design optimization flowcharts for the Tx and on-PCB coil.

Option A is the fastest method in designing the Tx coil as the Sonnet software is easy to use, the Tx coil diameter is immediately estimated, and the Rx coil does not need to be included in the simulations. To give a sense of time that it takes to optimize the Tx coil using the proposed design flow, the external coil parameters were found after a simulation of less than 30 minutes using a laptop with a processor speed of 2.5 GHz (give CPU model) and 16 GB of RAM. In step 2, the estimated Tx coil diameter is calculated based on [45]. Note that the Rx coil diameter coil has been removed from the equation as it is not large enough to impact the result. Also, a very large Tx-Rx distance (e.g. applications in human brain), will result in a large Tx coil diameter which might violate the minimum SRF constraint, in which case the Tx coil diameter is simply set to the highest value possible. In step 3, the quality factor is maximized by sweeping the width. Step 4 aims to match the coil resistance to that of the power amplifier and enable resonance.

Option B relies on the full-wave electromagnetic field solver HFSS to find optimal design parameters for the Tx coil. Step 2 of the Tx design aims to find D_{Tx_min} which is limited by the size of two capacitors that make up the L-match capacitor network used to maximize the transmitted power and D_{Tx_max} which is limited by SRF_{Tx_min}. In step 3, the coil width and diameter are found by maximizing FOM_{Tx}. The diameter of the Rx coil is the only parameter which can impact the FOM_{Tx}, thus its trace width and number of turns does not play a role in the Tx coil design. Step 4 is the same as that of Option A.

Although substrate-based coils present their own unique set of challenges, the complexity of the proposed optimization design flow for the 2-coil wireless link remains low, due to the independent (to some extent) optimizing of the external Tx and Rx coil. This is made possible because of the ultra-small size of the receiver and its negligible influence on the Tx coil, which is not the case in most near-field powering systems.

2.3.2 Matching network

To maximize the transmitted power, the series trimmer capacitance (C_s) and the parallel trimmer capacitor (C_p) allow for the exact tuning to the desired resonance and matches the resistance to that of the power amplifier. By assuming that the parasitic series resistance of the coil (R_s) is smaller than 50 Ω (R_{pa}) and that of the trimmers to be negligible, the two capacitors can be expressed as:

$$C_s = \frac{1}{w^2(L - L_{eq})} \tag{2.5}$$

$$C_p = \frac{L_{eq}}{R_s R_{pa}} \tag{2.6}$$

where

$$L_{eq} = \frac{\sqrt{R_s R_{pa} - R_s^2}}{w} \tag{2.7}$$

is the equivalent of the coil's inductance (L), reduced by the negative reactance of C_s.

2.3.3 Simulation Results

Going through the design steps (Option B) for a resonant frequency of 1.3 GHz, leads to the following results:

- D_{Tx_min} = 8 mm and D_{Tx_max} =15 mm
- D_{Tx}= 10 mm and W_{Tx}= 3 mm (Fig. 2.4)

Option A design flow provided the same parameter values. It is important to note that this is not always the case as it depends on the design constraint. When the parameters are different Option B provides better performing Tx coils then that with Option A, as it trades off accuracy for design speed.

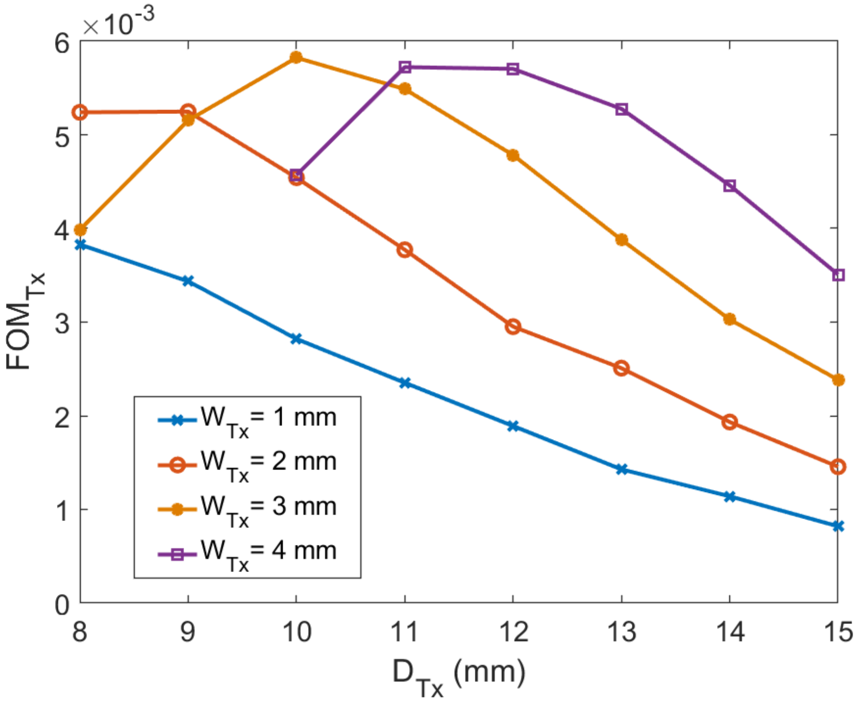

Figure 2.4: $\mathrm{FOM}_{\mathrm{Tx}}$ produced from different combinations of D_{Tx} and W_{Tx} at 1.3 GHz.

2.4 Receiver Coil Design

2.4.1 Design flow

The key to designing the Rx coil is to maximize the quality factor and to set the inductance such that the coil resonates at a particular frequency. The unloaded Q-factor of a coil is defined by:

$$Q_{Rx} = \frac{2\pi f \times L_{eff}}{R_s}$$

where L_{eff} is the effective inductance of the coil and R_{s} its series resistance.

The design procedure for the on-chip coil is shown in Fig. 2.5. The aim is to respect the constraints, have a resonating coil and shift the highest quality factor (Q) to the operating resonating frequency. Larger Q comes at the cost of reduced reception bandwidth (BW) which is favorable in this case as it improves the individual selectivity of each resonating microbead.

3D EM solvers such as Ansys HFSS and COMSOL are considered to be the standard tools for the design and optimizing of a wireless coil, but in terms of computation time and accuracy, a better method is to use the parameterized cell (pcell) provided by the IC foundry. Pcells are modeled based on extensive measurements results, whereas 3D EM solvers accuracy are as good as the knowledge of the IC (which can be very limited) and the computation power available. For these reasons, the Rx coil was mainly designed using

Cadence. Multiple inductor models are usually offered by the foundry, all of which are very well characterized. The dual layer series stacked inductor has been chosen for this work as it allows the effective inductance to be high while avoiding placing the capacitors directly underneath the inductor which degrades the Q (further discussed in the next section).

In step 1, the constraints are considered. The Rx coil diameter depends on the device area constraint and is always maximized as much possible. In step 2, the maximum width and minimum number of turns are found in order to set limits on the searching parameters. This is done by sweeping the trace width and number of turns until the values for minimum inductance and minimum SRF are obtained (which were defined in step 1). Increasing the number of turns leads to a larger inductance, but also increases resistance and parasitic capacitance, which leads to a lower SRF. Choosing a larger width for the traces increases Q_{Rx} (because it lowers R_s) but limits the number of turns for a given coil diameter and lowers the SRF by increasing the parasitic capacitance. In step 3, the peak Q is shifted to the resonating frequency. At this point, the geometry of the coil is defined.

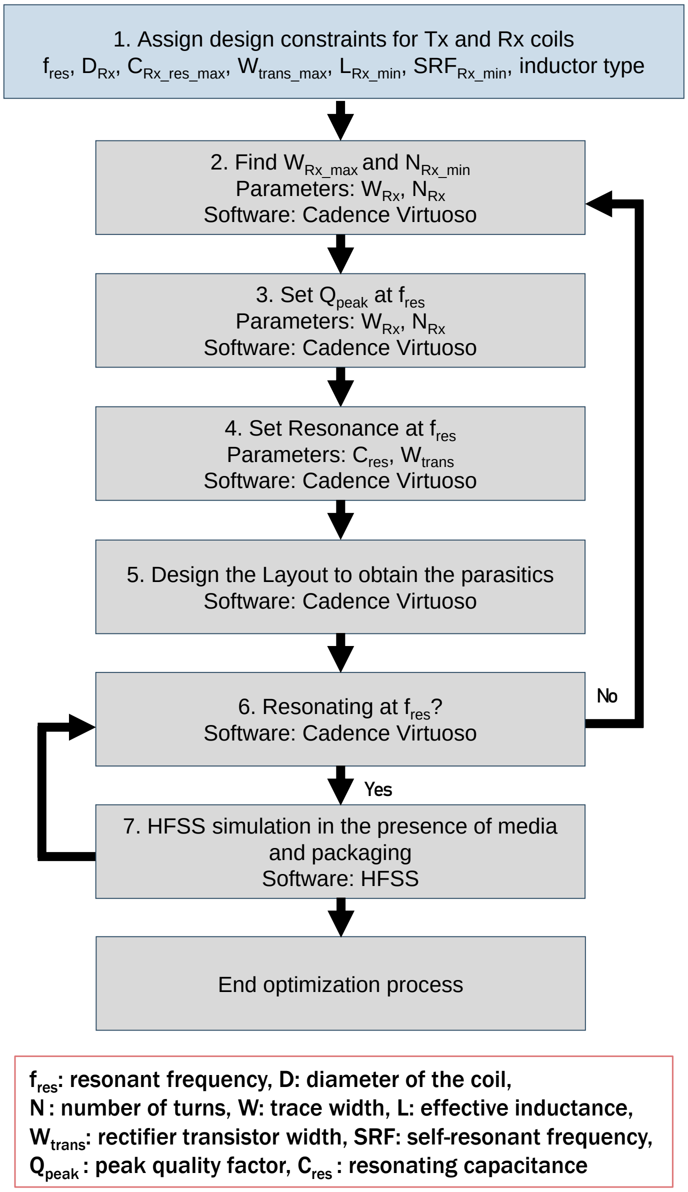

Figure 2.5: Iterative design optimization flowchart of the Rx on-chip coil.

In step 4, resonance is made possible by sweeping the value of the resonating capacitor. In the special case of the microbead, since the capacitor is eliminated for the purpose of miniaturization, this is achieved by sweeping the transistor's width in the rectifier. In step 5, the layout is designed and the parasitics are extracted. At this stage, there is the option to further increase Q_{Rx} by placing a patterned ground shield underneath it, but this was not done in this work as it would decrease the SRF of the coil and violate the minimum SRF constraint. In step 6, the Rx coil is simulated with the circuit in order to verify if resonance still occurs at f_{res}. In step 7, HFSS can to be used to account for the presence of media and device packaging, for instance, an IMD has to consider the shift in coil impedance caused by the presence of tissue and the electrode.

Furthermore, this stage has the option of including load optimization which consists of matching the resistance of the harvesting circuit to the equivalent parallel resistance of the coil's series resistance. This was not done in this work as multiple loads have been tested to account for various applications.

2.4.2 Challenges specific to on-silicon coils

Only a small percentage of research groups working on wirelessly-powered IMDs have relied on integrated inductors [6, 46, 47]. The main reason is the fact that on-silicon inductors used for energy harvesting have a much lower quality factor (Q_{Rx}) compared to off-chip coils [48] because of the low thickness metallization and losses introduced by the silicon substrate (Fig. 2.6). Despite these drawbacks, the usage of on-chip coils offers significant advantages to floating wireless neural devices because it allows for a: *i)* smaller implant by eliminating the bulky external RX coil, *ii)* good repeatability, *iii)* reduction in the number of parts to assemble, and *iv)* simpler implementation of the matching network because of the well defined on-silicon parasitics of the routing between the coil and the circuit.

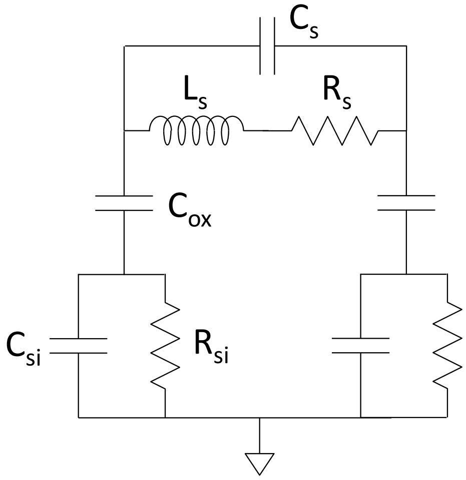

Figure 2.6: Equivalent circuit model of an on-silicon coil.

Although external coils, such as the wire-wound coil, can achieve higher Q than the CMOS integrated coils, it is very challenging to miniaturize them down to the sub-mm scale. As miniaturized state-of-the-art wirelessly powered devices continue to become smaller, they will have to rely on substrate-based coils which have their own unique set of challenges. While there is an abundance of literature on radio-frequency identification systems, research on small (< 500 µm) integrated coils for near-field powering is still immature. This section focuses on addressing these distinctive challenges.

2.4.2.1 Impact of MIM caps on the PTE

To save area, the Rx coil can either surround the circuitry or be placed above it. Placing it on top enables further miniaturization and allows for more turns. The drawback is the formation of a large parasitic capacitance C_c (Fig. 2.7), which changes the coil characteristics. To investigate the influence of the MIM capacitors on the electrical properties of the coil, the on-chip coil's Z-parameters were measured in two different configurations (with and without the circuitry underneath). As can be observed in Fig. 2.7, at 1.3 GHz, C_c has caused the quality factor to decrease by 19%. As for the inductance, the effect is not as significant but could result in a slight detuning of the resonant frequency. The 130 nm CMOS process utilized offered 8 metal layers, the MIM capacitors used metal 7 and 6, whereas the coil used metal 8, thus the close proximity of the metal layers explains the large C_c. This issue can be mitigated by using a vertical natural capacitor (VNCAP) in fabrication processes that offer more metal layers or a metal oxide semiconductor (MOS) capacitor in smaller technology nodes. The solution implemented in this work was having the on-chip coil surround the circuitry.

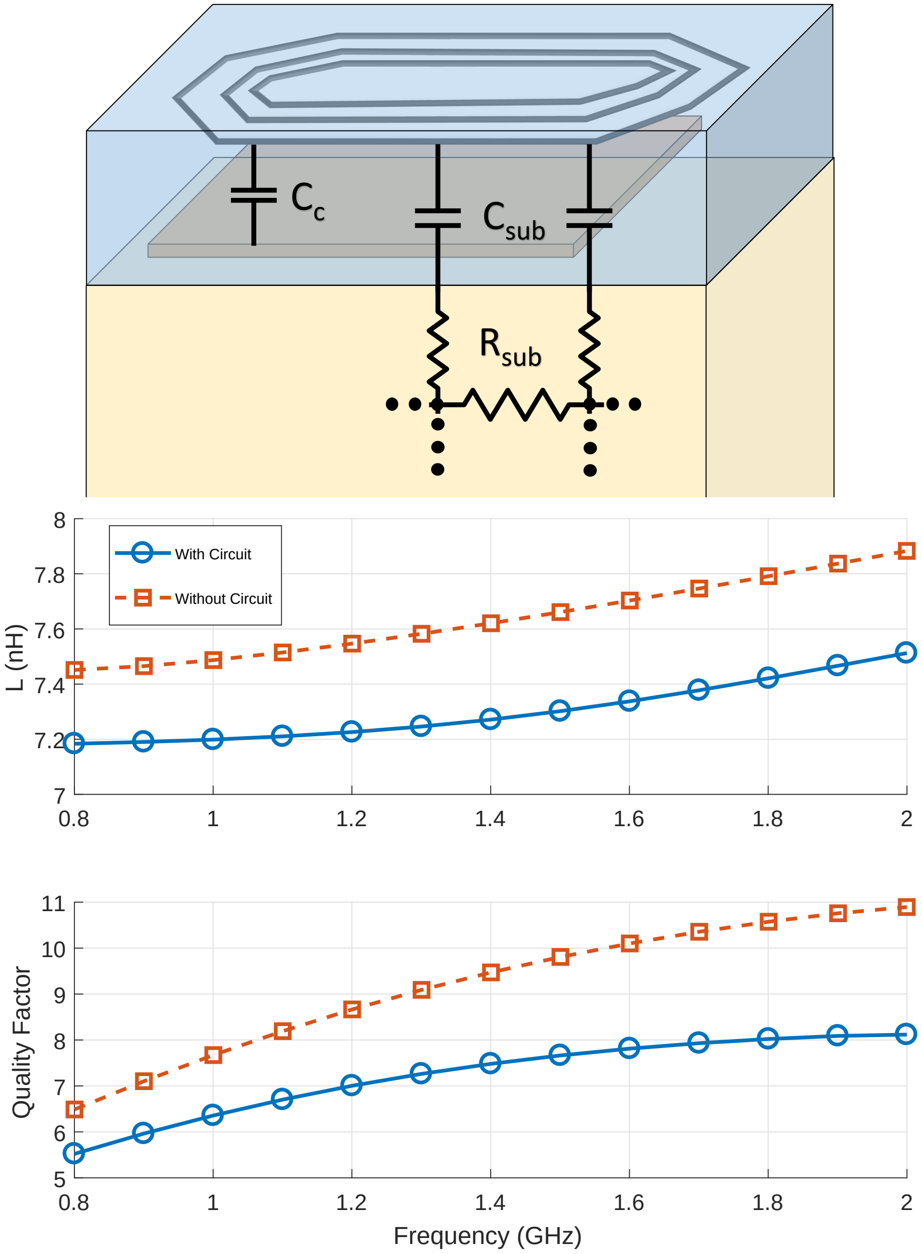

Figure 2.7: (Top) Simplified lumped model of the parasitics of an on-chip inductor on top of a MIM capacitor. (Bottom) Measured inductance and quality factor of the on-silicon coil with and without metal layers underneath.

2.4.2.2 Impact of the IC pad frame on the PTE

The section investigates the effect of conductive traces present around the inductor on its parameters. A typical IC pad frame includes a seal ring, power buses, and metal fills. The seal ring contains all the metal layers available in the fabrication process with uninterrupted continuous contacts and vias. It is used to prevent ionic contaminants from entering the circuits and to protect the IC from cracks that can be introduced during dicing. The foundry design guidelines do not allow the chip to be fabricated without the seal ring. The wide power buses are used to power the circuit and the ESD structures. They also surround the on-chip coil. The metal fills that are needed to satisfy the metal density rule were omitted in this study as they showed a negligible difference when placed around the Rx coil. On the other hand, the grounded seal edge and power buses diminish the gain of the on-chip coil as any metal loop can create a magnetic field that counters that of the source. In order to estimate their impact, the full-wave electromagnetic field solver HFSS is used to simulate the efficiency of an on-chip coil in different setups (Table 2.2).

The transmitter (Tx) and receiver (Rx) coils have been modeled as a 2-port network. The Z-parameters of this network are extracted to find the maximum achievable efficiency under optimum loading conditions [49]:

$$\eta_{max} = \eta_{amp} \times \frac{\chi}{(1+\sqrt{1+\chi})^2} \tag{2.8}$$

where η_{amp} represents the power amplifier efficiency and χ can be derived from the Z-parameters of the network as:

$$\chi = \frac{|Z_{12}|^2}{Re(Z_{11})Re(Z_{22}) - Re(Z_{12})^2} \tag{2.9}$$

for simplicity, we neglect the effect of η_{amp} in calculating efficiency.

Table 2.2: Different pad frames used to characterize its impact on PTE.

Setup	A	B	C	D
Coil	x	x	x	x
MIM caps		x	x	x
Seal Edge			x	x
4 Power buses				x

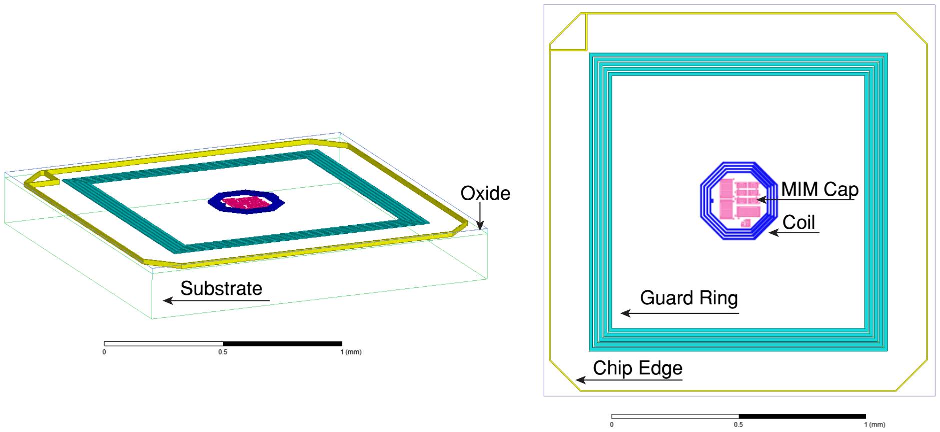

(a)

(b)

Figure 2.8: (a) Cross section and (b) top view of the 2-link simulation setup.

A single-turn on-PCB coil with 10 mm diameter and 3 mm trace width is used as the Tx coil to transmit power wirelessly. A 7 turn on-silicon coil with 300 µm diameter and 7 µm trace width is used the Rx coil. Fig. 2.8 shows the HFSS layout for setup D. As can be observed in Fig. 2.9, the pad frame significantly impacts the efficiency with respect to a stand-alone coil. To eliminate the influence of the seal edge and power buses on the coil's gain, the wafer or die can be diced in such a way as to leave only the Rx device and the pads needed to interface the ASIC as shown in Fig. 2.10. When MIM capacitors are centered underneath the on-chip coil, they lower the gain by less than 2 dB. Their influence on the electrical properties of the coil can be much more significant if placed directly underneath the coil's traces as shown in the previous section.

2.4.2.3 Power consumption of the Rx coil

A parallel resonant LC tank is conventionally used for receivers to maximize the induced voltage. However, as depicted in Fig. 2.11, at resonance the magnitude of the circulating current between the inductor (L) and the resonating capacitor (C_{res}) is often many times larger than the current supplied to the load (assuming $|Z_{Load}| > R_C$ & R_L). For a fixed voltage across the coil, the power lost in the tank increases as the quality factor of the coil decreases. An on-chip coil with a small impedance (due to small inductance) will cause a high current to go through its equivalent series resistance (ESR) and that of the resonating capacitor. This leads to high power consumption because of the high ESR of

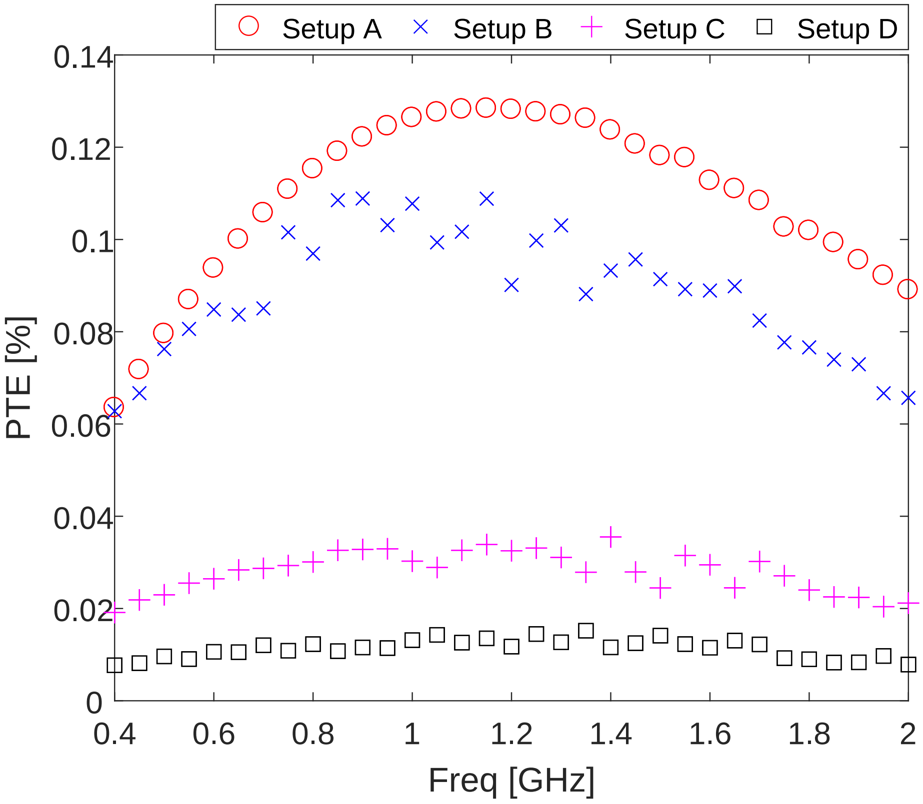

Figure 2.9: Simulated on-chip coil coupling link efficiency through air with 5 mm of Tx-Rx separation using different IC pad frames.

the µm-size coil. This is often not observed for larger external Rx coils because of their much lower ESR. Thus, with respect to power consumption, a series resonating LC tank is a better option for small integrated coils that operate at high frequencies and are used for low-power receivers.

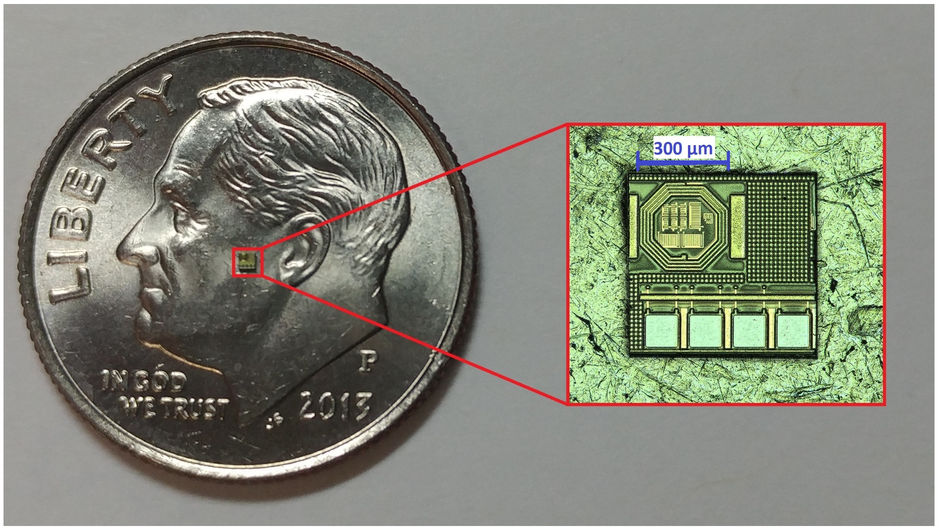

Figure 2.10: Micrograph of the diced Rx die used to measure the regulated voltage.

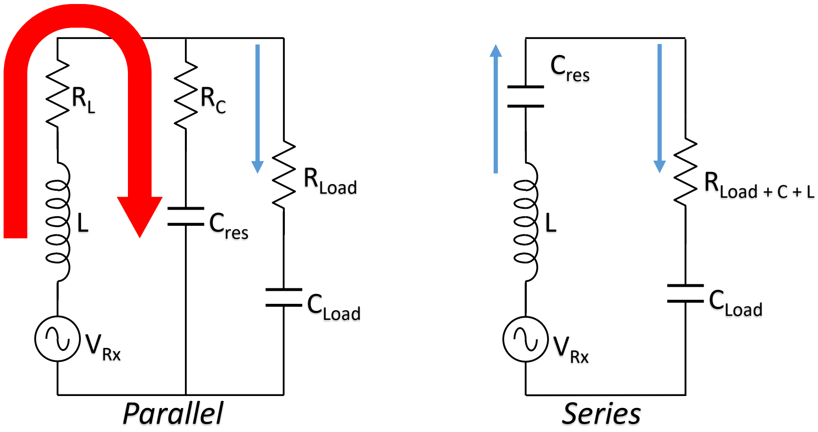

Figure 2.11: Simplified circuit model of a lossy parallel and series resonating LC tank.

2.4.2.4 Resonant frequency shift

Although HFSS simulations can take into account the Rx coil surroundings to accurately estimate the effective inductance, a shift in the resonant frequency can be expected. This shift is even larger for µm-sized coils due to additional factors such as process variations and the power received at the Rx coil. This is because a miniaturized Rx device has a hard constraint on the size of the on-chip resonating capacitor. This leads to a larger impact of the parasitic capacitance coming from the diode-connected transistors in the rectifier which is related to the junction capacitance given by: $C_j = \frac{C_{jo}}{\sqrt{1-V_D/\phi_B}}$

where V_D, the voltage generated across the diode is proportional to the source power.

A common method to remotely locate the resonant frequency is by using the maximum phase-dip technique. It involves measuring the input impedance phase of a non-resonating Tx coil in close proximity to the resonating on-chip coil. Unfortunately, the vector network analyzer (VNA) maximum output power is not high enough as to cause a noticeable phase-dip when working with ultra-small Rx coils. A more reliable method is to tune the capacitors of the Tx coil in order to resonate at different frequencies around the target resonant frequency while measuring the unregulated voltage generated by the Rx harvester. The measured peak voltage represents the new resonant frequency. A post-layout simulation in Cadence reveals a resonant frequency of 1.17 GHz while the measured resonant frequency is found to be 1.18 GHz when the Rx device is fully powered (which happens when the regulated voltage reaches its target value of 1 V). It is important to note that the transmitted power can be adjusted based on the Tx-Rx distance in order to guarantee minimum required power received at the Rx device, which secures a fixed resonant frequency of 1.18 GHz.

2.5 Experimental Tests

In this section, the Tx and Rx coil characteristics are measured and their measurement setup is described. It is very challenging to measure the PTE involving an ultra-small Rx coil as any connection to the on-chip coil will add parasitics and behave as a bigger inductive loop. This is due to the fact that the size of the Rx coil is in the deep sub-mm scale, whereas the bondwires and PCB traces are in the mm to cm range. Therefore, rather than finding the RF-RF efficiency (also known as PTE in this work), the RF-DC efficiency is measured as the parastics added by the pads, bondwires and PCB traces do not affect the DC voltage. Since RF-DC efficiency includes the efficiency of the harvesting circuit, these measurements were included in Chapter 4.

2.5.1 Measurement Setup

Characterization of the Tx and Rx coil was done using a vector network analyzer (ZVL, Rohde & Schwarz). In addition to the VNA, as shown in Fig. 2.12, the measurement setup for the on-chip coil also required a micromanipulator probe station and an RF probe (Z10-GS-150; Cascade Microtech). Double-sided tape is used to hold the die in place on a grounded metal cylinder. For accurate measurements, the parasitic effect caused by the coaxial cable, probe, pads, and the feed lines were removed during the de-embedding calibration procedure (on-chip short/open/50Ω). Same goes for the Tx coil, the parasitics from the SMD connector and cable were eliminated.

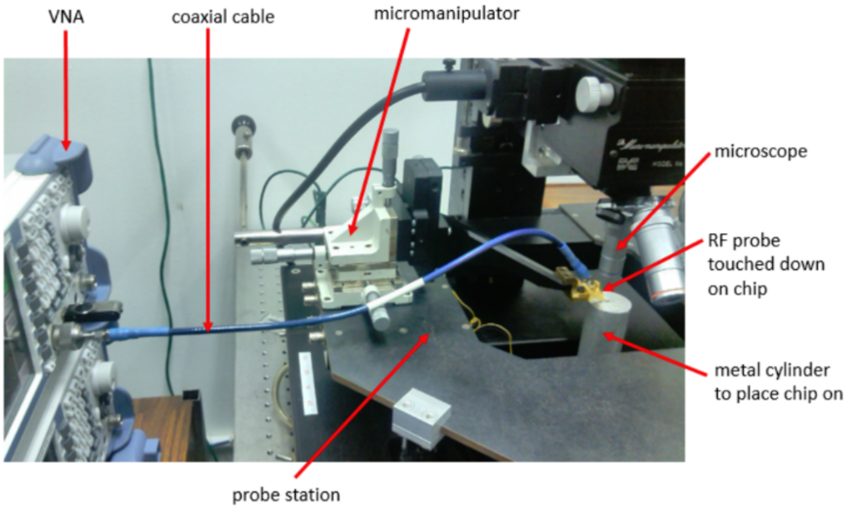

Figure 2.12: Measurement setup for the characterization of the on-chip Rx coil.

2.5.2 Measurement Results

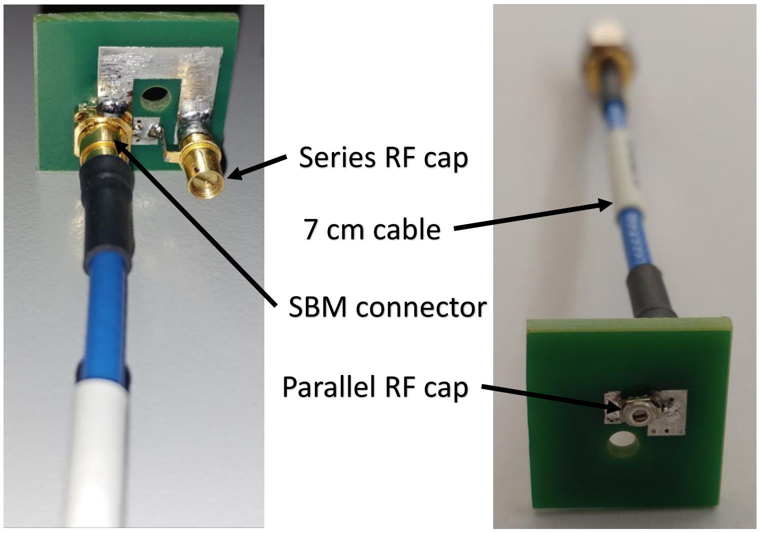

Figure 2.13: Front and back view of the Tx coil with the L-match capacitor network.

The transmitter is a single turn coil built on FR4 substrate. The PCB also contains the L-match capacitor network to maximize the transmitted power. It is important to note that due to the small size of the Tx coil, the PCB interconnect (connecting the SMA connector to the coil), the coaxial cable (connecting the PCB to the power amplifier) and the SMA connector had an appreciable effect on the coil parameters. In order to decrease the number of voltage maxima (an issue that arises when the cable length is much larger than $\lambda/4$) and parasitic capacitances added by the interconnect, cable and large connector, the traces were eliminated, the coaxial cable was chosen to be as short as possible and the SMA connector was replaced by an SMP connector. To remove the interconnects, the connector and the capacitors had to be placed on top or below the coil (Fig. 2.13), which shortened the inductor but allowed more of the source energy to be picked up by the microbead. Furthermore, the interconnects were removed in order to make the Tx coil as symmetrical as possible such that it can be used in a coil array for near-field beamforming [36].

Two different types of on-chip coils were designed and fabricated. One measures 200 μm in diameter, the other 300 μm. The larger one is an improved version since its peak Q has been shifted to its resonant frequency (following the design flow guidelines) and surrounds the MIM capacitors rather than being right on top of them. Measured characteristics of the Tx coil and Rx coil are summarized in Table 2.3.

Table 2.3: Characterization of the Tx and Rx Coil

Parameter	Tx	Rx (v1)	Rx (v2)
Diameter (mm)	10	0.2	0.3
Material	*Cu*	*Al*	*Al*
Trace width (mm)	3	5e-3	7e-3
Trace thickness (µm)	35.6	4	4
Space between turns (mm)	*N/A*	5e-3	5e-3
Number of turns	1	8.5	7
f_{res}(GHz)	1.3 | 1.18	1.3	1.18
Q at f_{res} in air	348 | 359	7.3	12.2
L at f_{res} in air (nH)	8.1 | 8	7.2	25
SRF (GHz)	4.1	8	2.5

Fig. 2.14 compares the measured quality factor (Imag(Z_{11})/Real(Z_{11})) of the stand-alone 200 µm coil with simulations done in HFSS and Cadence tool. Measurement results are in good agreement with Cadence. HFSS plot follows the trend with a lower quality factor by about 0.8.

Fig. 2.15 compares the measured quality factor and effective inductance of the 300 µm coil with simulations done in Cadence tool. When including the entire circuitry of the microbead, the quality factor drops by approximately 1.2 compared to a stand-alone coil.

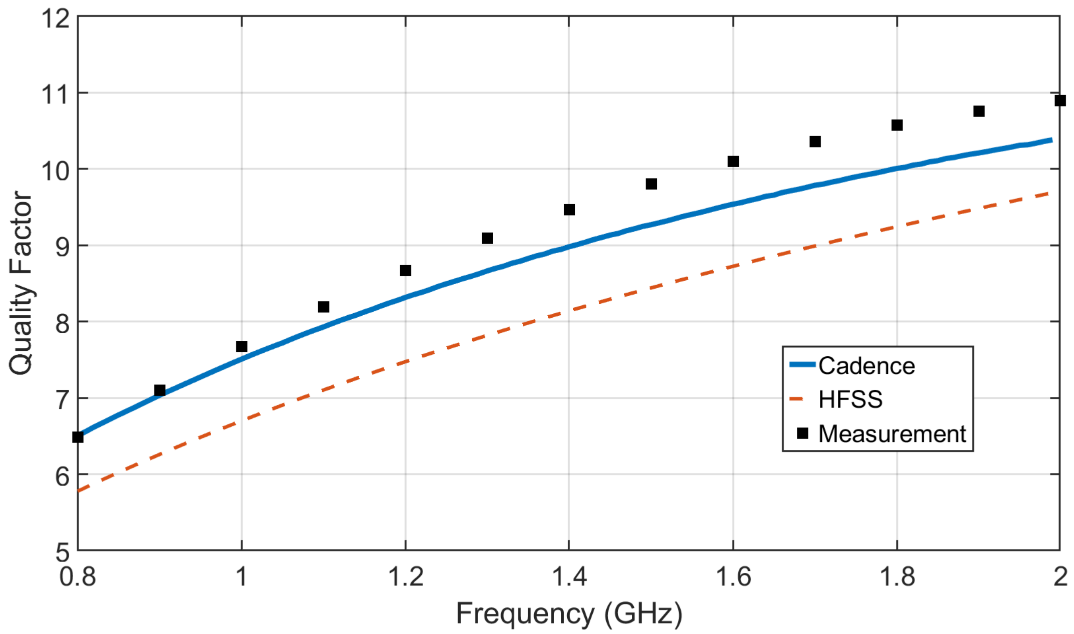

Figure 2.14: Measured and simulated quality factor of the 200 µm on-silicon coil.

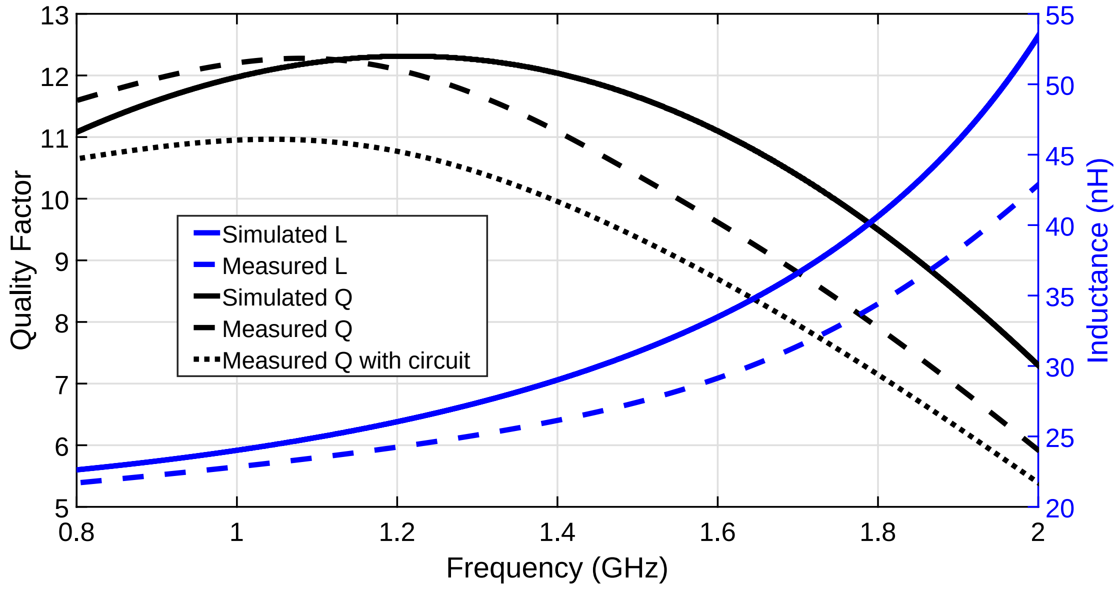

Figure 2.15: Measured and simulated quality factor, and effective inductance of the 300 µm on-silicon coil.

Chapter 3

Ultra-Compact RF Energy Harvesting System

3.1 System overview

The RF power gathered by an implant is generally very low. This is especially true for the microbead because after the signal is attenuated in tissue it is collected by an ultra-small coil. Thus, the energy harvesting circuit must be highly optimized to convert low RF power levels into usable DC energy. In this work, the harvesting circuit includes a charge pump rectifier, a voltage reference and a voltage regulator (Fig. 3.1).

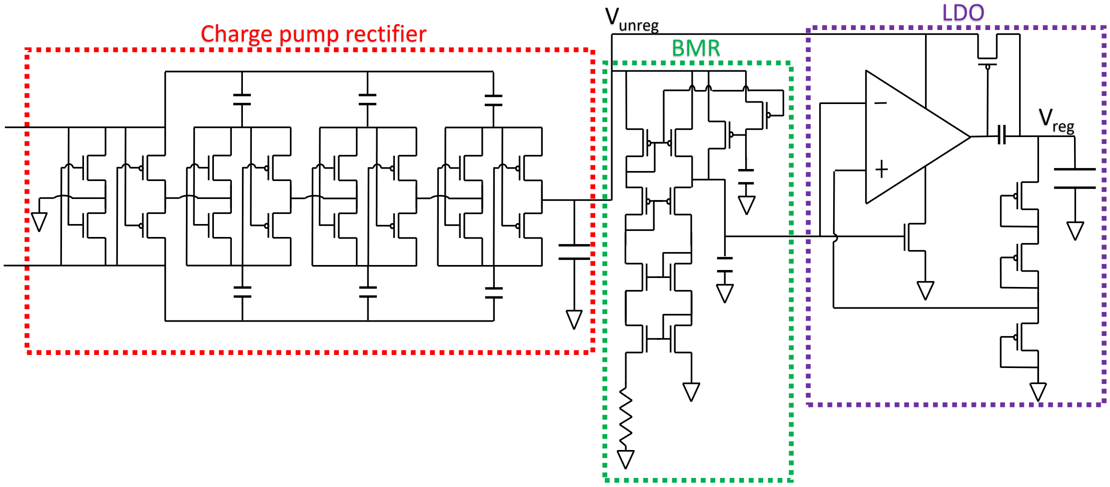

Figure 3.1: Detailed circuit diagram of the entire system harvesting circuit.

3.2 Charge Pump rectifier

The goal in designing the rectifier is to convert the RF signal to DC with high efficiency. There are various rectifiers for different applications, the rectifier type with the highest efficiency will depend on parameters such as frequency, input power and desired DC output voltage. The most common conventional rectifier circuit is known as the full wave bridge rectifier which is comprised of four diodes and one capacitor (Fig. 3.2). However, Schottky diodes are not supported in GF 0.13µm CMOS technology. Fortunately, the diode can be implemented in CMOS technologies using MOS devices. A diode is a two–terminal device in which the device conducts when the voltage across the terminals is larger than the threshold and does not conduct when below threshold. A MOS device with the gate and drain terminals connected is equivalent to a diode as shown in Fig. 3.2. A MOS rectifier structure can thus be formed using only NMOS or PMOS devices or both. Fig. 3.3 shows a bridge-type full wave rectifier composed of only diode connected NMOS transistors.

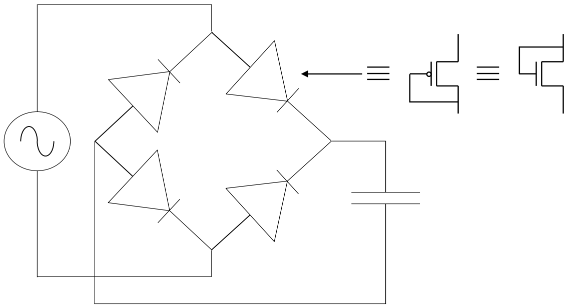

Figure 3.2: Schematic of a full wave bridge rectifier and the equivalent MOS model of a diode.

The threshold voltage (V_{th}) of MOS transistors which is equivalent to the voltage drop of a diode, will reduce efficiency of the rectifier. Therefore, reducing the threshold voltage will increase the efficiency of the rectifier. Two methods have been implemented in this work to reduce or cancel V_{th}.

The bridge-type full wave rectifier exhibits two forward voltage drops as shown in the following equation:

$$Vout_{DC} = Vin_{RF} - 2 \times |V_{th_n}| - V_{loss}$$

Where Vin_{RF} = Vin_{RF+} - Vin_{RF-} and V_{loss} is the voltage drop due to the finite on-resistance of the diode.

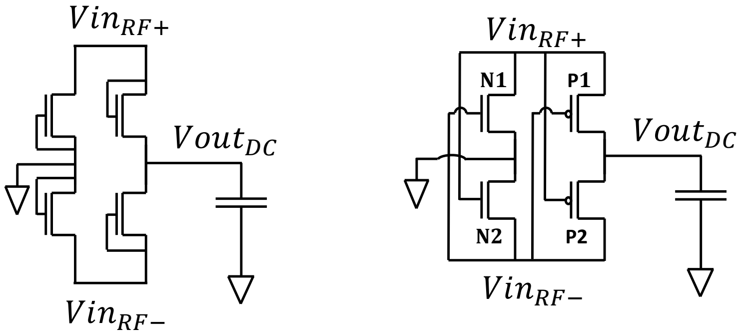

Figure 3.3: Schematic of a (left) bridge-type full wave rectifier and a (right) cross-connected bridge rectifier.

Some IC technologies, such as the one used in this work, offer a variety of different MOSFETs featuring a range of threshold voltages. For instance, low-V_{th} (LVT) and zero-V_{th} (ZVT) transistors, use thinner gate oxide thicknesses to achieve lower V_{th} compared to standard MOSFETs. However, LVT and ZVT transistors also exhibit significantly larger reverse leakage currents, which can effectively counteract any advantage gained from a lower V_{th} value.

The second method of reducing the forward voltage drop is by using a cross-connected bridge rectifier as show in Fig. 3.3. During positive half-cycles of the input voltage, current flows through P1 and N2, while transistors N1 and P2 are in cutoff mode. The situation is reversed for negative half-cycles of the input voltage. In either case, the cross-coupled PMOS transistor (i.e. P1 or P2) have larger Vgs (compared to diode-based rectifier), therefore lower on-resistance.

Since the output of a single-stage rectifier is always below the input amplitude $\mathrm{Vin}_{\mathrm{RF}}$, using a single stage will not suffice when a regulated voltage of at least 1 V is needed. Fortunately, this type of rectifier can be used to obtain voltage multiplication by cascading single stages in a charge pump configuration. As shown in Fig. 3.4, the charge pump rectifier includes four rectifier stages that are connected in series with the RF signal being fed into later stages through coupling capacitors. The output of each stage is the DC reference node for subsequent stages, allowing to build DC voltage higher with each stage. The coupling capacitors (C_c) and the number of stages were optimized to obtain a certain efficiency and DC output voltage. The transistors were sized for optimal power conversion efficiency (PCE), keeping in mind that a larger width increases the forward current while also increasing the flow-back current (which reduces PCE). C_{filt} is added to filter the ripple at V_{unreg}.

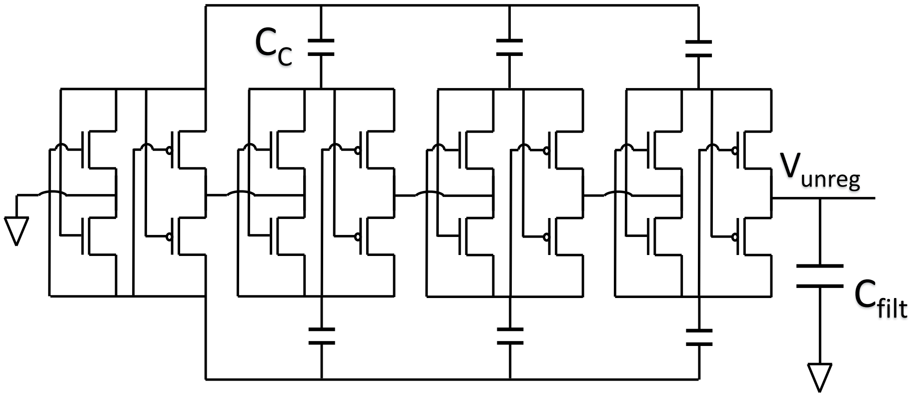

Figure 3.4: Schematic of a 4 stage charge pump rectifier.

The simulated PCE of the charge pump rectifier is shown in Fig. 3.5 and includes the efficiency of the charge pump rectifier and the LDO. Details on the PCE calculation can be found in the "Experimental Tests" section. What can also be noticed from the plots is that the PCE of the harvesting circuit highly depends on the received power and resonant frequency causing it to vary significantly. For a regulated voltage of 1 V, the cross-connected bridge rectifier that uses LVT transistors shows a much larger PCE compared to the diode connected rectifier that uses thick ZVT transistors. The opposite is true for a regulated voltage of 3 V (which requires a larger received power). Therefore, the optimal rectifier type depends on the application, for instance, if the neuroscientist or clinician prefers a larger stimulus amplitude, then the microbead version that offers a regulated voltage of 3 V is best suited for the task.

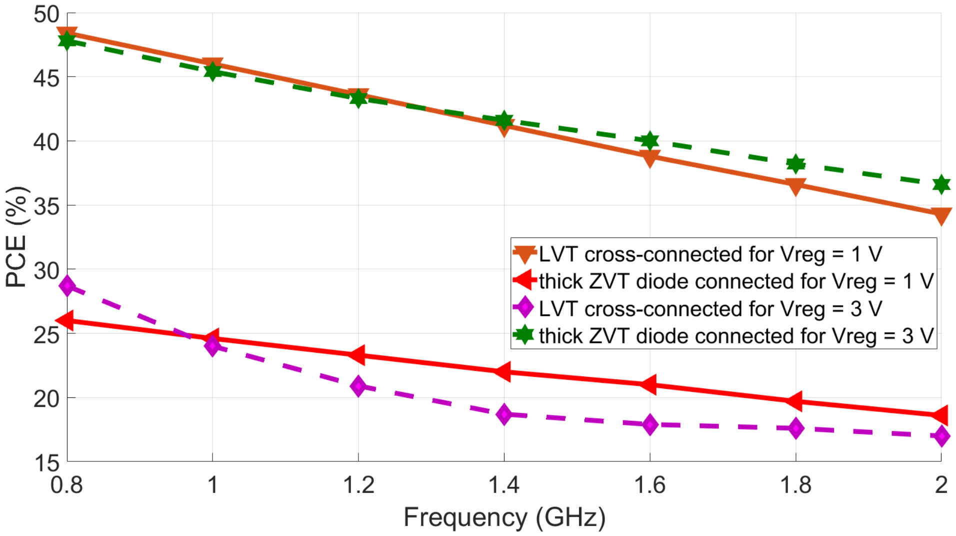

Figure 3.5: Post-simulated PCE over frequency of the harvesting circuit with a load of 30kΩ and a regulated voltage of 1 V and 3 V.

3.3 Voltage Reference

A compact and low power cascode beta multiplier reference (BMR) was designed (Fig. 3.1) as to provide a bias voltage to the LDO. A start-up circuit has been added in order to eliminate the possible zero current condition. It consumes power only when needed thanks to the added feedback. As the temperature in the brain is stable [50], temperature independence was not a main design target. The focus was placed on the power supply rejection ratio (PSRR) and the power consumption.

3.4 Voltage Regulator

A low-dropout regulator (LDO) was designed (Fig. 3.1) to provide stable regulated voltage (needed especially for the recording front-end circuitry). A symmetrical OTA has been chosen as the topology for the error amplifier because of its large output swing. The feedback resistors are implemented using diode connected PMOS transistors with large resistance in order to decrease the DC current through them. A very large load capacitance is usually used to supply more charge to a fast current transient before the op-amp must respond. Thus, in order to improve the system's stability and save area, a compensation capacitor connects the output of the op-amp to the regulator's output.

The effect of load regulation on the regulated output voltage is shown in Fig. 3.6. As can be seen in the figure, a load jump from 20 µA to 200 µA with a rise and fall time of

100 ns causes a maximum undershoot of about 500 mV, a small price to pay when using a 40 pF on-chip capacitor. Fortunately, this is not a major concern since none of the blocks in the microbead induces large transient loads.

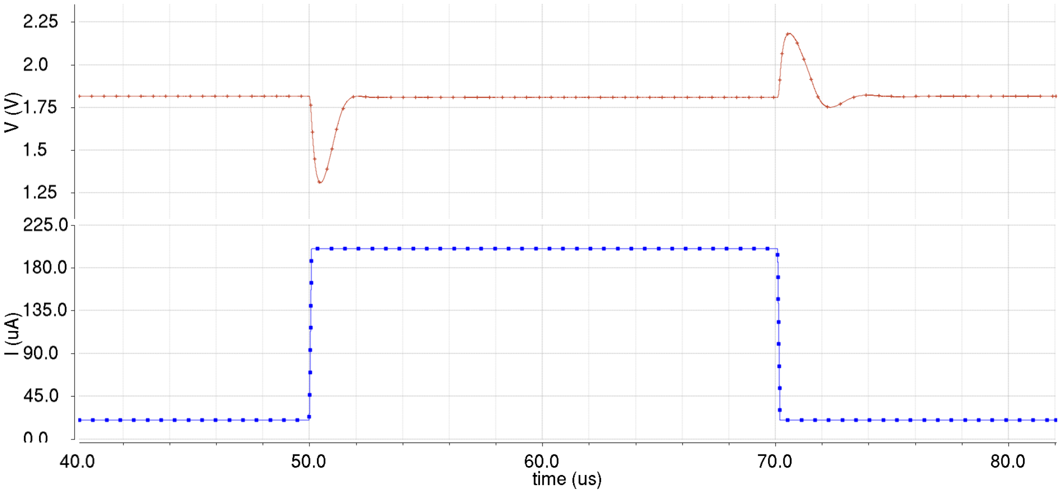

Figure 3.6: Simulated load transient response; (top) output voltage, (bottom) load current.

3.5 Experimental Tests

3.5.1 Measurement Setup

The performance of the harvesting circuit is characterized by its DC output voltage and PCE for a given input power level and input frequency. While the output voltage is straightforward to measure, the input power, and hence the PCE, is considerably more difficult. To compute the PCE, the input power delivered to the harvester must be determined. This can be done using a VNA and by applying following equation:

$$P_{in} = P_{source}(1 - |S_{11}^2|)$$

S-parameter measurements were taken at the input of the harvesting circuit. However, since conventional S-parameter measurements apply a stimulus to only one port at a time, the rectifier is not excited differentially, and thus will not operate as expected. Therefore, to more accurately emulate the simulation setup, a balun has been used in order to provide a balanced signal to the rectifier. Unfortunately, doing so results in the plane of reference being shifted further away from the rectifier input. Thus, a short-open-load on-PCB de-embedding calibration technique has been implemented (Fig. 3.7) in order to remove the parasitic effect coming from the SMA connector, the PCB traces and the balun.

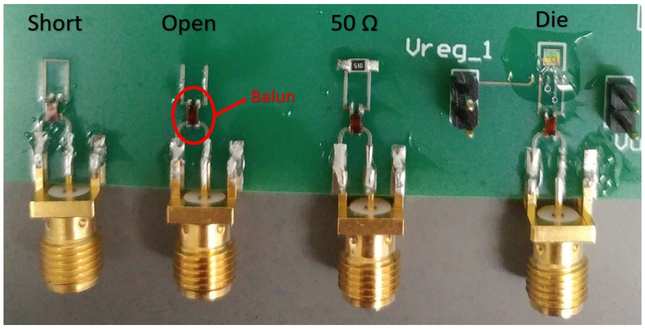

Figure 3.7: Picture of the PCB setup used to measure the PCE of the harvesting circuit.

Efficiency measurements were obtained by sweeping the source power at a certain frequency until the harvesting circuit reaches its regulated voltage of 1 V. In summary the steps taken to measure the PCE for a fixed added resistance load (R_L) and a certain frequency range are:

1. Find minimum P_{source} needed to fully power the microbead using a high frequency signal generator
2. Short-open-load de-embedding calibration
3. Measure S_{11} at P_{source} using a VNA
4. Calculate P_{in}
5. Calculate $PCE = \frac{P_{out}}{P_{in}} \times 100 = \frac{V_{reg}^2/R_L}{P_{in}} \times 100$

3.5.2 Measurement Results

The harvesting circuit is fabricated in GF 130 nm CMOS 8RF technology. The LDO consumes 3.75 μA of quiesent current (for a unregulated voltage of 1.3 V) and has a dropout volage of 30 mV. The BMR has a power supply rejection ratio of -54.2 dB at 1.3 GHz.

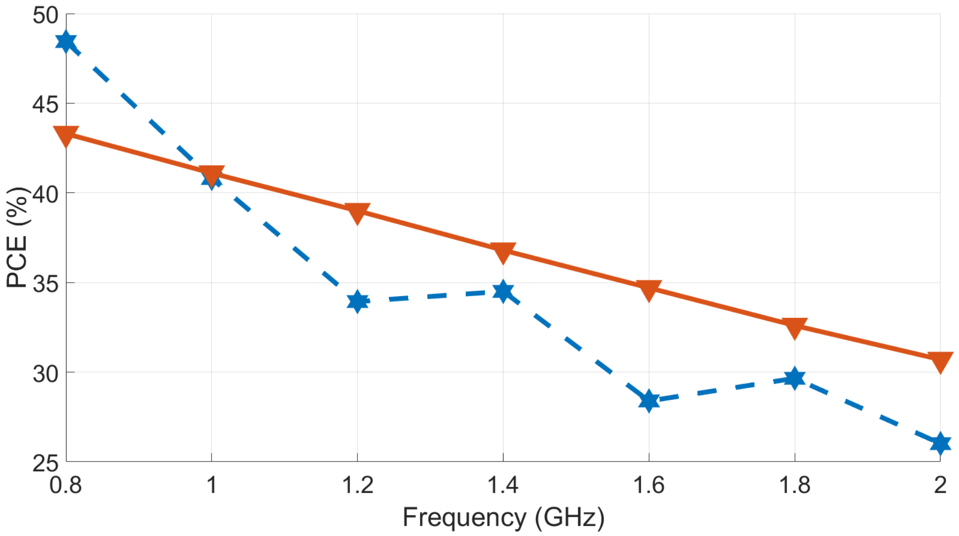

Figure 3.8: Measured and simulated PCE over frequency of the harvesting circuit with a load of 30 kΩ and a regulated voltage of 1 V.

Fig. 3.8 compares the measured PCE with simulations with a load of 30 kΩ and a regulated voltage of 1 V. As shown in the figure, both measurements and simulations show the PCE decreasing over frequency, which is expected because of the capacitive parasitic losses. However, there is a noticeable discrepancy between simulation and measurement results. This discrepancy is in part caused by the imperfections of the balun which shows fluctuating return loss, amplitude and phase over the studied frequency range. Any imbalance in the amplitude or phase between the rectifier's input terminals will result in asymmetrical operation and will therefore exert a negative impact on PCE. Furthermore, although de-embedding calibration technique eliminated the majority of the setup parasitics, it did not remove that of the wirebond and on-chip pads.

Chapter 4

Proof-of-concept: Sub-millimiter sized Neural Stimulator SoC

4.1 Electrical stimulation of the nervous system

In order to interface with the nervous system, it is first necessary to understand the physiology of neurons. There are over 10 billion neurons in the human brain. Neurons differ from other cells in the body in that they have specialized information carrying extensions called dendrites and an axon. The process of ion exchange across their membrane is known as an action potential. Action potentials in live cells can be initiated from external excitation by stimulating optically, magnetically, or electrically.

This work relies on extracellular electrical stimulation which consists of placing the electrode outside the cell. When an external current source (known as current-mode stimulation) or voltage source (voltage-mode stimulation) is introduced to the cell, positive extracellular ions becomes attracted towards the electrode and a depolarization across the cell membrane occurs. When the membrane potential reaches the threshold level, an action potential is triggered. Cell thresholds mainly depends on the distance between the electrode and the neuron, the stimulus profile and the stimulation site. Many researchers have reported successful CNS stimulation by delivering around 3 nC, which can be achieved with a 10 μA pulse amplitude with a width of 300 μs.

4.2 System overview

The entire system used for neural stimulation is shown in Fig. 4.1. The circuit implemented in the microbead is entirely analog. By eliminating the need for data demodulators, decoders, digital control blocks and clock generators, the microbead relinquishes the control of the stimulation pulse amplitude to achieve lower power consumption and further miniaturization [33]. A pulsed power transmission scheme is adopted, and thus the implant stimulates (after a delay of a 5 μs, which is the time it takes to generate the maximum regulated voltage) for every transmitted RF pulse. The microbeads are individually addressable because of their distinct resonant frequency and the stimulus width is simply determined by the "ON" duration of the circuit. Thus, the amount of charge injected into the tissue is linked to the width of the RF pulse. To save area, the on-chip inductor resonates with the coupling capacitors of the charge pump rectifier and the parasitic capacitances of the transistors, the resonant frequency can thus be controlled by changing the transistors width in the rectifiers. The drawback of this approach is the slight decrease (i.e., <3%) in the charge pump rectifier efficiency because of the deviation from the optimal transistor size.

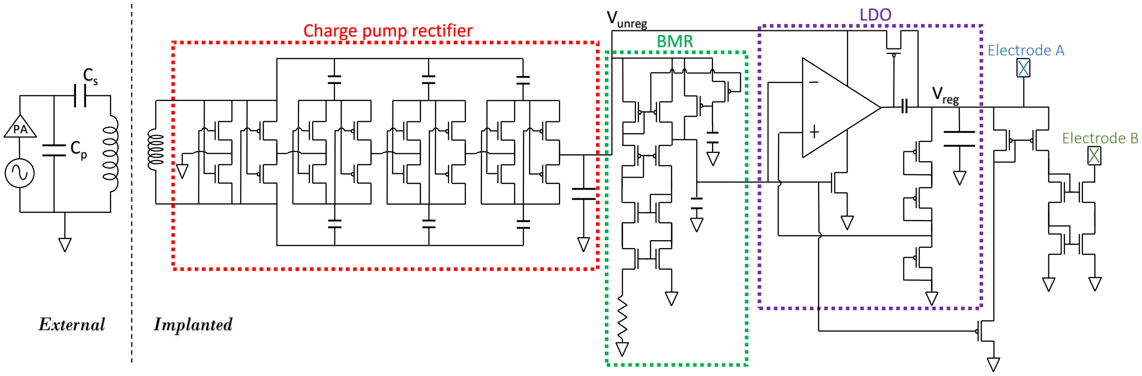

Figure 4.1: Detailed circuit diagram of the entire system showing the external Tx and the implanted ASIC chip.

Multiple microbeads with different coil diameters (e.g., 300, 200, 180), stimulation-modes (current and voltage mode), and stimulus waveforms (monophasic and biphasic) were fabricated and tested to satisfy different applications and their requirements. Two neural stimulation modes are possible depending on where the electrode is placed: current-mode stimulation (CMS) and voltage-mode stimulation (VMS). Most classical stimulators use current mode stimulation over voltage mode stimulation as the pulse strength is directly controllable by current-based stimulation, and thus the charge injected can be easily controlled. In a constant voltage stimulation, the current injected into the tissue is a function of the stimulation voltage and tissue interface (which can vary over time). With respect to power efficiency, current mode is less efficient because of the voltage drop on the current source. In many neural implants with high electrode density, CMS is preferred as VMS requires large capacitors. However, this is not an issue for single-channel implants, making both approaches practical for the microbead.

4.3 Charge Balancing concept

Monophasic pulses lead to charge buildup at the electrode-electrolyte interface, eventually causing damage to the electrode and surrounding tissue. Therefore, high frequencies pulses can be problematic since charge buildup occurs when the microbead is not fully discharged before the next pulse occurs. Biphasic pulses maintains charge balance and are often used to safely stimulate tissue. Unfortunately, because the microbead does not receive any control signal (to adjust the stimulus parameters), conventional current driver circuits cannot be implemented to generate biphasic pulses. Thus, a different approach was taken.

Fig. 4.2(a) shows a simplified equivalent circuit model of the electrode/electrolyte interface. R_s, R_{ct} and C_{dl} represent the solution spreading resistance, the charge transfer resistance and the double layer capacitance, respectively. The transistor whose gate is connected to a voltage source represents the current stimulus driver of the microbead; the voltage source represents the regulator generating the 1.2 Vdd. A resistor (R_v) in parallel with the voltage source is added to take into account the resistive path to ground. The switch closes when the microbead in “ON” and opens when it’s “OFF”.

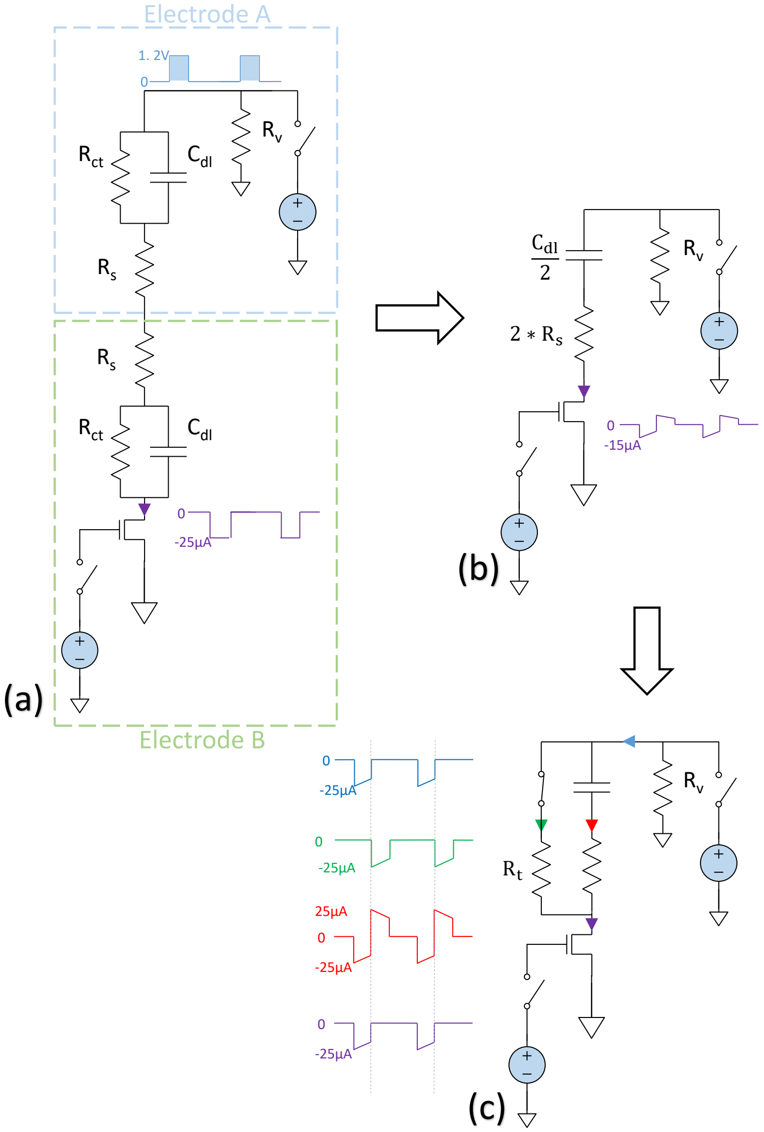

Figure 4.2: The creation of biphasic stimulation shown using the electrode-tissue interface model of the microbead.

If resistive electrodes (such as iridium oxide, platinum, and PEDOT) were to be used, neural stimulation would be dominated by a small R_{ct}, and a square shape monophasic pulse would be applied. However, faradaic reactions can corrode the electrode and damage the tissue, therefore only capacitive electrodes are used for the microbead.

Capacitive electrodes (such as carbon nanotube, titanium nitride and tantalum/tantalum pentoxide) have a large C_{dl} which dominates the electrochemical reactions at the electrode-electrolyte interface, and can be represented by the electrical model in Fig. 4.2(b). This circuit behaves like an RC differentiator circuit. Assuming the RC time constant is large compared to the "ON" duration of the microbead, a biphasic current pulse can be injected into to the tissue.

The downside of the proposed capacitive stimulation mechanism is the small voltage headroom at the current source node. This limits the stimulus pulse width and strength significantly. In order to increase the voltage headroom a transistor is added between the voltage source and current source (Fig. 4.2(c)). The transistor operates in the linear region when the microbead is "OFF" and cutoff region when the microbead is "ON", and thus can be replaced by a resistor (R_t) with a switch. Furthermore, because R_v is larger than R_t, at the onset of the anodic pulse (when the current switches direction), the current takes the path of least resistance (going through R_t), resulting in an increase in the anodic pulse strength. Thanks to the capacitive electrodes, the added feedback transistor and the

ON-OFF switching operation of the microbead, charge balancing is automatically applied without the need for a control system.

It should be noted that capacitive currents are not as effective as faradaic currents at triggering action potentials, especially when the strength of the stimuli pulse cannot be adjusted. Fortunately, depolarization of the cell membrane could be enhanced step by step until self-excitation of sodium channels set in as shown in [51]. The study shows that pulse trains of weak capacitive stimuli were able to elicit action potentials in cultured rat neurons, and concluded that weak biphasic stimuli resulted in safer extracellular stimulation.

4.4 Full system efficiency

4.4.1 Measurement Setup

When transmitting large amounts of power at a short distance from the test board, the setup becomes affected by unwanted eddy currents in the PCB traces. Eddy currents induced due to Faraday's law can be minimized in the silicon substrate by using a silicon-on-insulator (SOI) process [52], however, eddy currents in highly conductive PCB traces are much larger and harder to minimize. They generate a magnetic field in the opposite direction of the source field resulting in an attenuated overall field and an induced AC voltage on top of the measured signal generated by the Rx device. A common solution to this problem is to cover the PCB with a high-permeability ferrite sheet which deflects the magnetic flux.

Unfortunately, commercial ferrite shields are not effective at high frequencies in which µm-sized coils need to operate in order to resonate. One method that has found some success in this work is the careful design of the PCB layout. The design techniques that have been applied include:

i) reducing the area of closed metal loops as much as possible,

ii) keeping the number of traces on board to a minimum,

iii) reducing the width of the metal traces to a minimum,

iv) using coax cables to interface with the PCB,

v) prioritizing SMA connectors over headers or large BNC connectors and placing them far from the Tx coil, and

vi) prioritizing wire-bonded dies over IC chip sockets.

Pond pads without ESD protection were used in order to reduce the number of Cu traces on PCB. Fig. 4.3 shows the test boards designed specifically to minimize the EMI. The induced AC voltage has been measured and is found to be 900, 200 and <50 mV, for setups X, Y, and Z, respectively. The Tx coil was placed 5 mm away with a source power of 35 dBm.

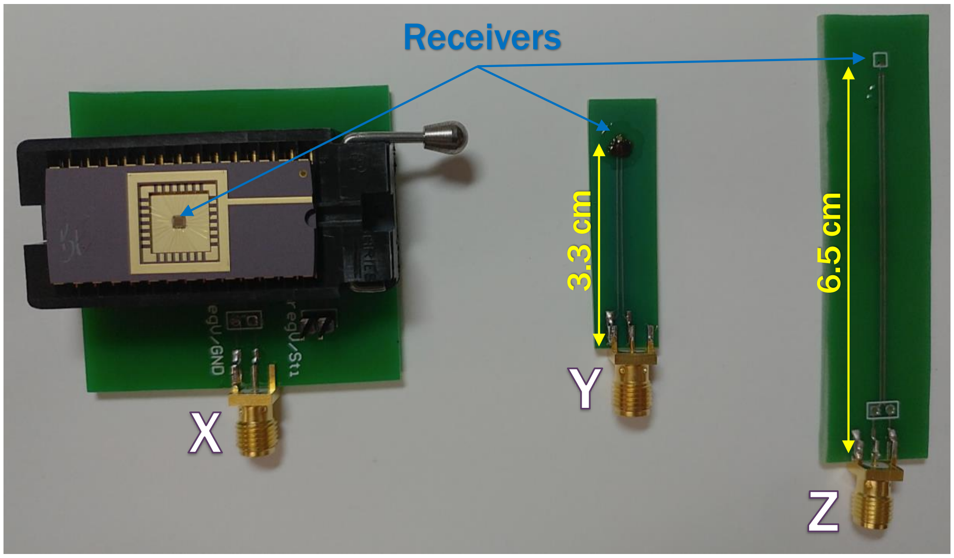

Figure 4.3: Picture of different PCB setups used to measure the regulated voltage generated by the Rx device.

We define the full system efficiency (η_{total}) as the ratio of power delivered to the resistive load to the transmitting source power set by the power generator. The overall measure thus includes several loss factors which are the power loss: *i)* in the Tx coil (η_{TxCoil}) which also includes that of the PA and coaxial cable, *ii)* between the Tx and Rx coil (PTE), *iii*) the Rx coil (η_{RxCoil}) which also includes power reflected by resistance mismatch, and *iv)* the harvesting circuitry (PCE) which comprises a charge pump rectifier, a reference voltage, and a regulator. The product of all efficiencies are given by: $\eta_{total} = \eta_{TxCoil} * PTE * \eta_{RxCoil} * PCE$. Efficiency measurements were obtained by sweeping the source power at 1.18 GHz until the Rx device reached its regulated voltage of 1 V.

Full system efficiency measurements are taken in two different mediums: air and tissue (beef). To mimic the lossy tissue media, the microbead was entirely engulfed in beef by placing the tissue above and underneath the PCB. The CMOS chip was partially encapsulated in epoxy (EPO-TEK 353ND-T) such that the bondwires are protected from the tissue while leaving the microbead exposed. The purpose of this was to create a physically contact between the wet tissue and the microbead, as would occur in a real scenario. Two microbead versions were used during this experiment, one containing a coil diameter of 200 µm and the other 300 µm.

4.4.2 Measurement Results

The area of the entire 200 µm microbead, measures 200 × 200 µm^2 as shown in the micrograph (Fig. 4.4). The on-chip coil and metal-insulator-metal (MIM) capacitors conceal the circuit blocks underneath.

To estimate the stimulus pulse shape/width, it is important to know how reactive the 200 µm microbead is to an RF pulse. Measurement results (Fig. 4.5) show that it takes about 20 µs (the first vertical dashed line represents the onset of an RF pulse) for the mirobead to reach a steady regulated voltage of 1.2 V, while it is wiressly powered and stimulating. This rise time is larger than that shown in post-layout simulations (~ 5 us) because of the omitted parasitic capacitances introduced by the measurement setup, mainly from the coaxial cable (~60 pF) and the oscilloscope input (~15 pF). To show this, a 75 pF capacitor has been added at the output of the microbead, leading to the same rise time of 20 µs. It is important to note that the measurements are taken without the electrodes, which modify the pulse shape because of the double layer capacitance formed with the electrolyte. The addition of electrodes and their influence are covered in the following sections.

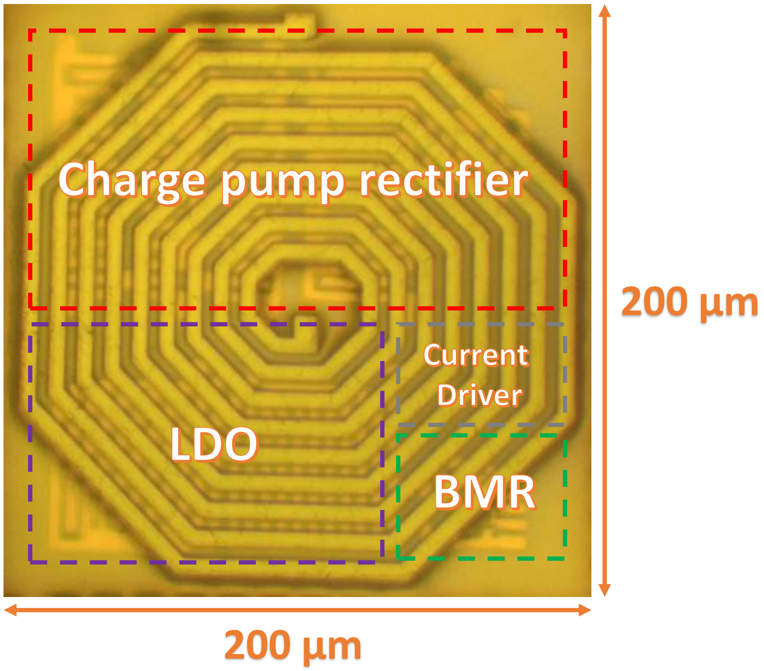

Figure 4.4: Micrograph of the microbead with annotations for the circuit blocks. The coil and the capacitors sit on top of the circuit.

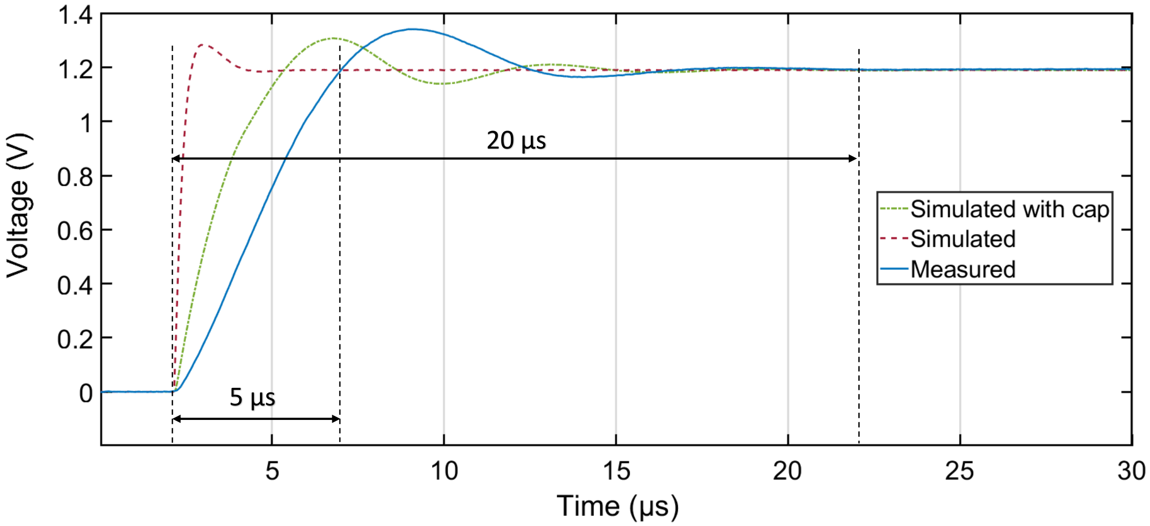

Figure 4.5: Measured and simulated close up waveforms of the regulated voltage when the microbead is wirelessly powered.

Fig. 4.6 shows the correlation between the output power from the signal generator (at 1.3 GHz) and the unregulated voltage (V_{unreg}) when a 200 µm microbead is not stimulating. V_{unreg} is the voltage generated by the charge pump rectifier. The distance between the Tx and Rx coil was set to 7, 8 and 9 mm, making the RF wave propagate through FR4 (1.6 mm), air (1.4 - 3.4 mm), and beef tissue (4 mm).

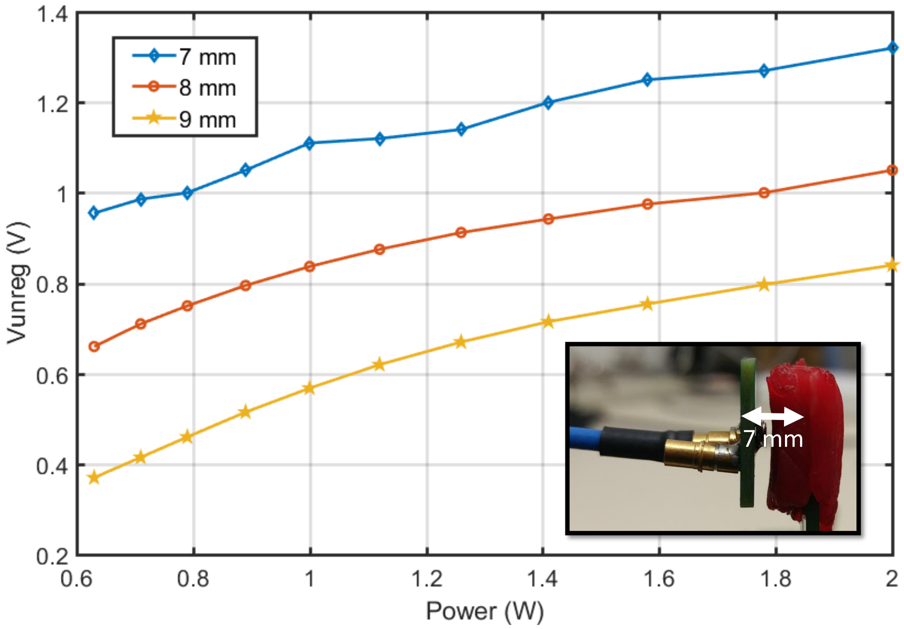

Figure 4.6: Measured unregulated voltage versus different power levels for a coupling coil distance of 7, 8 and 9 mm.

Fig. 4.7 shows the measured overall efficiency as the 300 µm microbead is moved away from the Tx coil. The amount of power delivered to the load (PDL) is changed four times to demonstrate the PCE dependence on the stimulus amplitude. As stimulation is an energy-intensive function (much greater than neural recording), large PDL values were chosen. This particular charge pump rectifier performs better as the source power increases.

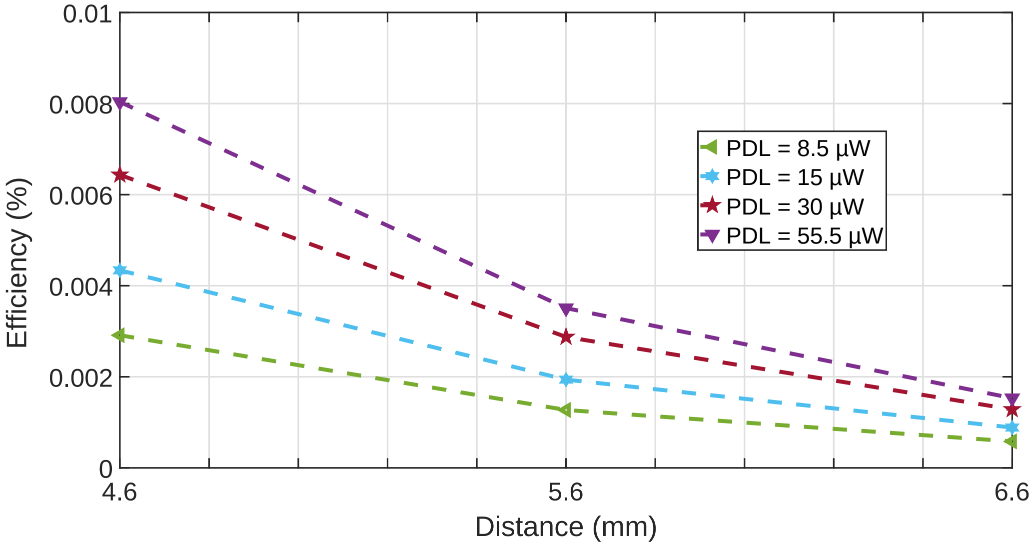

Figure 4.7: Measured efficiency as a function of Tx-Rx distance for different PDL values.

Fig. 4.8 shows the measured overall efficiency when tissue with a thickness of 5 mm is placed between the Tx coil and the 300 µm microbead, and 2 cm of tissue placed underneath the PCB. This experiment is done for two reasons: emulate to some extent the performance of a microbead in the cortex and quantify the difference between air and tissue medium. Although some of the transmitted power is lost in tissue, the setup with tissue still performs better compared to that with air. The exact reason for this unusual response is still unknown, but it important to note that the medium is considered during the design of the microbead. Thus, the resistance of the coil is better aligned with that of the rectifier when tissue is present, leading to less signal reflection caused by mismatched impedances.

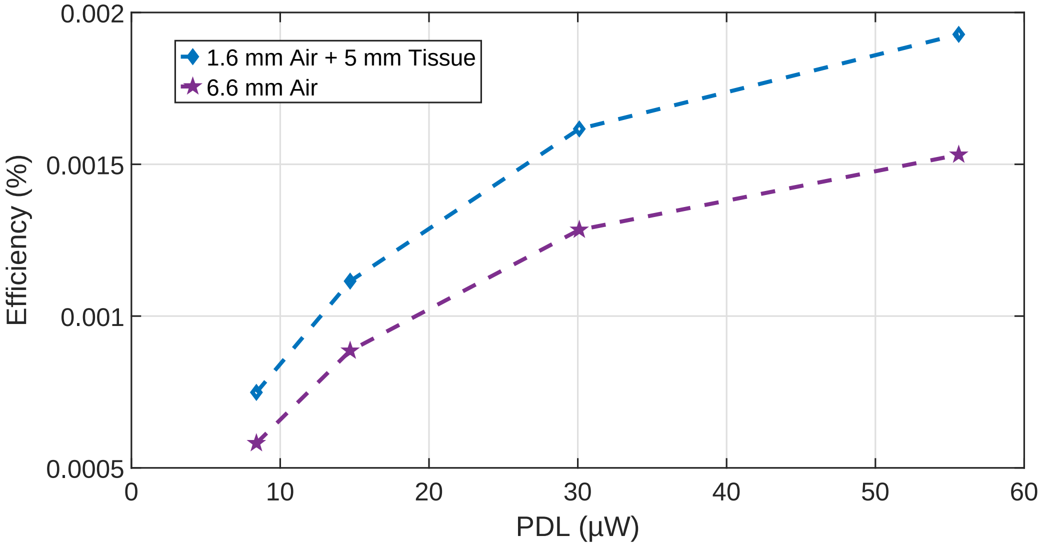

Figure 4.8: Measured efficiency in air and tissue as a function of PDL for a Tx-Rx distance of 6.6 mm.

Table 4.1 compares the wireless powering efficiency of the microbead with that of state-of-the-art ultra-small receivers (≤ 0.5 mm^2). A straightforward comparison is difficult as the Rx coil area, Tx-Rx distance and medium are all different from one another. In order to make a fair comparison with other published results, an FOM has been proposed in [46]:

$$FOM = \frac{\eta \times d^3}{A^{1.5}}$$

where, d is the Tx-Rx distance, and A is the Rx coil area.

It is important to note that although this FOM is widely used in the field when Rx coil dimensions are much smaller than the Tx coil, it does not take into consideration the operating frequency, the wireless system, the PDL, and the medium.

Table 4.1: Wireless powering performance specifications of the microbead in comparison to other state-of-the-art ultra-small receivers ($\leq$ 0.5 mm^2).

Ref.	Rx coil area (mm^2)	Rx coil type	Tx-Rx distance (mm)	Wireless system	Medium	FOM	η_{total}(%)
[53]	0.5	On-chip	0.5	2-coil	Air	0.013	0.038 2.5 GHz PDL = 94.7 µW
[54]	0.25	On-chip	8	3-coil	Liquid phantom	77	0.019 915 MHz PDL = 95 µW
[47]	0.125	On-chip	1	2-coil	Air	0.48	0.021 1.5 GHz PDL = 10.5 µW
[55]	0.01	On-chip	2.2	2-coil	Air	53.2	0.005 4.8 GHz PDL = 100 µW
This work	**0.09**	**On-chip**	**6.6**	**2-coil**	**Tissue (beef)**	20.4	**0.0019*** **1.18 GHz** **PDL = 55.5 µW**

* in addition to the rectifier, the PCE also includes the efficiency of the charge pump, voltage reference, and voltage regulator.

4.5 Misalignment analysis

Most studies conducted on wirelessly powered implants assume ideal scenarios where the Rx coil is perfectly aligned with the Tx coil, but in reality, misalignment occurs (particularly in the application of implantable medical devices) and is one of the major drawbacks of resonant near-field coupling. This section of the thesis studies the impact of lateral misalignment on the PTE [37].

4.5.1 Measurement Setup

Because this work deals with µm-sized receivers, the measurement misalignment setup needs a highly accurate center to center alignment and displacement. As shown in Fig. 4.9, this was achieved by having multiple PCB through holes (1 mm in diameter) which were used to insert precisely made 3D printed photopolymer spacers in order to guarantee a certain distance between the two PCBs. To improve the repeatability and stability of the setup, four spacers were placed on all four sides of the PCB. Headers were printed instead of plastic screws to save time when scanning along the x and y-axis. The Tx and Rx coils are fixed in parallel planes, separated by 4.6 mm, and the center of the Tx coil is displaced by a distance Δx and Δy. Measurements are done in air with a 300 µm microbead.

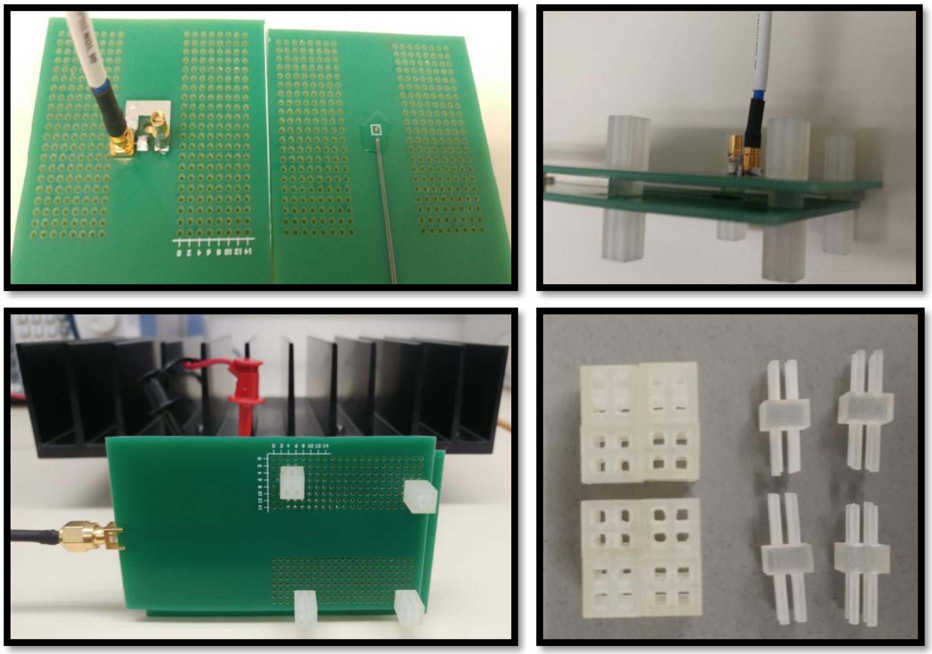

Figure 4.9: Pictures of the setup components used to obtain misalignment measurement results.

4.5.2 Measurement Results

Fig. 4.10 depicts the misalignment measurement efficiencies of the Rx device when a load resistance of 120 kΩ is connected to it. The 3D plot does not have a symmetrical shape since the Tx coil symmetry is broken by the added connectors and capacitors. Based on the measurement results, misalignment is less forgiving here than with larger conventional coils since at $\Delta x = 2$ mm, η_{total} already decreases by 50 %. This is expected because it only takes a displacement of 5.5 mm for the Rx device to no longer be directly underneath the Tx coil. Unfortunately, increasing the Tx coil diameter would lead to a decrease in PTE as there is an optimal diameter for every Tx to Rx distance. With the addition of angular misalignment, µm-sized receivers would become too big of a challenge to power. Chapter 5 proposes a solution to the misalignment complication.

Using the same approach, setup C (Table 2.2) was also implemented to study the impact of the seal edge. Measurement results showed a decrease in efficiency of 64% compared to setup B, which is good agreement with the simulation results shown in Fig. 2.9 (~60%).

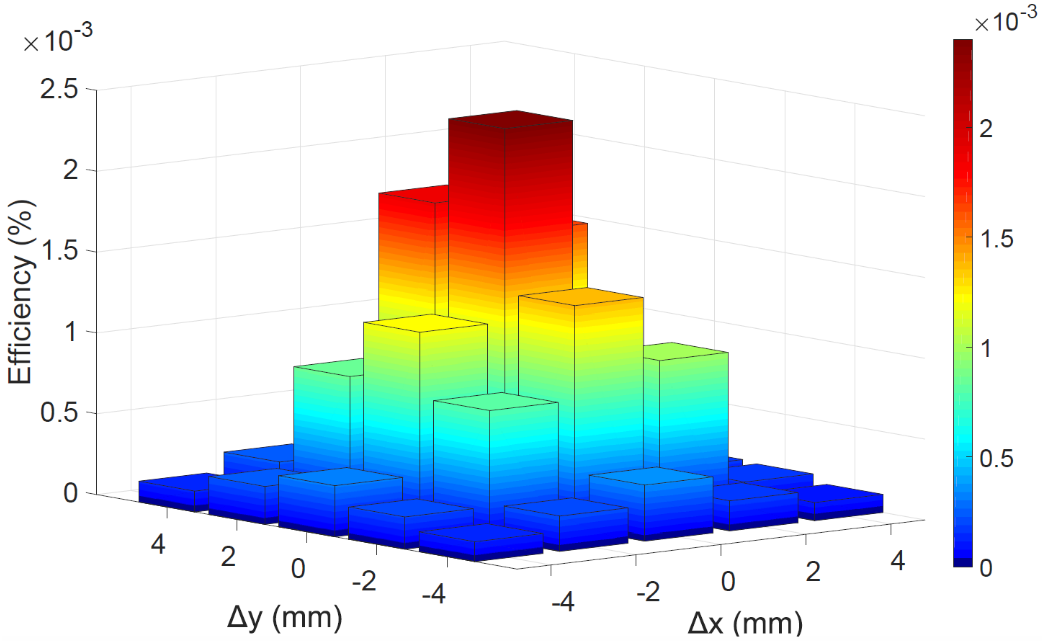

Figure 4.10: Measured overall efficiency as a function of lateral misalignment.

4.6 Implant Electrode Integration, Packaging, and Implantation

Wirelessly-powered neural interfaces are usually made of an assembly of multiple different components, such as an off-chip coil (or crystal if ultrasound powering is used), an ASIC chip, electrodes and surface mount capacitors. The conventional methods used to connect these components (e.g., flip-chip bonding, wire-bonding and conductive epoxy) increases the volume of the implant and decreases reliability. Therefore, the bulky external parts and the interconnections significantly limit the extent of miniaturization of the packaged implant. The key to solving this issue is to use microfabrication integration techniques [38]. A process flow that incorporates all these separate parts into the ASIC chip is shown in the following sections, it is designed such that the microbead does not increase in volume after the electrode integration.

4.6.1 Fabrication Process

After receiving the 1.5 mm × 1.5 mm dies from the foundry (Fig. 4.11(a)), the chips are diced again (while focusing on their edge quality) such that the microbead exposes the top aluminum metal on two sides of the die to act as stimulation electrodes (Fig. 4.11(b)). The electrode dimensions are 4 μm × 200 μm.

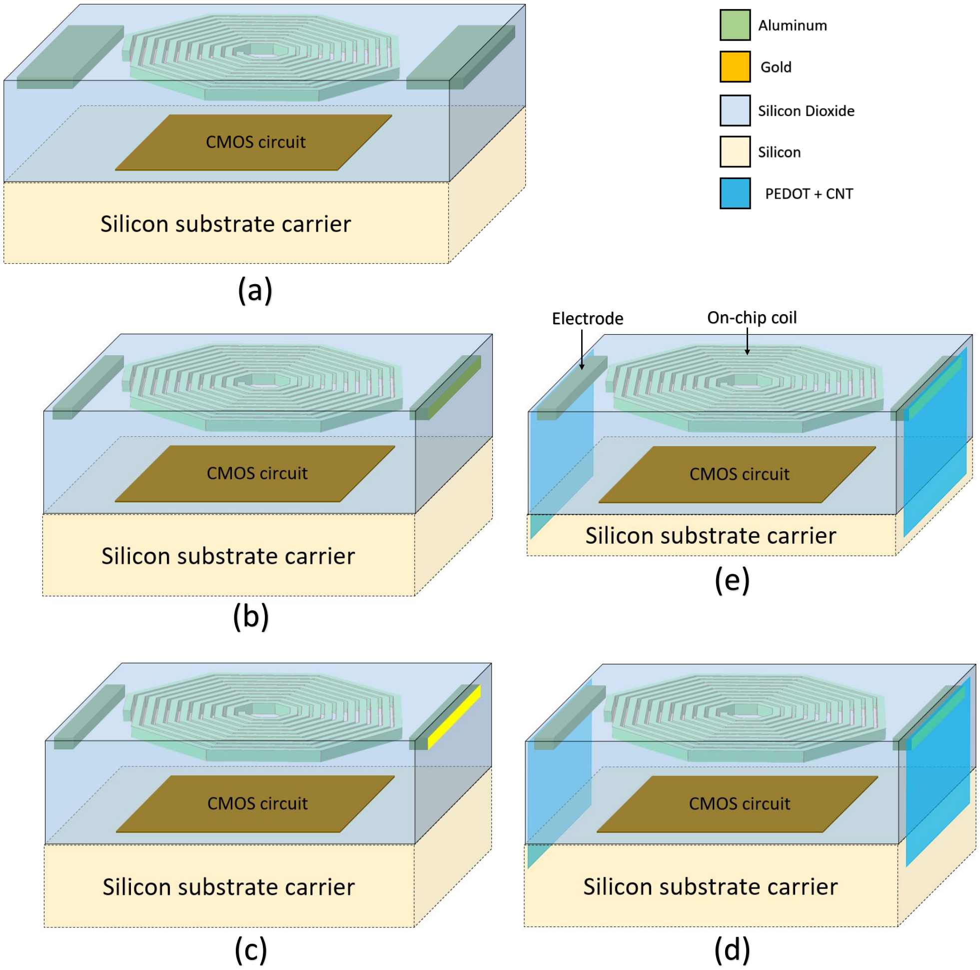

Figure 4.11: Process flow diagram of the microbead electrode integration.

A Zn/Ni/Au stack is deposited on both electrodes (Fig. 4.11(c)) using an electroless process (Fig. 4.12) which consists of a series of steps: zincation, nickel deposition, followed immersion gold deposition. Zincation is used to improve the uniformity of the Ni layer and to prevent further oxidation. The sodium hydroxide in the bath removes the native oxide on the Al electrode. The Ni layer provides mechanical backing for the Au layer.

During gold immersion, a displacement reaction occurs in which Ni atoms are replaced by Au atoms. Trisodium citrate and ammonium chloride are added into the bath to act as the complexing agent and stabilizer, respectively. After each step, the die is rinsed in DI water.

Poly-ink HC is then deposited onto the Au electrodes through inkjet printing (Fig. 4.11(d)). The poly-ink HC, purchased from POLY-INK, contains an aqueous mixture of conductive polymer and carbon nanotube (CNT), combining the good process ability of PEDOT-PSS with the high conductivity of CNT. It has been shown that PEDOT-CNT electrodes offer the possibility to stimulate tissue at relatively low voltage and that its adhesion on gold is excellent [56, 57]. The poly-ink dispersion is passed through a glass fiber syringe filter with a pore size of 0.7 µm and degassed for a few minutes to remove trapped air bubbles before it is loaded into a cartridge. A Dimatix Fujifilm DMP 2800 inkjet printer with 10-pl drop volume cartridges is used. To guide the printing process, images of the microbead were taken on both sides using an optical microscope. One side of the silicon-based die is cleaned using oxygen plasma (Technics Micro-RIE Series 800, 150W, 200 torr, 45s). Printing is first done on photo paper to tune the droplet morphology. Multiple cleaning cycles and voltage adjustment were applied until the trajectory of the droplet is stable. The microbead is transferred carefully with a tweezer to a carrier glass slide with the electrode side facing up. Droplet (drop-to-drop spacing and size) and jet (speed and frequency) settings were chosen based on trial and error. The cartridge and microbead temperature are set to 28°C. The printed line measures 0.02 mm^2 (other dimensions have been printed as well) and completely covers the Au electrode. After baking the die on a hotplate, it is gradually cooled to room temperature and flipped over with high precision tweezers. The same process is repeated on the other side of the microbead to coat the second electrode.

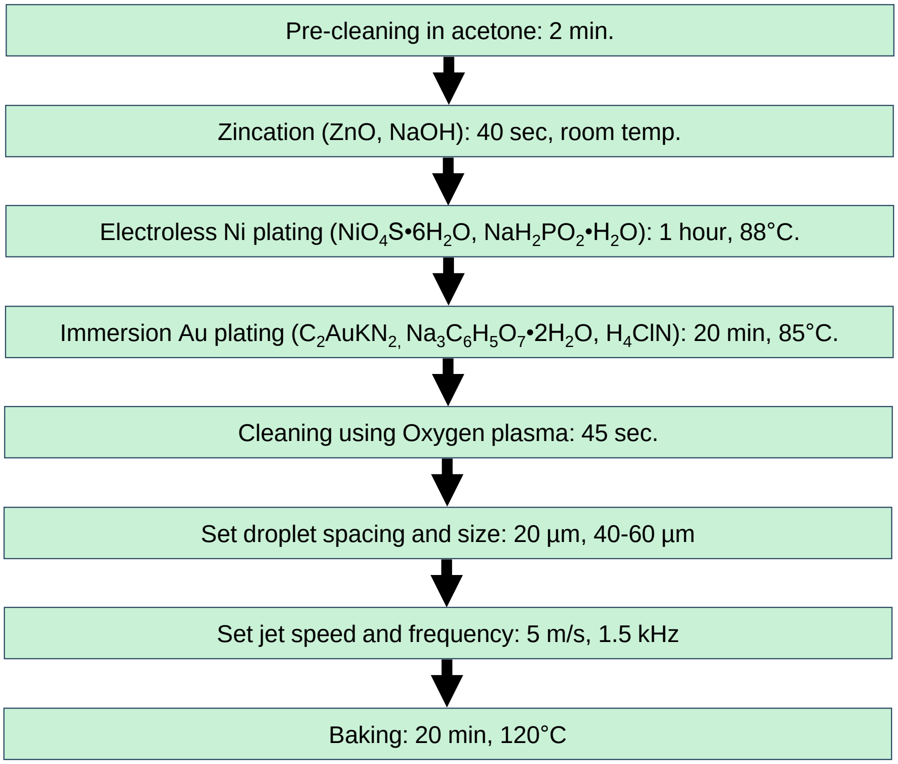

Figure 4.12: Flowchart of the complete electroless process and the deposition of PEDOT/CNT.

Once the electrode post-processing is completed, the microbead is thinned down to 80 µm, removing approximately 180 µm of silicon (Fig. 4.11(e)). This is done using the Multiprep polishing system by Allied. The die is mounted on a small polished metallic stub (prepared in-house) which is mounted on the fixture using thermal wax heated to 150°C. Since the silicon surface area that contacts the stub is small, the wax is not able to hold the die in place during grinding. Therefore, in order to increase the contact surface area, the microbead is squeezed between two larger dies. The metallic fixture is then fixated onto the polishing system, and the diamond lapping film placed on the platen. The surface roughness of the diamond film (15 µm) is chosen such that the bottom surface of the silicon is rough in order to better anchor the microbead in tissue. The grinding process is interrupted after 10 sec in order to calculate the silicon removal rate. The total grinding time is 50 sec at a speed of 100 rpm. The final dimensions of the microbead are 340 µm × 330 µm × 80 µm, giving it a volume of approximately 0.009 mm^3 (Fig. 4.13).

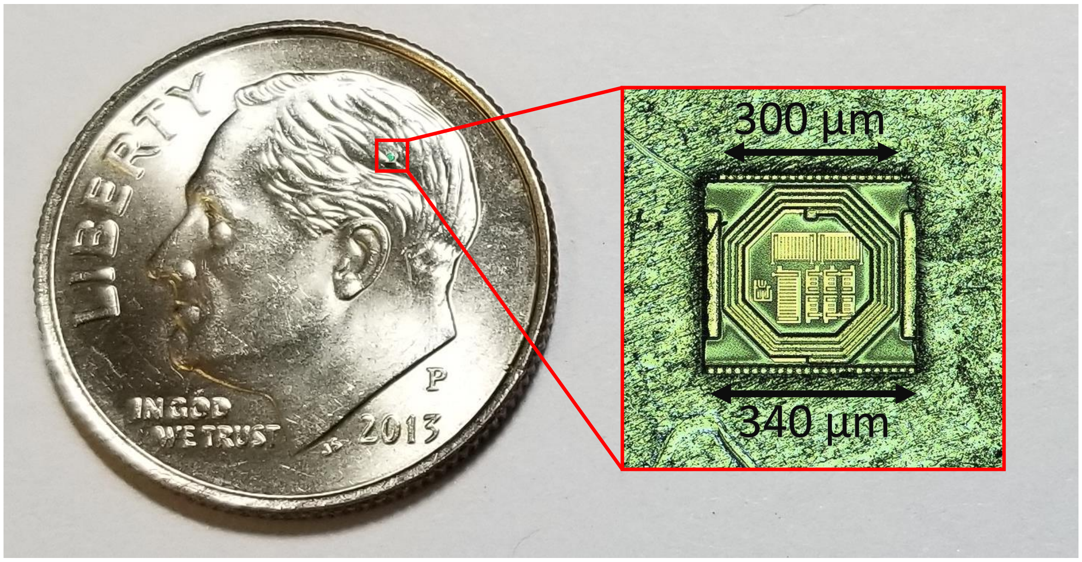

Figure 4.13: Micrograph of the microbead with the integrated electrodes. A U.S. dime is shown as a scale reference.

4.6.2 Results and Discussion

The described process flow is simple and relatively inexpensive to implement as it does not require a micro-fabrication facility. It is important to note that the fabricated prototype is intended for acute experiments and will need a hermetic biocompatible coating to survive the harsh tissue environment. To provide lifetime longevity, thermally grown, thin layers of exceptionally high-quality SiO_2 can be integrated on ultra-small IMDs [58]. However, this step is not a priority in the initial stages of this work as there are more important challenges to address first. The fabricated microbead relies on the native oxide (on the remaining silicon bulk) to prevent short circuits from occurring in tissue, however, the oxide is not thick enough (< 3nm) to prevent small current paths between the electrode and grounded substrate. The leaked current is estimated to be only a few microamps, which is large enough to make a noticeable impact on the overall system efficiency. This issue can be solved by porting the device to a silicon-on-insulator (SOI) process as described in detail in Chapter 6. As each microbead is manually handled, the proposed process flow is not designed for efficient fabrication of hundreds of these implants and thus the process flow needs to be modified during more advanced stages of this work.

Once post-processing is complete, the microbeads can then be inserted at a desired depth and location in the brain. If the tissue damage is substantial during the insertion of the microbead into the CNS, the astrocytes will encapsulate the implant and increase the tissue impedance which diminishes the ability to stimulate. Fortunately, the microbead is small enough to enable direct injection into the target brain region via a syringe needle with an inner diameter of 0.4 mm (Fig. 4.14). During a stereotactic surgery, this method allows for precise and minimally-invasive insertion into the cortex and subcortex. Nevertheless, further studies are needed to investigate the induced tissue reactions with the proposed insertion method.

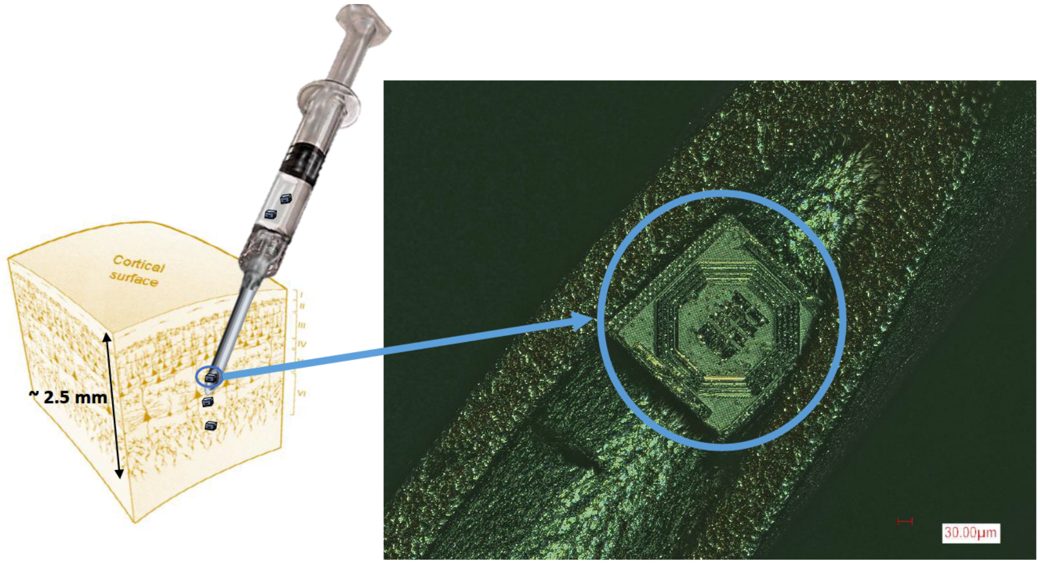

Figure 4.14: The packaged microbead which is entirely implanted into the brain by means of a syringe with a 22G needle.

Micrographs of the microbead's surface, which contains one of the two electrodes, at different stages of post-processing are shown in Fig. 4.15. The microbead makes use of surface electrodes as there is no need for 3D electrodes since the whole system is implantable and can be placed close to the target neuronal population. Besides, high aspect ratio implantable electrodes, such as those used for deep brain stimulation/recording, are difficult to fabricate as they require a biocompatible material with a large Young' s modulus to survive the insertion without mechanical failure. It is important to note that a CMOS process that provides aluminum metal should be chosen as copper is harmful and would cause tissue necrosis. Having the electrodes on the sidewalls of the CMOS die maximizes the anode-cathode separation and thus the stimulation effect. Similarly, the recording and reference electrode separation is also maximized, minimizing the signal to noise ratio of the recording signal. As for the area of the electrode, although the width of the surface CMOS electrode is determined by the metal used, its area is significantly increased by the added conductive ink. The optimal area depends on the CNS bipolar stimulation application as there is a link between the size of the electrode and the number of activated neurons. Furthermore, one should keep in mind that a smaller electrode will lead to a larger electrode impedance, and thus larger voltage compliance. For these reasons, different electrode sizes were fabricated in this work. Microbeads of different thicknesses (63, 80, 114, 130, and 146 µm) were successfully fabricated, Fig. 4.15(d) shows the thinnest of them all. As the ratio of the implant's length to the implant's thickness increases, the ASIC chip becomes more fragile and thus harder to handle.

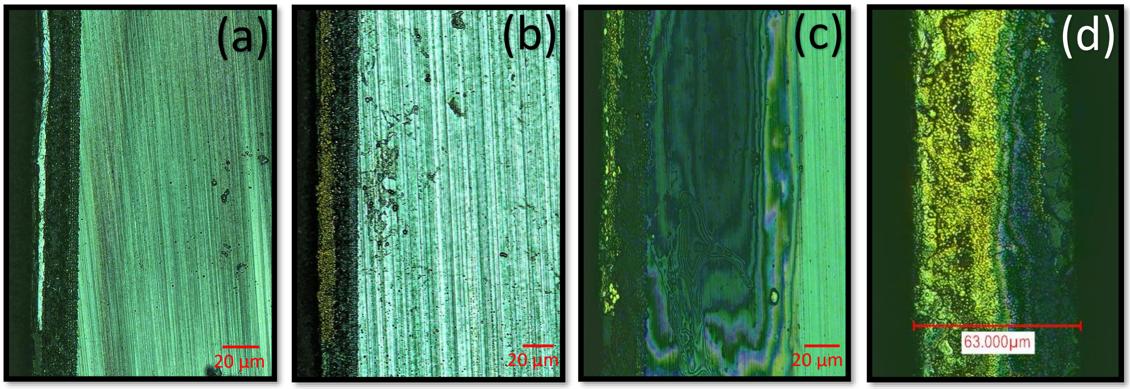

Figure 4.15: Micrographs of the microbead at different stages of post-processing: (a) after dicing, (b) after Au immersion, (c) after Poly-ink printing, and (d) after backside thinning.

Conducting polymers have been often utilized to improve the performance of planar electrodes. In this research, Poly-ink HC has been used to significantly decrease the impedance of the electrodes. However, depositing PEDOT-PSS directly on aluminum will cause unwanted chemical interactions. Therefore, Au is first deposited in order to better interface with the Poly-ink and prevent aluminum from corroding in tissue. PEDOT-PSS deposited using electrodeposition was not possible for the microbead as having to physically contact the microbead in a liquid will significantly increase the complexity of the fabrication process flow. It is for that reason that the polymer is deposited using ink jet printing, an unconventional technique but an effective one in this situation.

The maximum electrode area is determined by the thickness of the microbead and thus the silicon removal step. A larger electrode surface area will increase the current peak of the stimulation pulses but will reduce to maximum stimulation rate (as it takes longer to charge and discharge the electrode capacitance). A 0.02 mm^2 electrode strikes a good balance between the two as can be noticed from generated current pulses as shown below. The neural interfacing application also determines the electrode area, for instance, applications focusing on selectivity and resolution would require a smaller stimulating electrode area in order to recruit fewer neurons.

Using the VSP-300 potentiostat, a two-electrode system was implemented for the electrochemical impedance spectroscopy (EIS). Poly-ink served as the working electrode and a large Pt electrode as the counter electrode. A PDMS (1:10) chamber was glued onto printed Poly-ink lines (with different surface areas) by using low toxicity silicone adhesive (World Precision Instruments) and filled with 1x phosphate-buffered saline (PBS). Outside the chamber, a thin copper wire was connected to the poly-ink line with eutectic gallium indium (EGaIn). The EIS measurements were made over a 1-10^5 Hz frequency range using a 10 mV sinusoidal excitation voltage. The impedance spectrum is presented as Bode plots using log spacing for |Z| and frequency.

Fig. 4.16 illustrates the EIS plot for 3 electrode surface areas: 0.05 mm^2, 0.025 mm^2, 0.02 mm^2, with impedance (at 1 kHz) of 3.8 kΩ, 5.9 kΩ, and 8.2 kΩ, respectively. At low frequencies, the Poly-ink exhibits a predominantly capacitive phase angle (-80°), thus the electrode typically behaves like a capacitor. Capacitor electrodes provide a safer stimulation mechanism as they rely on charge redistribution rather than charge transfer. The equivalent circuit model of the electrode-electrolyte interface of the 0.02 mm^2 electrode is shown in Fig. 4.16, in which R_s is the spreading resistance, C_{dl} is the double layer capacitance. Both parameters heavily depend on the surface area of the electrode. Due to the non-ideal capacitance response, C_{dl} can be replaced by CPE, a constant phase element, however, for simplicity it is kept as it provides a satisfactory fitting curve as shown in Fig. 4.16. By using low-impedance electrodes, the microbead can operate with a V_{DD} of 1 V. A much larger regulated voltage would have been problematic since the charge pump rectifier would have needed more stages resulting in a decrease in PCE, and thus increase in power transmitted.

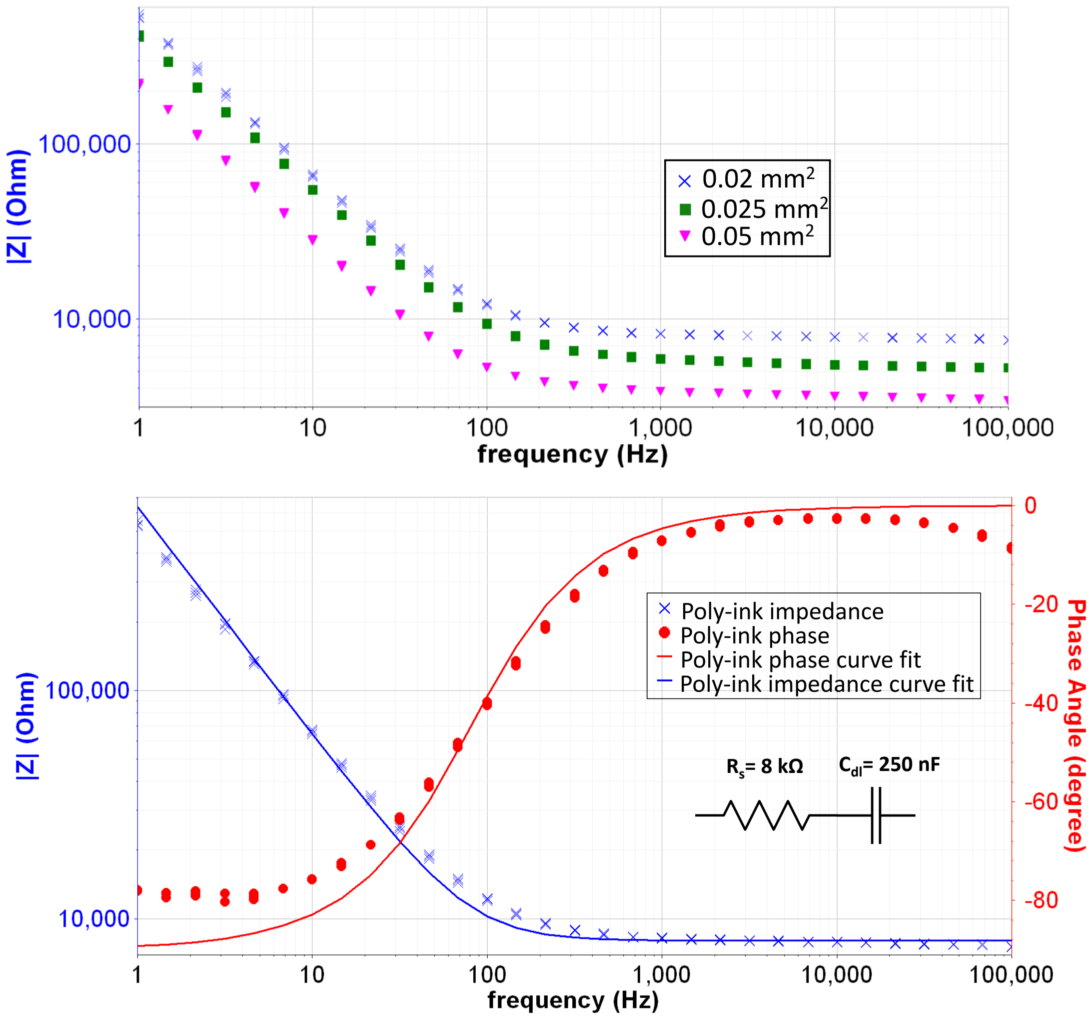

Figure 4.16: Impedance measurement bode plots of: (top) Poly-ink electrodes of 3 different dimensions and (bottom) a 0.02 mm^2 Poly-ink electrode with the equivalent circuit model of the electrode-electrolyte interface.

The 200 µm × 4 µm Al electrode impedance before post-processing was also measured in order to show that it would not have been possible to stimulate without lowering its impedance. This was done by wire-bonding the microbead on a PCB and partially encapsulating it with epoxy (Epo-Tek 353ND) such that only the integrated Al electrode is exposed to PBS (Fig. 4.17). An EIS is then performed similarly to that with poly-ink to construct the electrode-electrolyte equivalent circuit model (Fig. 4.17). The equivalent circuit model is more complex than that of the poly-ink because of the formed alumina in PBS. R_t is the charge transfer resistance, R_f is the resistance of the alumina and accounts for defects which creates conductive pathways in the insulating material, and C_f is the oxide layer capacitance. The impedance at 1 kHz is 1.6 MΩ and increases with time as the thickness of the alumina does not stay constant in PBS.

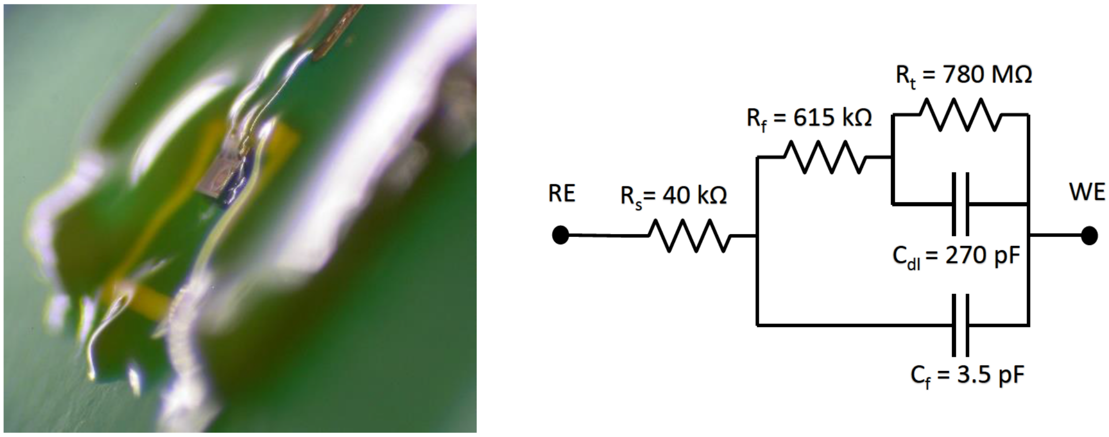

Figure 4.17: Picture of the partially encapsulated wirebonded microbead and an equivalent circuit model of the electrode-electrolyte interface of the untreated Al electrode.

The Poly-ink electrode equivalent circuit model has been implemented using discrete passive components (250 nF, 8 kΩ, 8 kΩ, 250 nF) to measure the stimulation current of the microbead while being wirelessly powered. The generated current pulses provide a good idea of what to expect when the microbead is implanted in tissue. The Tx coil was placed 7.6 mm above the microbead and the power amplifier supplied 36 dBm of power to the

Tx coil at 1.18 GHz. The RF power pulse had a frequency of 5 Hz and a pulse width of 500 us. After transmitting four pulses, the frequency was changed to 50 Hz. Fig. 4.18 shows a single current pulse with a width of 500 µs and a peak current amplitude of 38 µA, leading to a calculated injected charge of 18 nC (0.09 mC/cm^2) which is more than what is typically needed to activate neurons in the CNS and is well below the charge injection capacity reported for PEDOT [59]. The injected charge can be significantly increased (i.e, > 60 nC) if more is needed as the required charge to elicit an action potential is not a fixed quantity since it depends on multiple parameters such as the distance between the electrode and target neural structure, the shape of the stimulus pulse and the properties of the neural tissue. It is important to note that with larger pulse widths or larger transmitted power, the voltage pulse reaches its maximum amplitude of 1 V. Limiting the maximum voltage across the Poly-ink electrode prevents water from hydrolyzing, which will cause damage to the electrodes and surrounding tissue.

Due to the dominant capacitive component of the electrode-electrolyte interface, the current has an exponentially decaying waveform (which can be better observed for larger pulse widths). After the microbead is turned OFF, at the end of the monophasic stimulation pulse, both electrodes discharge over a time course determined by the tissue resistance and electrode capacitance. As can be noticed from the figure, the voltage at the electrode (which is the regulated voltage) discharges very slowly, fortunately, this does not prevent the microbead from reaching stimulation rates over 200 Hz, covering the high frequency bands used for clinical applications such as the treatment obsessive compulsive disorder, depression, and Parkinson's disease. However, this comes at the price of smaller current peaks (< 30 μA), since the voltage across the electrodes is diminished. A form of biphasic stimulation is implemented in one of the microbead versions to address this issue.

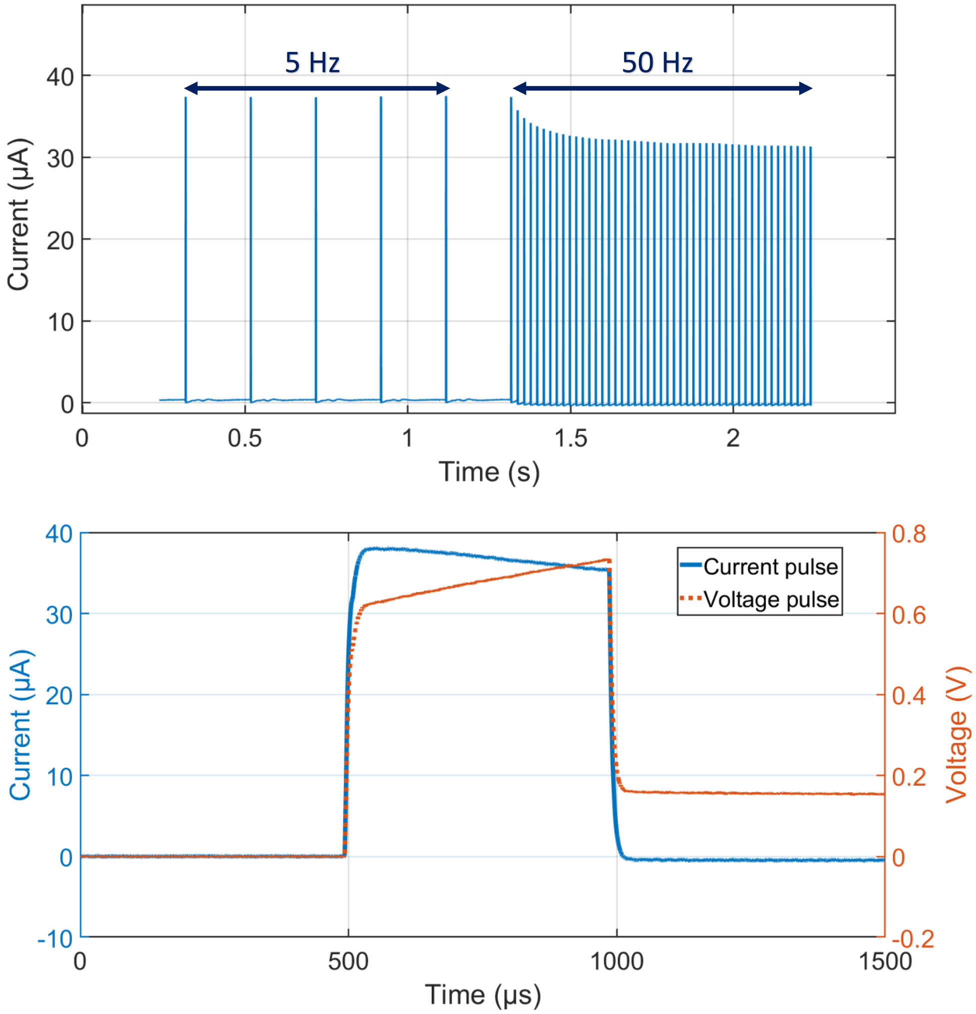

Figure 4.18: Measured monophasic current pulse(s) of the microbead in voltage-mode stimulation, while being powered wirelessly and connected to the electrode-electrolyte equivalent circuit model. (Top) current pulses at 2 different frequencies, (Bottom) zoomed-in view of a single current and regulated voltage pulse.

4.7 Standalone validation in PBS

4.7.1 Measurement Setup

The purpose of validating the free-floating microbead in a conductive aqueous environment is to show: *i)* that it can still be turned ON while currents are leaking into the substrate (as the implant is not hermetically sealed with an added coating), *ii)* the ability of native silicon dioxide to act as a barrier against the permeation of water vapor for a short period of time, and *iii)* the formation of a voltage gradient across its Poly-ink integrating electrodes.

Fig. 4.19 shows the setup used for the validation in PBS. The chamber surrounds an MEA that measures 800 µm × 800 µm. The MEA consists of 60 electrodes, each composed of multiple PEDOT pillars. The measured impedance of each electrode is around 200 kΩ. The microbead is dropped inside the chamber containing 1x PBS. Since the silicon chip is floating on the surface of the PBS, the microbead is not aligned with the Tx coil and its location is unpredictable. Therefore, a MEA was used instead of a single electrode pair in order to guarantee that at least one PEDOT electrode is located directly underneath the implantable device. Two Intan chips (RHD2164, Intan Technologies Inc., USA) were used to amplify and digitize the acquired signal coming from 60 recording channels. The commercially available chip was chosen as it offers programmable sampling rate and filtering along with high input impedance, accurate gain, and good common-mode signal rejection. An XEM 6010 Opal Kelly board then receives the processed signal and transfers it to a computer. The whole setup is battery powered in order to minimize the 60 Hz noise. The Tx coil was placed 1 cm above the PBS surface (and thus the microbead) and the power amplifier supplied 36 dBm of power to the Tx coil at 1.18 GHz. The RF power pulse had a frequency of 5 Hz.

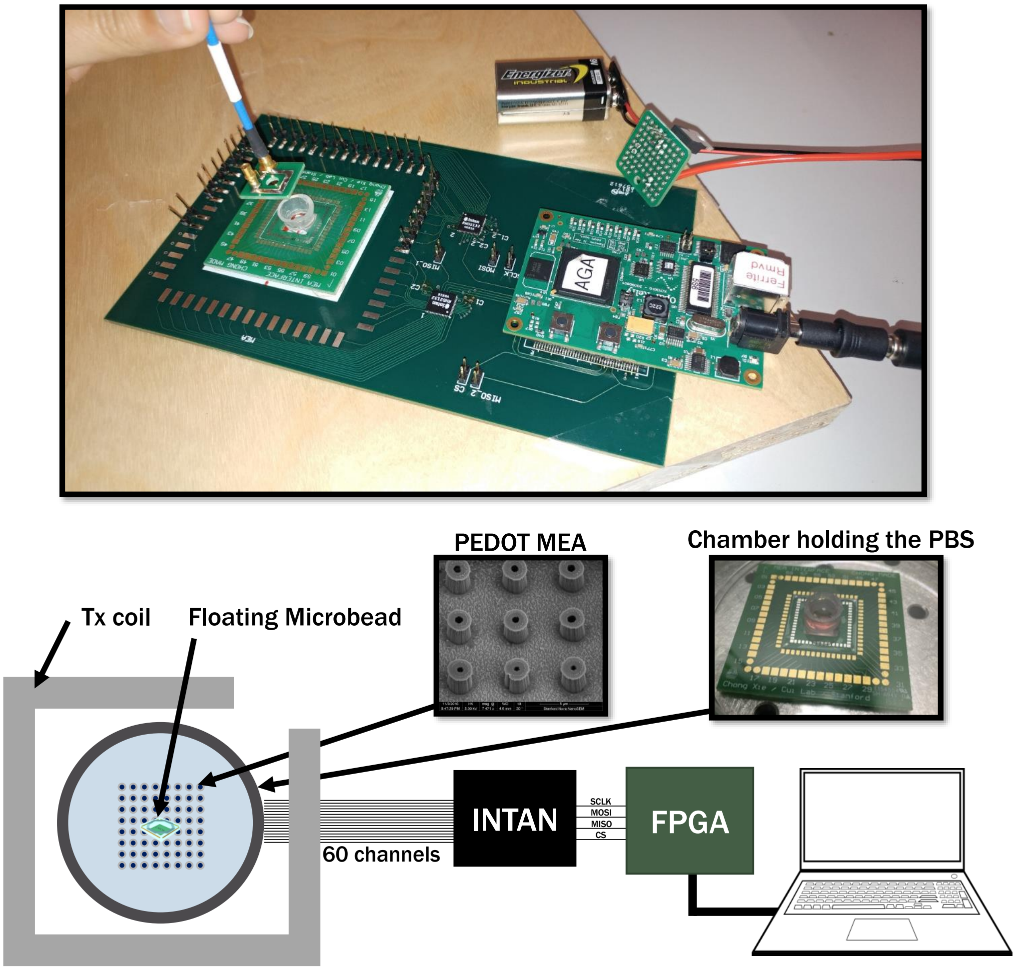

Figure 4.19: Top view of the measurement setup used to indirectly record the voltage generated by the wirelessly powered microbead floating in PBS.

4.7.2 Measurement Results

Fig. 4.20 shows the voltage recorded by the Intan chip using a PEDOT electrode. Although it is not a direct measurement of the voltage generated by the microbead, it does hint that the microbead has reached its regulated voltage of 1 V. This was deduced by replacing the microbead with a pair of electrodes connected to a 1 V voltage source, which resulted in a recording of 5 mV. It can also be concluded that moisture will not damage the implant during acute experiments as the exact same plot was obtained after leaving the microbead in PBS for approximately 6 hours.

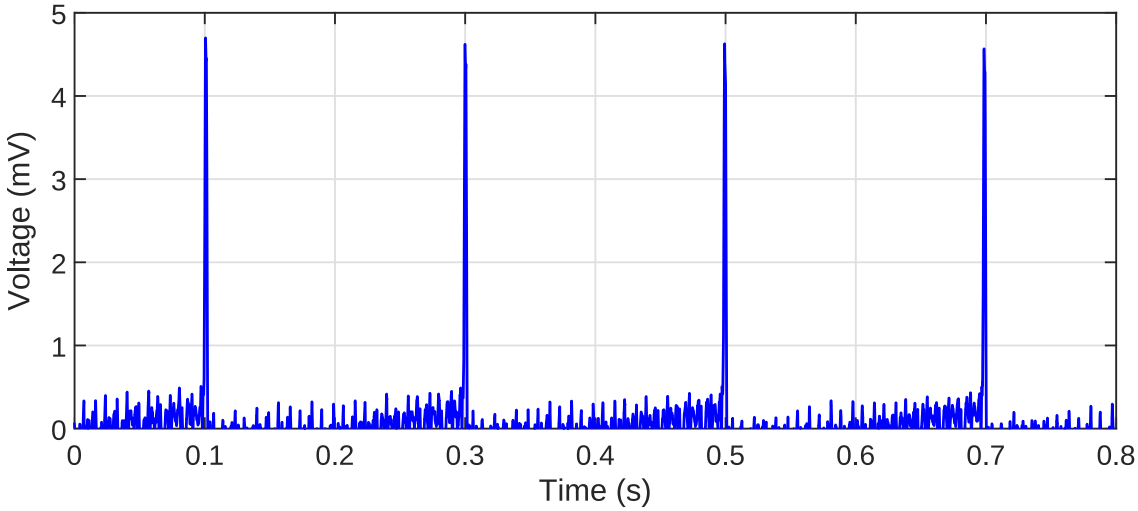

Figure 4.20: Voltage recordings of the Intan chip when the microbead is floating in PBS while being wirelessly powered.

4.8 In-vivo validation

To test the microbead in practical use with the integrated electrodes in a biological environment, an animal experiment has been conducted. The 200 µm microbead was connected to cuff electrodes and evoked leg twitches. The 300 µm microbead was fully implanted in the sciatic nerve and stimulated the sciatic nerve at lower intensities. Although the microbead is designed for the stimulation of the central nervous system (CNS), having the microbead fully implanted in the sciatic nerve of a rat confirms its ability to elicit action potentials in axons.

4.8.1 Measurement Setup

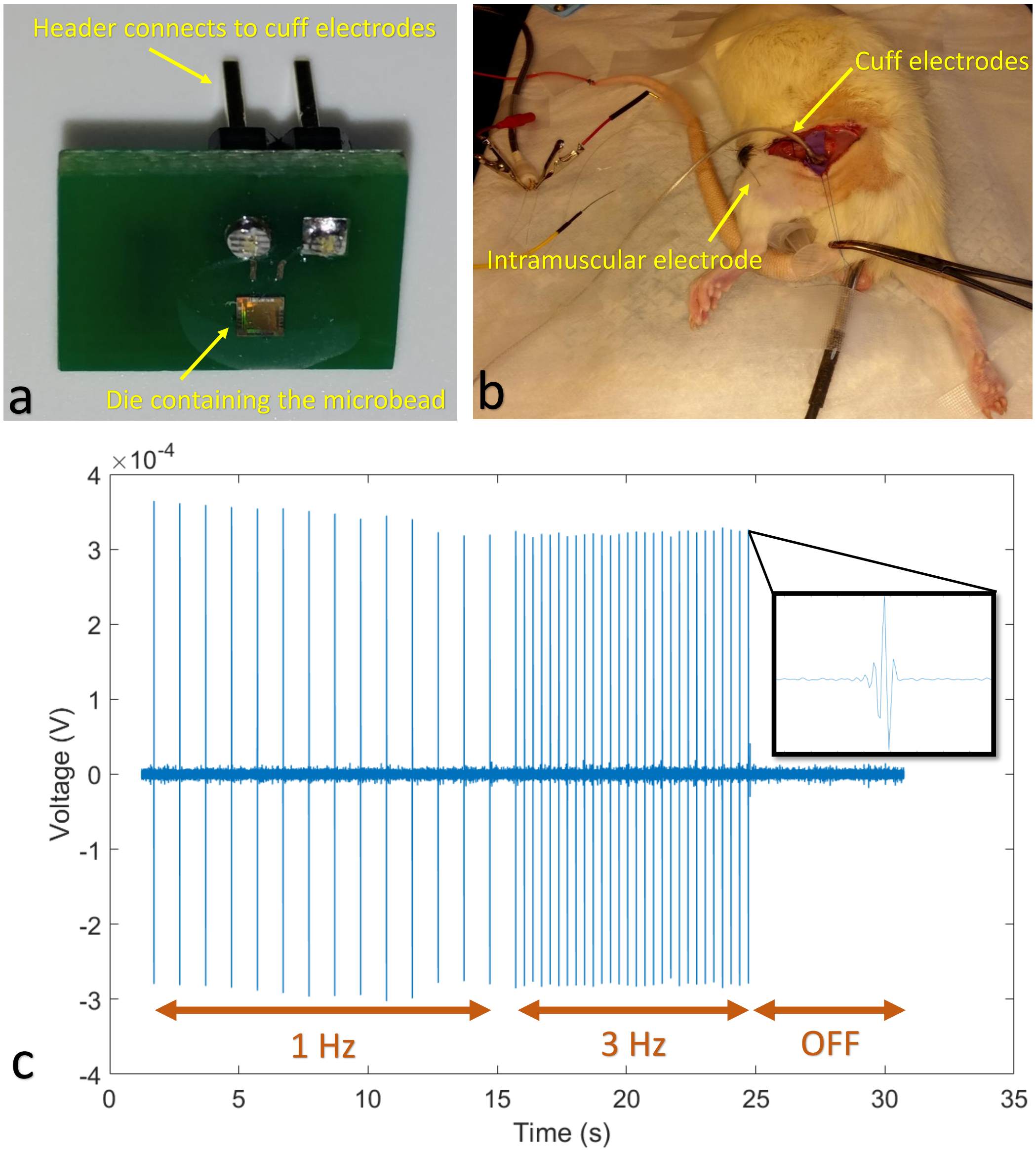

Figure 4.21: a) Picture of the wirebonded 1.5 mm × 1.5 mm die containing the microbead. b) Picture of the anesthetized rat during stimulation. c) EMG response to voltage-mode bipolar stimulation at 1 Hz and 3 Hz.

This experiment was done with the 200 µm microbead which was wirebonded onto a PCB (Fig. 4.21(a)). The surgical procedures used for electrical stimulation and monitoring of peripheral nerves in rats were approved by the Johns Hopkins Medical Institute Animal Care and Use Committee (ACUC). A Male Wistar rat was given an intraperitoneal injection of ketamine/xylazine cocktail (0.1 mL/100g). After dissecting and exposing the left sciatic nerve, a piece of rubber from a surgical latex glove was gently placed under the nerve. A cuff electrode (MicroProbes for Life Science) was placed around it as shown in Fig. 4.21(b). The electrode is made of stainless steel, measures 125 µm in diameter and has an impedance of 10 kΩ at 1 kHz which was measured in [60]. The electromyographic (EMG) activity evoked in the gastrocnemius muscle of the lower leg was recorded using hook intramuscular electrodes (Motion Lab Systems, CA, USA). The signals were amplified and digitized with a preamplifier (RA16PA, Tucker-Davis Technologies, Alachua, FL). The distance between the Tx and the microbead was set to 5 mm and the system was turned “ON” and “OFF” at frequencies of 1 Hz and 3 Hz. An RF signal generator (SMBV100A, Rohde & Schwarz) connected to the power amplifier supplied 36 dBm of power to the Tx coil at 1.3 GHz. In order to control the duty cycle using pulse modulation, a 100 MHz arbitrary function generator (AFG3102, Tektronix) was connected to the RF generator. The delivered monophasic current pulse width was set to 195 µs.

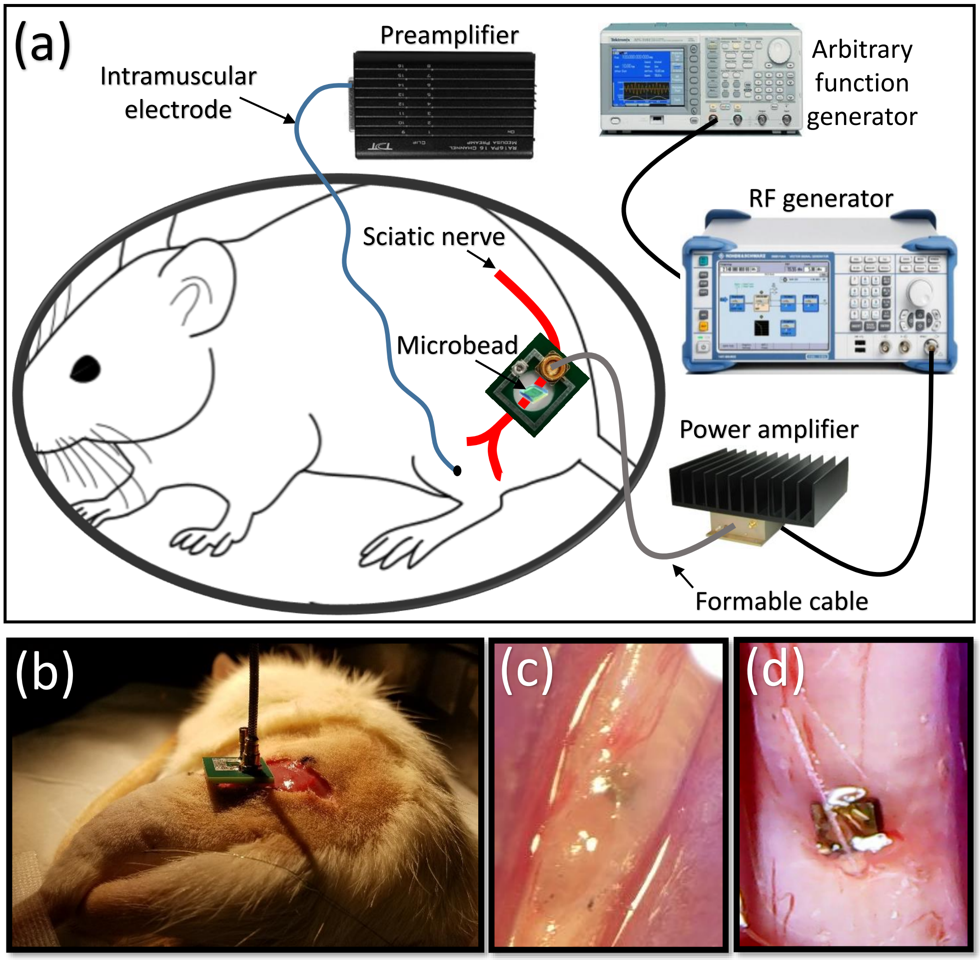

Figure 4.22: (a) Drawing of the experimental setup for *in-vivo* testing. Picture of (b) the anesthetized rat and the Tx coil, (b) the microbead implanted half way through the sciatic nerve, and (d) when implanted at shallow depths.

The surgical procedures are similar for the 300 µm fully implanted microbead. A pocket was created on the side of the nerve, large enough for the microbead to slide in. The Tx-Rx distance is estimated to be around 5 mm. After positioning the Tx coil on top of the rat's leg, the capacitors are tuned for impedance matching and resonance. The system was turned "ON" and "OFF" at frequencies of 1 Hz and 5 Hz. An RF signal generator (SMBV100A, Rohde & Schwarz) connected to the power amplifier supplied 36 dBm of power to the Tx coil at 1.18 GHz. In order to control the duty cycle using pulse modulation, a 100 MHz arbitrary function generator (AFG3102, Tektronix) was connected to the RF generator. Monophasic current pulses with a width of 500 µs were delivered using the integrated 250 µm × 80 µm (0.02 mm^2) electrodes.

Fig. 4.22 shows a drawing of the experimental setup in order to clearly illustrate the different instruments and components used during the *in-vivo* testing. A formable RG405 SMP Female to SMA Male Cable was used so that the Tx coil remains impedance matched to the amplifier during the duration of the experiment. The fully implanted microbead is shown in Fig. 4.22(c). In order to better visualize the implant, it is shown again in Fig. 4.22(d), after placing it at very close proximity to the surface of the nerve.

4.8.2 Measurement Results

The 200 µm microbead was able to activate motor fibers to produce muscle twitches as shown in the EMG data (Fig. 4.21(c)). A video was recorded during the rat experiment and motion was extracted using the common Lucas-Kanade optical flow method to show the leg movement (Fig. 4.23).

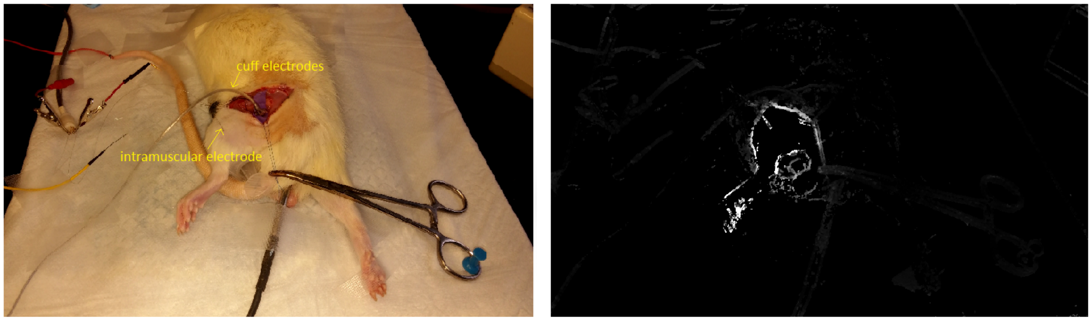

Figure 4.23: Picture of the anesthetized rat during stimulation. The picture on the right shows the leg twitching.

The EMG response to voltage-mode bipolar stimulation is shown in Fig. 4.24. Each voltage spike represents a muscle response; the width of the EMG response is about 5 ms, which explains why they appear as spikes in the 6 sec plot.

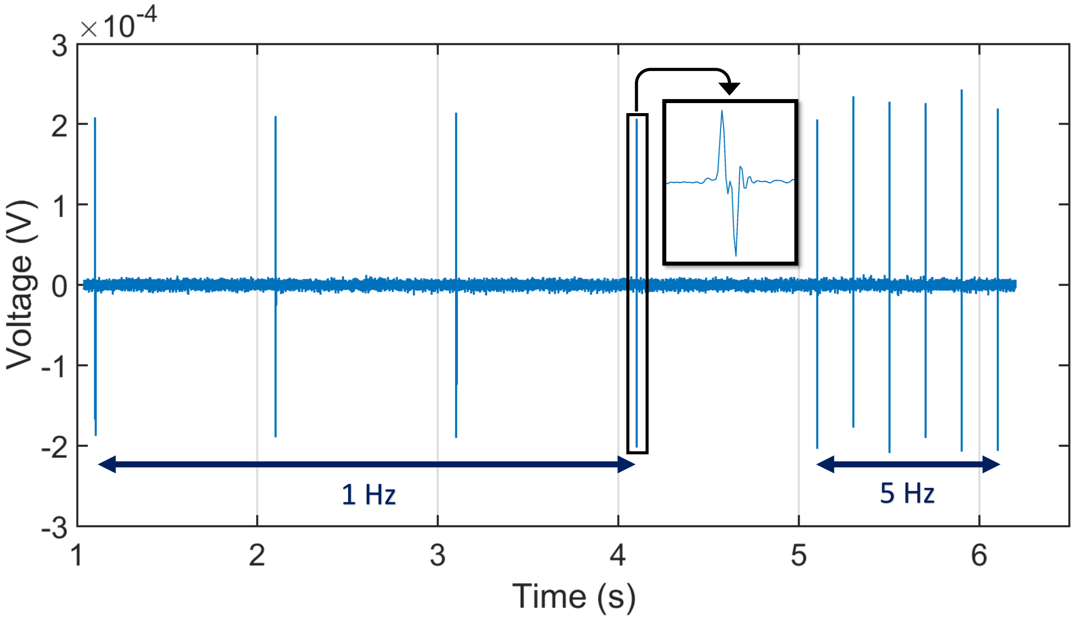

Figure 4.24: EMG response to voltage-mode bipolar stimulation at 1 Hz and 5 Hz repetition rate.

As the distance between the integrated electrodes is only 340 µm, recruiting a large number of nerve fibers in order to generate a large muscle force was not possible with the current amplitudes used. Furthermore, while the Tx coil was positioned such that the external coil center is aligned with the Rx coil center for maximal efficiency, this was difficult to verify, and a lateral displacement of up to 2 mm is possible which can result in a large attenuation in received power as shown in [37]. A rotational misalignment of at least 20 degrees is also expected.

4.9 Safety Limit Analysis

Although an experimental validation has been presented in a rat model, one of the applications of this work is to have the microbead implanted in human subjects as they would benefit to most from an untethered device. Therefore, it is important to know if the transmitted power level respects the limit for safe exposure to radio-frequency energy. To prevent tissue heating, the Federal Communications Commission (FCC) in the United States has set the specific absorption rate (SAR) limit to 1.6 W/kg, which is an average over a time period of 6 minutes for the head over any 1 g of tissue. SAR is given by the following equation:

$$SAR = \frac{\sigma |E|^2}{\rho}$$

where σ and ρ represent conductivity and mass density of the exposed tissue. E is the electric field strength in the tissue.

When continuously transmitting 36 dBm of power 1 mm above the human head, HFSS simulations shows a SAR value of 3.7 W/kg at the skin level. Fortunately, for neurostimulation applications, the duty cycle does not exceed 2% of the stimulation period. Since a pulsed powering scheme is implemented (like during magnetic resonance imaging scans), power is only transmitted for a very short amount of time. For instance, if we take the example of the *in-vivo* experiment when stimulating every second with a current pulse width of 195 µs, the power is transmitted for 200 µs every second and a total of 72 ms over 6 minutes. Therefore, the average SAR over 6 minutes is 0.74 mW/kg, which is well below the SAR limit. When stimulating at a repetition rate of 10 Hz with a current pulse width of 500 µs, the average SAR over 6 minutes becomes 18.5 mW/kg. In this work, the Tx-Rx distance has been limited to 1 cm due to the power amplifier (PA) maximum transmitting power capabilities. Therefore, knowing that there is a large headroom available before the SAR limit is reached, the microbead implantation depth can be significantly increased by simply utilizing a PA that delivers a larger output power.

4.10 Performance Summary and Comparison to the State-of-the-Art

Numerous wirelessly powered single channel neural stimulating implants have been fabricated [61, 62, 63, 64, 25, 29, 65, 27]. Table 4.2 summaries and compares the microbead performance with the smallest (< 50 mm^3) among them. The microbead is 50 times smaller than the second smallest neural stimulating implant reported in the comparison Table. The microbead extreme miniaturization puts a heavy limit on its implantation depth. Yet, owing to its optimized wireless inductive link, the FOM (Depth/Volume) remains large compared to the state-of-the-art. However, the FOM only provides a rough idea on the performance of the different types of implants as it can be further increased by increasing the transmitted power (and thus depth) until the SAR limit is reached. Therefore, it should not be solely relied upon for comparison. A voltage-mode stimulating microbead was used during the animal experiment, the current-mode stimulating microbead which uses biphasic stimulation was not tested *in-vivo*, and is thus not included in the table.

Table 4.2: Performance summary comparison with state-of-the-art ultra-small (< 50 mm^3) wirelessly powered neural stimulating implants.

Reference	[25]	[29]	[65]	[27]	**This work**
CMOS Process (nm)	180HV	65	-	discrete	**130RF**
Stimulation mode	current	current	switched-cap.	voltage	**voltage**
Wireless Link	ultrasound	ultrasound	2 coil inductive	2 coil inductive	**2 coil inductive**
Frequency (MHz)	1.3	1.85	394	10	**1180**
Charge Balance	biphasic	passive recharge	biphasic	none	**none**
Compliance Voltage (V)	15	3	N/A	N/A	**NA**
Electrode Material	Pt	PEDOT	Pt-Ir	Pt	**PEDOT/CNT**
Surface Area (mm^2)	3.3	0.3	0.79	0.07	**0.02**
Impedance (kΩ) at 1 kHz	< 1	4*	-	-	**8.2**
Animal model	(ex vivo) frog sciatic	rat sciatic	rat peroneal	rat sciatic	**rat sciatic**
Fully-implanted	no	yes	yes	yes	**yes**
In-vivo Depth (mm)	-	20	-	50	**5**
Off-chip components	capacitor, piezo, LED, and electrodes	capacitor, piezo, and electrodes	diodes, ind. and electrodes	no ASIC used	**none**
Implant Encapsulation	PDMS	parylene	SU-8	epoxy	**SiO_2**
Mass (mg)	78	10	-	-	**< 1**
Volume (mm^3)	39**	2.2	1.39	0.45	**0.009**
FOM$_{\text{Depth/Volume}}$ (mm^{-2})	-	9.1	-	111	**555**

** does not include the electrodes
* provided for 2.5 kHz

Chapter 5

Proof-of-concept: Sub-millimeter sized Neural Recording SoC

5.1 Electrical recording of the nervous system

The measurement of neural signals can be split in two categories: non-invasive and invasive. Some of the non-invasive neural recording methods include electroencephalography (EEG), magnetoencephalography (MEG), functional magnetic resonance imaging (fMRI) and positron emission tomography (PET). The invasive neural recording methods record the neuron activity directly from the cortex under the skull and thus can provide high spatial and time resolution. There are two ways to record action potentials: intracellularly recording and extracellularly recording. Extracellularly recordings are achieved by placing electrode adjacent to the neurons. An action potential amplitude ranges from 10 µV to 500 µV (this depends on the distance of the neuron form the electrode and the impedance of the electrode) with a bandwidth from 300 Hz to 7 kHz. Local field potentials are filtered in this work, and the focus is placed on AP as they are the primary signal of interest for neuroscientists and clinicians.

5.2 System overview

Before the development of the microbead concept, a larger neural recording system was developed and tested in-vivo [66]. The integrated circuits that have been implemented include neural amplifiers, digitizers, compressive sampling matrix and mixing, and inherently charge balanced neural stimulation methodologies. Compressive sampling was implemented on-chip to minimize the number of bits required to be communicated by the implant, while maximizing the reconstruction accuracy of the whole neural signal, not just the spikes. Neural data were acquired from the cortex of a monkey as shown in Fig. 5.1. The ASIC was not designed to be fully implanted and thus needed significant modifications in order to get it down to the microbead size scale (< 300 µm).

A detailed schematic of the recording microbead is shown in Fig. 5.2. The analog front-end includes a T-network amplifier, a SAR analog-to-digital converter (ADC), and an RC oscillator clock. The front-end was fabricated in GF 7RF 180 nm process, and measures 170 µm × 120 µm. Its ultra-small size is the result of many hours spent in layout design and layout miniaturization techniques (e.g. placing the transistors underneath the capacitors). Additionally, the system and circuit design also played a very important role in downsizing the front-end circuitry. The following sections provides the details on the innovative analog techniques implemented.

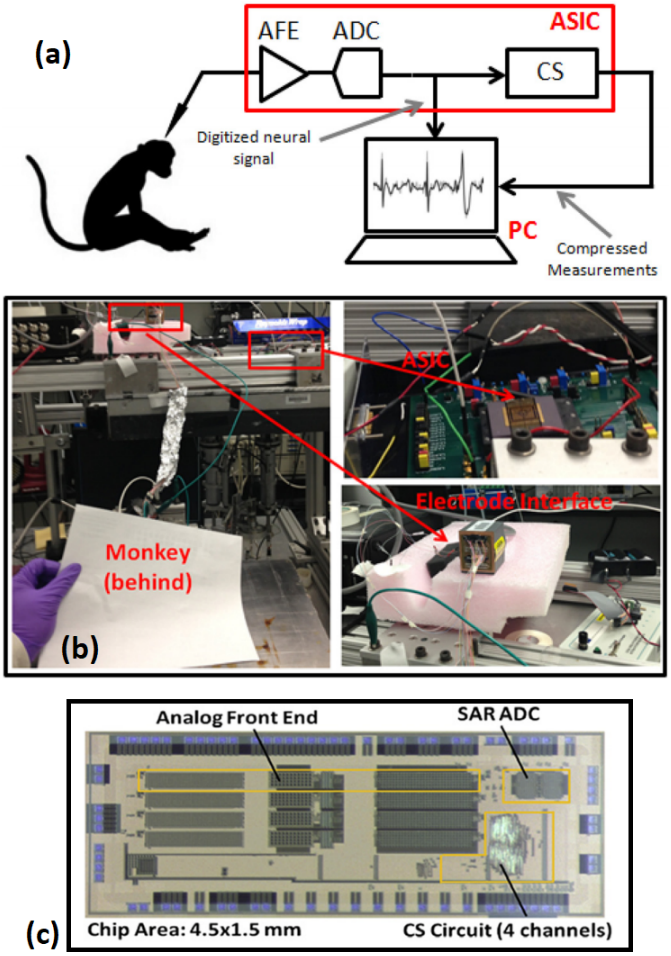

Figure 5.1: a) Drawing of the in vivo recording experiment setup. b) Picture of the setup. c) Micrograph of the ASIC.

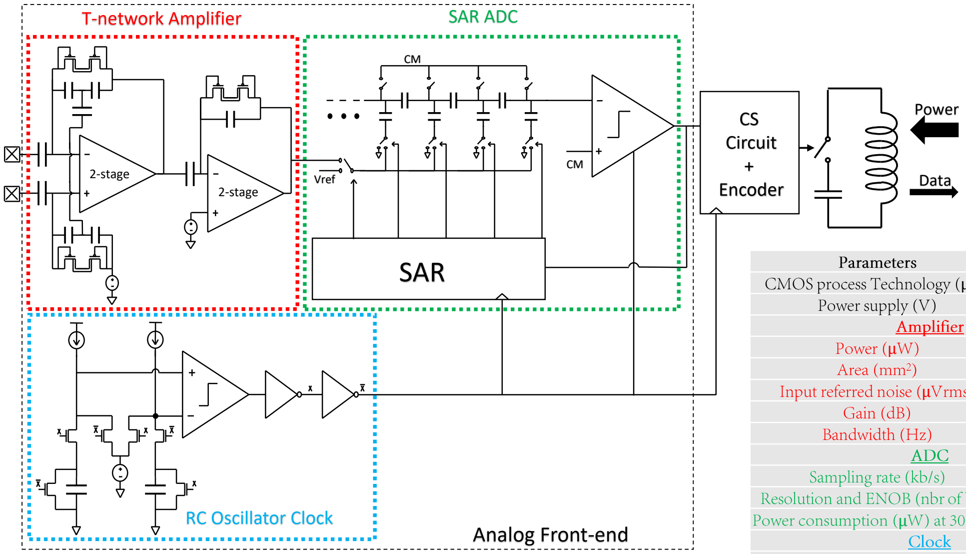

Parameters	Values
CMOS process Technology (µm)	0.18
Power supply (V)	1.8
Amplifier	
Power (µW)	2.3
Area (mm²)	0.009
Input referred noise (µVrms)	6.47
Gain (dB)	62.3
Bandwidth (Hz)	278 – 7.7k
ADC	
Sampling rate (kb/s)	25
Resolution and ENOB (nbr of bits)	8 / 6.6
Power consumption (µW) at 300kHz	24
Clock	
Power consumption (µW) at 300kHz	3.7

Figure 5.2: Detailed schematic of the recording microbead with a table summarizing its performance.

5.3 Amplifier

The differential amplifier is composed of two op-amps. Each op-amps includes a 2-stage miller operational transconductance amplifier (OTA) with a common source (Fig. 5.3). The OTA shows a simulated open-loop gain of 50 dB and an open-loop phase of 62 degrees. The input transistors are biased in sub-threshold region to minimize power consumption and improve noise performance. Large area PMOS transistors are used as input transistors to minimize the 1/f noise and large lengths are used for the current mirror transistors to improve current mirror matching. Matching is also improved during layout design by dividing the matching transistors into figured structures and placed in a common-centroid configuration.

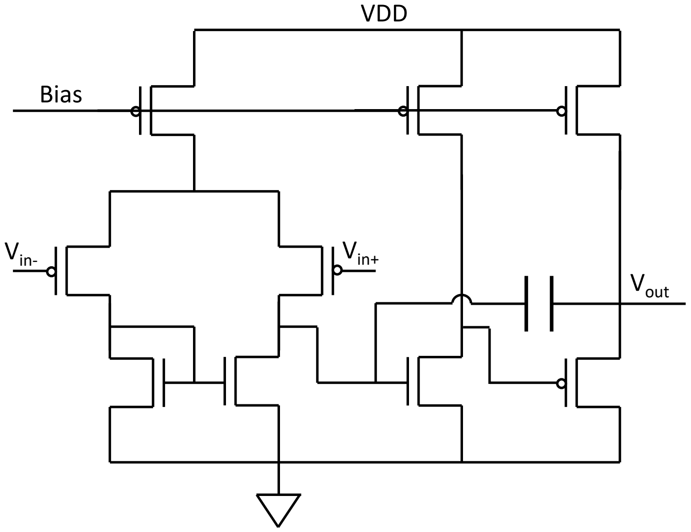

Figure 5.3: Schematic of the 2-stage miller OTA.

The amplifier is capacitively-coupled in order to eliminate the DC offset voltage coming from the electrode-electrolyte interface. The DC voltage is large enough to saturate the amplifier and is thus not wanted. Unfortunately, AC-coupled amplifier with large closed-loop gains require two large input series capacitors which would increase the size of the implant and would decrease the input impedance of the amplifier (leading to a large signal attenuation coming from the electrodes). Therefore, to keep the area small, a T-network based capacitive feedback is implemented for the first-stage (Fig. 5.4). Its derivation can be found in [67]. The mid-band gain of the first op-amp is calculated as: $(\frac{C_{iu}}{C_{F1}})(\frac{C_{F1}+C_{F2}+2C_{F12}}{C_{F12}})$. The gain of the second op-amp is given by: $\frac{C_{in-2}}{C_{F-2}}$. The T-network implementation has reduced the area of the amplifier by at least 7 times compared to a conventional capacitive feedback topology. Further reduction is possible but decreasing the input capacitors value would make them too sensitive to process variations and would increase the input referred noise of the amplifier which is set to 6.57 µVrms (much smaller than the noise coming from neural background activity and the thermal noise of the electrodes). To keep the total input-referred noise to a reasonable level, the amplifier is designed to have a high closed-loop gain (62.3 dB) in order to compensate for the ADC's small effective number of bits (ENOB). It is well known that the first amplifier plays an important role in setting the noise performance of the system as the input-referred noise of subsequent blocks are reduce by the gain of the preceding stages.

To save area, all the needed filtering happens at the first amplification stage such that the need of an additional filtering stage is eliminated. The bandpass amplifier is designed to capture only action potentials and thus has a bandwidth of 278 Hz to 7.7 kHz. The lower cut off frequency is set by the feedback resistance and capacitance. To reduce area, the high-value feedback resistors are implemented using MOS pseudo-resistors. The upper cut off frequency is mainly set by the transconductance of the OTA (which explains why the OTA's open-loop gain does not have a larger value). The amplifier has a total area of 0.009 mm^2, making it one of the smallest neural amplifiers to date (even with compared to smaller process nodes).

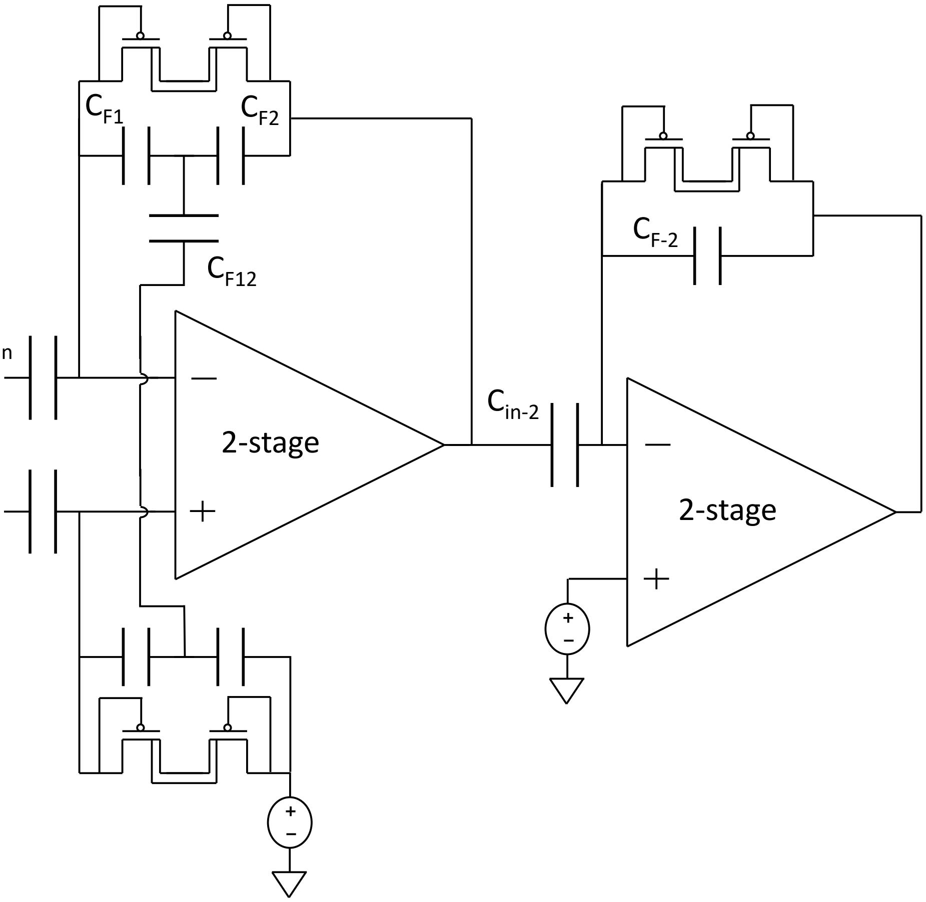

Figure 5.4: Schematic of the T-network AC-coupled amplifier.

5.4 ADC

The goal of an ADC is to quantize an input V_{in} to one of the various levels in its full-scale range. These levels are equidistant from each other with difference equal to the resolution of the ADC. The ADC adds error to the output due to this quantization process which is known as quantization error. The digital-to-analog converter (DAC) is controlled by the

SAR logic based on the previous decision. Each output of the comparator is stored in a data register. Various kind of DACs can be used in a SAR ADC but capacitive DAC are predominantly employed due to the advantage of no static power dissipation.

The successive approximation register (SAR) ADC architecture is chosen in this work (Fig. 5.5). It's a good fit for single channel neural signal acquisition systems because of its low-power consumption and its medium speed. The full-scale reference voltage of the 8-bit ADC is Vref = 1.4 V, giving a quantization noise of 1.49 mVrms (or 1.22 μVrms when referred to the input of the amplifier). To reduce power consumption and area, a combination of split-capacitor array and C-2C ladder is utilized for the DAC. To improve capacitor matching, unit capacitors are used to implement the array. The SNRD defines the minimum capacitor size. The comparator is composed of a pre-amplifier and a latch as shown in Fig. 5.6. The pre-amplifier amplifies the input difference and reduces the kickback effect coming from the positive feedback stage of the latch.

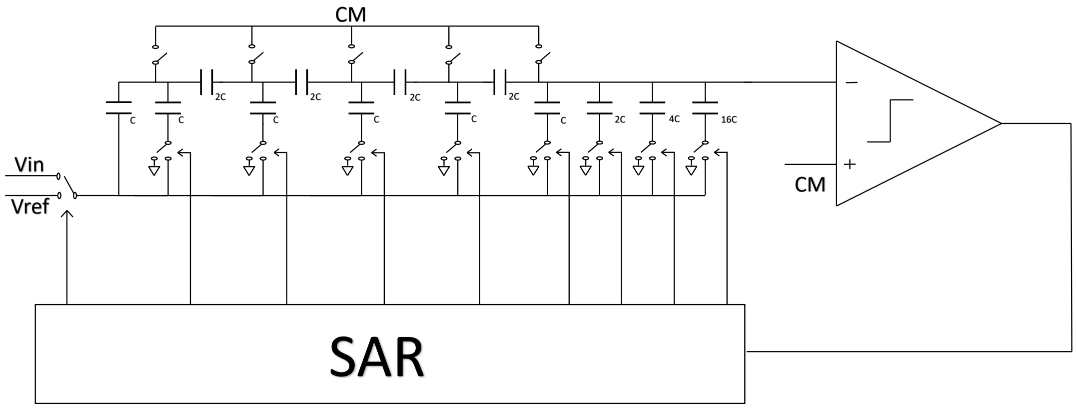

Figure 5.5: Schematic of the SAR ADC.

For a real ADC, the effective number of bits (ENOB) is are more realistic measure to specify the ADC's resolution, compared to the number of bits (N) which does not summarize an ADC's dynamic performance. The ENOB takes the signal-to-noise-and-distortion ratio SNDR into consideration as follows:

$$ENOB = \frac{SNDR - 1.76}{6.02}$$

The simulated ENOB for the compact ADC is 6.6 bits. The sampling frequency of the ADC is set to 25 kHz, which is slightly higher than the Nyquist frequency. This requires a clock frequency of 300 kHz (25 kHz*12 cycles) because 3 cycles are used for sampling, 8 for bit cycling and 1 for storing.

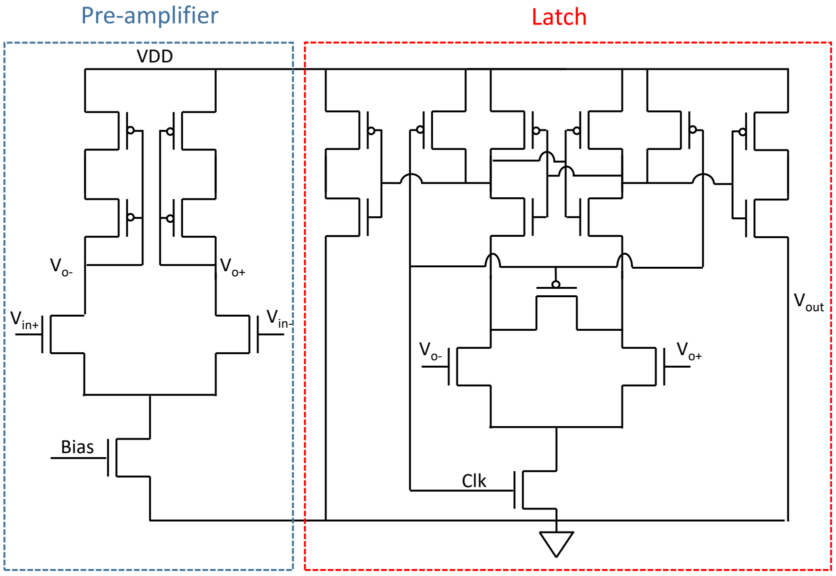

Figure 5.6: Schematic of the comparator used in the ADC.

5.5 Clock

The clock is a type of RC oscillator (Fig. 5.7). It has the advantage of being very accurate, low power, and resistant to bias variations. When the voltage at node X is low, a current passes through one of the two capacitors, charging it such that node V_- ramps up at a rate dependent the capacitor value. Meanwhile, node V_+ is set to V_{ref}. When node V_- crosses V_+, the comparator goes low which toggles all the switches. When node X is high, the voltages at the capacitor resets and the reverse occurs. Therefore, the clock frequency is set by the values of the capacitors, the current source and the reference voltage. At 300 kHz the RC oscillator consumes a total of 3.72 μW (from a 1.8 V supply) and measures 1750 um^2.

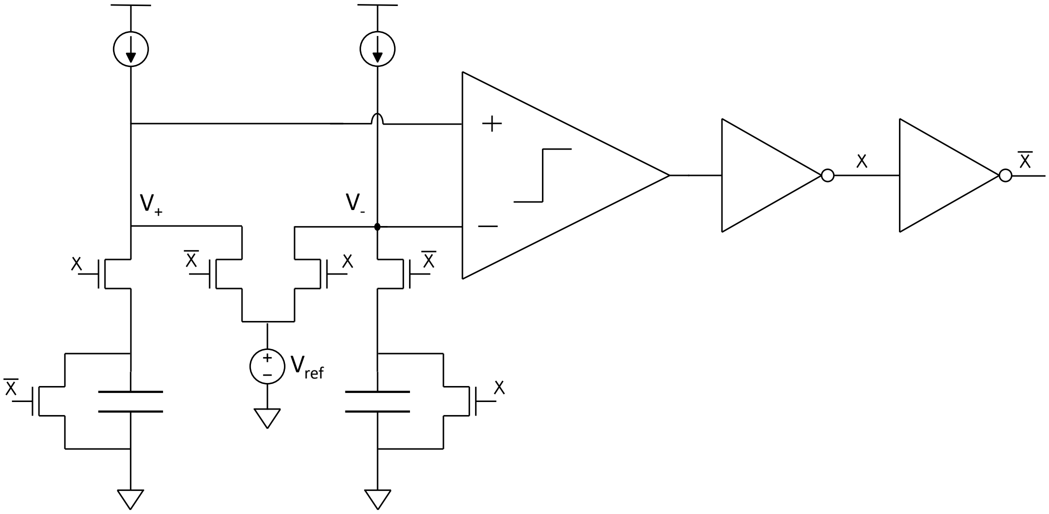

Figure 5.7: Schematic of the RC oscillator clock.

5.6 Safety Limit Analysis

When continuously transmitting 36 dBm of power 1 mm above the human head, HFSS simulations shows a SAR value of 3.7 W/kg at the skin level. This means that when recording every second for 400 ms, the average SAR over 6 minutes becomes 1.48 mW/kg, which is below the SAR limit. However, it is important to note that a high peak pulsed power transmission scheme is practical for stimulating IMDs but not so much for recording IMDs since neuroscientist and clinicians generally want to record neural activity within the entire time frame of an experiment without any interruptions. Thus, how can the SAR be reduced when continuously sending power to an ultra-small implant?

SAR is proportional to the square of the magnitude of the electric field. Reducing the electric field is generally done by dividing the Tx coil into multiple segments using capacitors. As a result, a more uniform current distribution within the loop is obtained and the hotspots close to the feed point of the coil diminishes [68]. However, the Tx coil perimeter (i.e., 4 cm) is much smaller than the RF wavelength, and therefore segmenting the coil did not show any significant improvements. Another approach has been taken as shown the following section.

5.7 Coil Array Design for Maximizing Wireless Power Transfer

To focus energy on a particular point in space, be it electromagnetic or ultrasonic energy, a phase array of transmitters can be used. Prior work has presented systems relying on multiple transmit coils to improve power delivery [69, 70, 71], but none of these simulations were done in the context of safety limits for implantable devices.

5.7.1 Tx Coil Array Design

In this section, an optimization strategy is presented for the design of a coil array for near-field beamforming.

The additional Tx coils increase the power induced at the terminals of the Rx coil. To maximize this power, the contribution of each Tx coil to the open-circuit voltage at the terminals of Rx coil has to be aligned in time. This is achieved by introducing the phase difference between the currents driving the Tx coils. The mutual coupling between Tx coils reduces the power efficiency of the system and increases the electrical field, effectively reducing the maximum allowable current given to each of Tx coils. The increase of the induced voltage in Rx coil, as well as the mutual coupling and the maximum current that satisfies SAR limit, depends on the distance between the Tx coils. The system with $n - 1$ Tx coils can be modeled as n-port network with the network parameters extracted using a full wave EM solver. With the extracted Z-parameters, the network comprising of n – 1 Tx coils and a single Rx coil can be modeled as:

$$\begin{bmatrix} V_1 \\ V_2 \\ . \\ . \\ V_{n-1} \\ 0 \end{bmatrix} = \begin{bmatrix} Z_{11} & Z_{12} & . \; . & Z_{1n} \\ Z_{21} & Z_{22} & . \; . & Z_{2n} \\ . & . & . \; . & . \\ . & . & . \; . & . \\ Z_{(n-1)1} & Z_{(n-1)2} & . \; . & Z_{(n-1)n} \\ Z_{n1} & Z_{n2} & . \; . & Z_{nn} + Z_L \end{bmatrix}$$

where V_i and I_i (i = 1,2,..,n) are voltages and currents of the coils in the system, respectively. In the case of weakly coupled Tx coils and Rx coil, we can neglect the effect of Rx coil on the circuit of each of the Tx coils and equate each of the impedances Z_{in}, (i = 1, 2, .., n-1) with 0. This also means that the optimal load in the Rx coil circuit becomes just the conjugate of impedance Z_{nn}. This leads to a simple expression for the power delivered to the implant:

$$P_{imp} = \frac{1}{8} Re(Z_{nn}) |I_n|^2 \tag{5.2}$$

The input power can be computed as:

$$P_{in} = \frac{1}{2} \sum_{i=1}^{n-1} Re(V_i I_i^*) \tag{5.3}$$

The maximum power that can be delivered to the implant is determined by the maximum current of the Tx coils that satisfies SAR limit.

5.7.2 Simulation Setup

All simulations were done using the 3D EM simulator ANSYS HFSS. To mimic the brain implantation scenario in our simulations, we chose a model of an average sized human head represented by different lossy materials that have a frequency-dependent complex relative permittivity and conductivity which are suitable for high frequency simulations. As illustrated in Fig. 5.8, the six-layered human head model includes skin, fat, skull, dura, cerebrospinal fluid (CSF), and grey matter (GM). We assume that the on-chip coil is implanted 1 mm into the GM of the brain, while the transmitting coil(s), fabricated on printed circuit board (PCB), are 1 mm away from the skin. The total distance between transmitting coil(s) and receiving coil is then 12 mm. In the following section, we will investigate the simulation results for five transmitting coil(s).

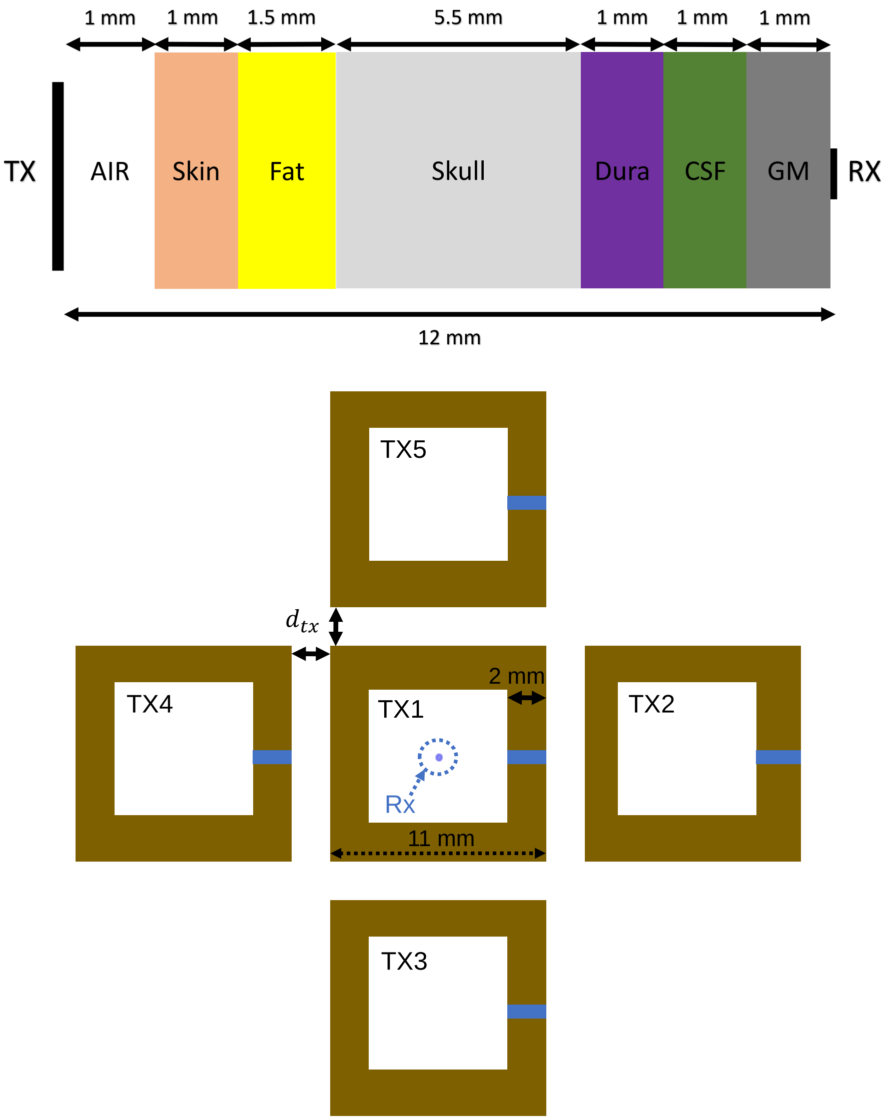

Figure 5.8: (Top) A drawing of the six-layer human head model used. (Bottom) Top view of 5 Tx coils on top of the small Rx coil.

5.7.3 Simulation Results

Adding more coils to the array results in higher available power for the on-chip coil. To show this, four more Tx coils were added at each side of the center coil in a cross shape array manner as illustrated in Fig. 5.8. The current phase difference between the off center coils and the center coil is kept same in all the simulations. I_{max} that satisfies the SAR limit for different distances as a function of the current phase shift is shown in Fig. 5.9, while the maximum power that can be delivered to the implant is shown in Fig. 5.10. The maximum power that can be delivered to the implant occurs at a distance of 2 mm, with a current phase shift of 60^o, and at a distance of 7 mm, with a current phase shift of 150^o, between the coils. The maximum power is 10.6 μW leading to the overall gain of the antenna array of 4.3 dB.

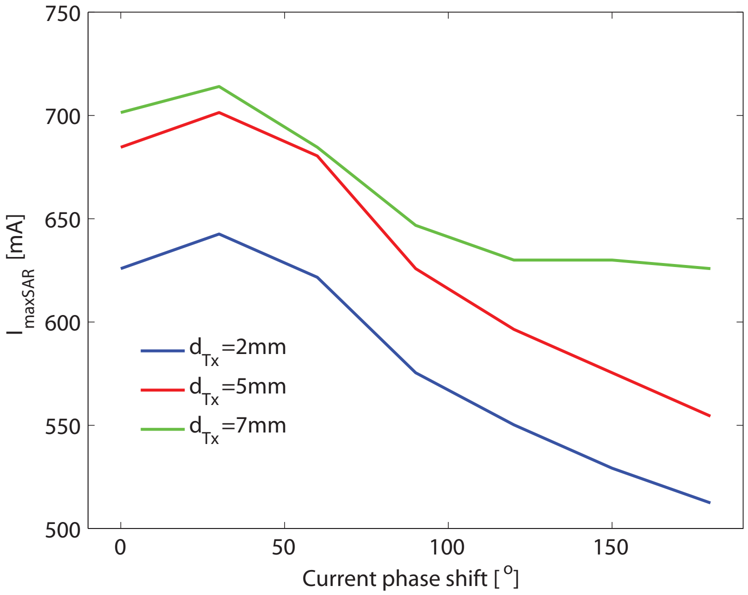

Figure 5.9: The maximum input current (that meets the SAR limit) of Tx coils as a function of phase difference in coils' current for different distances between the coils in case of 5 coil transmitter array.

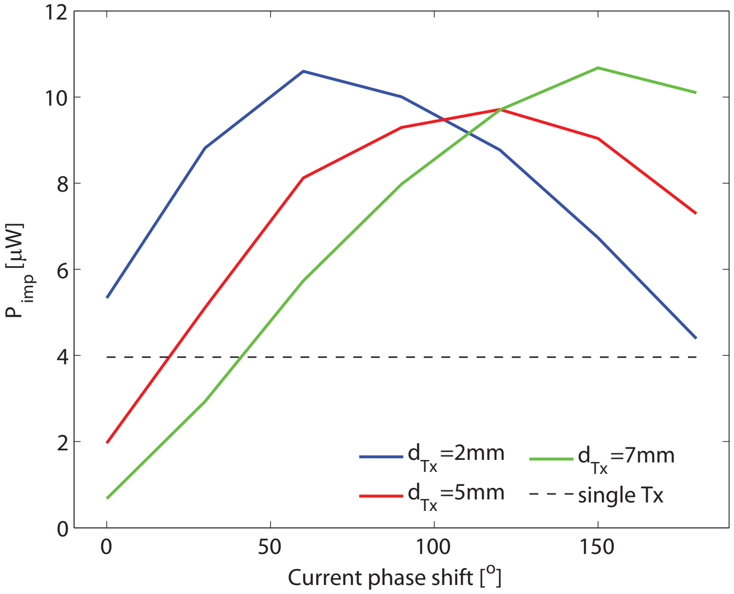

Figure 5.10: The maximum power that can be delivered to implant as a function of phase difference in coils' current for different distances between the coils in case of 5 coil transmitter array.

5.7.4 Discussion

The distance between transmitters (d_{tx}) and the current phase assigned to each Tx were optimized to maximize the Rx gain. Next, the power provided to the transmitters of both setups (single coil and coil array) was increased until the SAR limit was reached. Simulation results show that an improvement of 4.3 dB in gain was achieved with the phased array compared to the single coil. Furthermore, since the phased array allows the energy beam to be steered to a localized area, the coil array also performs better when the microbead is misaligned, for instance, for a directional misalignment of 3 mm from the center (along X or Y-directions), an improvement of 4 dB in gain was obtained. Although this increase in gain might not be sufficient in some applications, it is important to remember that adding more coils to the array will improve the gain even further. The phased array implemention is not covered in this work and will be fabricated on a flexible PCB to reduce the distance between the edge coils and the microbeads.

Chapter 6

Conclusions and Future Directions

6.1 Conclusions

A new generation of neural interface is needed to open up a wide range of potential applications that are currently not possible. In this thesis, the development of an ultra-small (~ 0.009 mm^3) neural implant device and its experimental validation has been reported. To allow for minimally-invasive insertion into the cortex and subcortex, the microbead has been extensively miniaturized by minimizing the area of the system using simplification and aggressive layout design techniques, and by implementing a novel packaging method to allow the microbead to become a fully encapsulated stand-alone implant. In order to increase the implantation depth of the SoC, the power consumption has been minimized by improving the PCE and the inductive link has been strengthened owing to the innovative optimization design flow of the Tx and Rx coils. The microbead has been fully implanted in a sciatic nerve to elicit compound action potentials. The purpose validating the implant in PNS is to show applicability to CNS applications.

The microbead has the potential to replace the Utah array as the main interface used for chronic MEA recordings and stimulations, particularly in studies involving many neurons from many areas distributed around the nervous system. The presented work is to be seen as the initial steps taken in achieving the goal of safely powering ultra-small implants. Although there are still numerous obstacles to overcome, the future of fully injectable single channel neural interfaces looks promising. The next iteration of this work is discussed in the following sections.

6.2 Future Directions

6.2.1 Microbead fabrication using SOI technology and Closed-loop stimulation

Closed-loop stimulation offers tremendous advantages for human patients such as ongoing therapy adjustment and disease control [72, 73]. In order to allow the microbead to be efficiently used as a tool for closed-loop neuromodulation, it has to include both the recording and stimulating channel on a single silicon die. In order to keep the microbead within the 300 µm size limit, a smaller process node ($\leq$ 65nm) has to be chosen. Fig. 6.1 presents the entire system architecture of the proposed microbead. The power harvesting system with the current driver (which we call the stimulating microbead), the analog front end (which we call the recording channel), the compressive sampling (CS) circuit and backscattering circuitry, will all be included into a single chip.

Furthermore, the generation of microbeads will be fabricated using silicon-on-insulator (SOI) technology which will bring the following advantages:

- Higher power transfer efficiency (due to an increase in the on-chip coil quality factor)
- High power conversion efficiency (due to a decrease in parasitic losses)
- Fully encapsulated microbead in SiO_2

Migrating the current design to SOI technology (6.2) offers significant advantages in terms of packaging. Below shows a process flow that will eliminate the current leakages that are decreasing the stimulation capabilities of the currently fabricated prototype.

The first step is to fabricate the CMOS chip using a SOI wafer. After receiving the dies from the foundry (Fig. 6.3(a)), dicing the 1.5 mm × 1.5 mm chip into a 302 μm × 302 μm microbead exposes the top metal on all four sides of the die to act as stimulation electrodes and recording electrodes (Fig. 6.3(b)). In order to better understand the process flow, the figure only displays 2 out of the 4 electrodes. Au (Fig. 6.3(c)) and Poly-ink (Fig. 6.3(d)) are deposited on all 4 electrodes as described in Chapter 4. The SOI microbead is then thinned down to 20 μm (this number might change depending on the process node used)

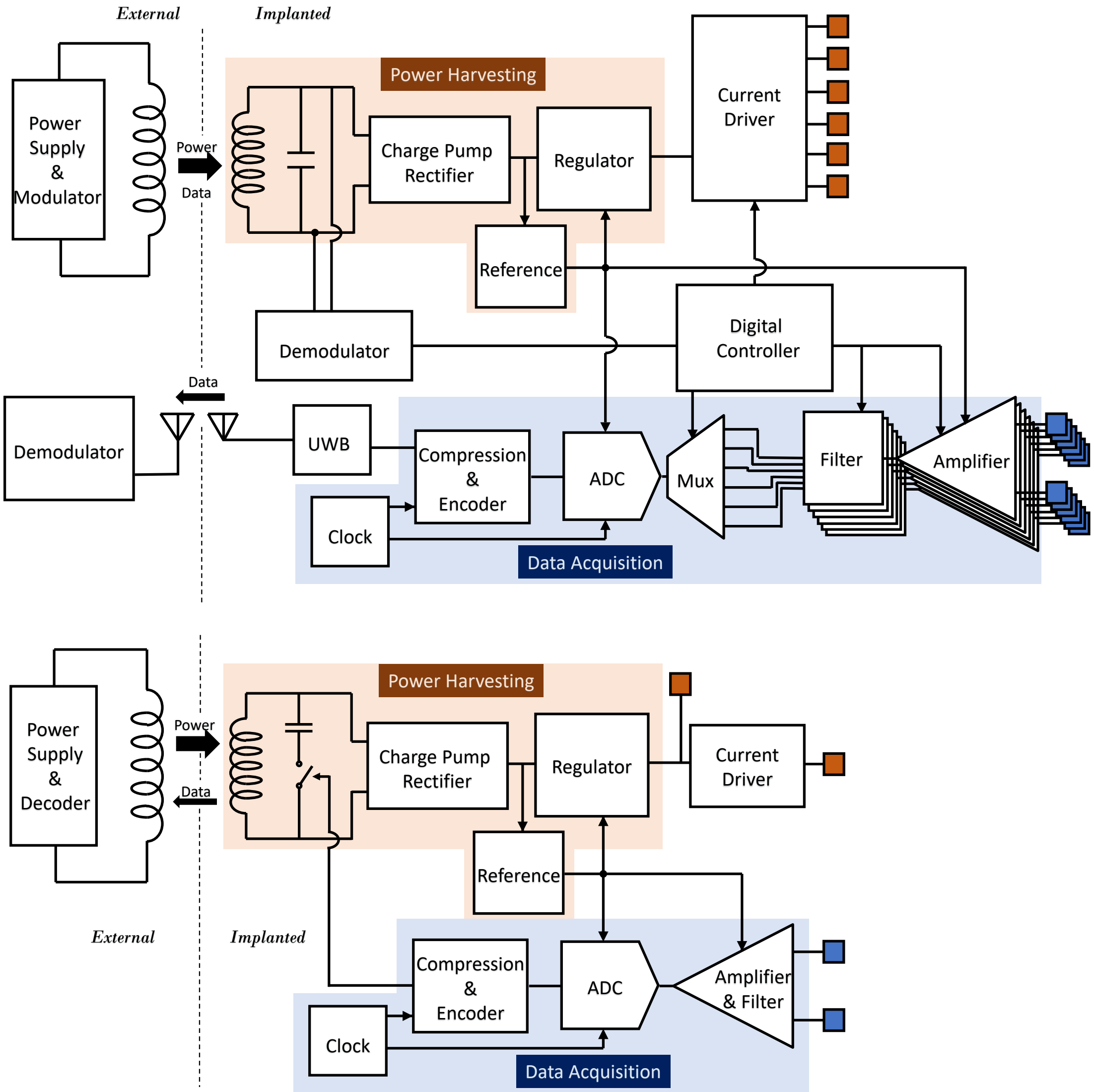

Figure 6.1: Drawing of the system architecture of the proposed recording/stimulating microbead.

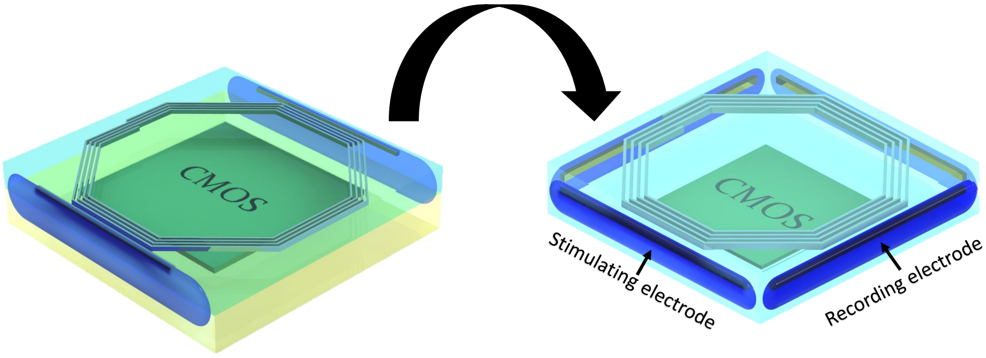

Figure 6.2: 3D drawing of the (left) fabricated stimulating microbead and the stimulating/recording microbead in SOI.

using a polishing system before completely removing the silicon substrate by wet-etching using tetramethylammonium hydroxide (TMAH) while using the buried oxide layer as an etch stop. TMAH has good selectivity, is non-toxic and is CMOS compatible as it has no mobile K+ contamination (unlike KOH). However, the downside is that TMAH etches aluminum which could happen at this stage of the process if parts of the Al electrode remains exposed after Au and Poly-ink deposition. A solution proposed in [74] is to dissolve an appropriate amount of silicon in TMAH. The silicon powder forms aluminosilicates on Al which serves as a passivation layer. With the carrier substrate removed (Fig. 6.3(e)), the remaining system is completely encapsulated in silicon dioxide, which has a low water vapor permeability. The final dimensions of the microbead are 302 µm × 302 µm × 20 µm, giving it a volume of 0.0018 mm^3. Although the proposed packaging concept significantly reduces current leakage, it is still intended for acute experiments as a stand-alone SiO_2 will slowly dissolve when exposed to body fluids [75].

Parts of the system shown in Fig. 6.1 have already been successfully implemented using the described process flow on a 32nm SOI wafer.

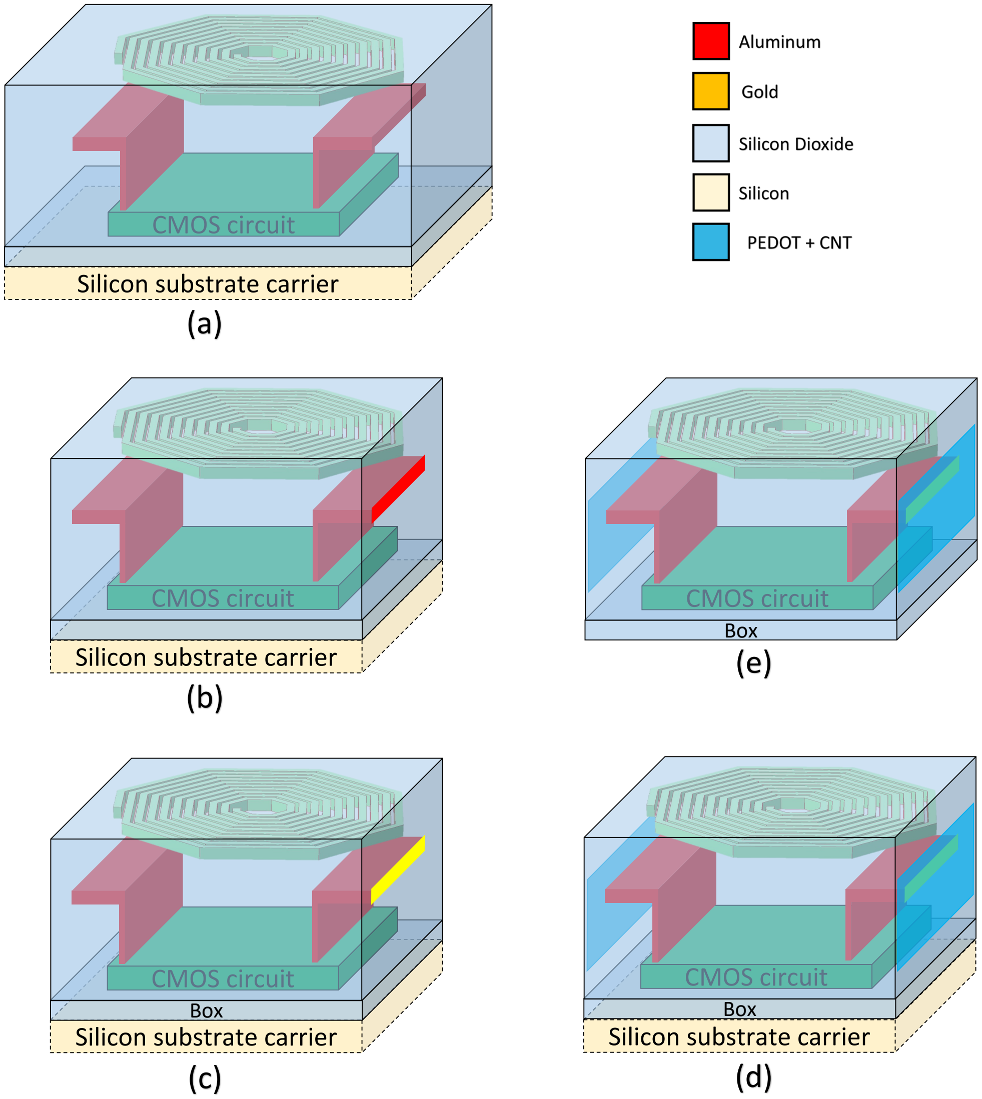

Figure 6.3: Process flow diagram of the proposed microbead in SOI technology.

6.2.2 Implementation of a backscattering system

Telemetry can be implemented using backscattering technology which allows the use of a single inductive link for both power and data. This method modulates the load seen by the Rx coil. Since only a switch needs to be driven, the power consumption is very small compared to other telemetry techniques that require a power amplifier. The downside is the complexity at the external data reception because of the large power difference between the weak backscattered signal and the forward power signal carrier. To verify the possibility of wirelessly transmitting neural recorded data to the external coil using backscattering technology, the entire setup was simulated in Advanced Design System (ADS) as shown in Fig. 6.4. The S-parameters were derived from HFSS when the external coil was placed 5 mm from the microbead. Based on the simulations results, the reflected data is strong enough to be captured when transmitting 35 dBm of power. The next step is to replicate this setup with real components.

The proposed circuitry to transmit and read the backscattered signal is shown in Fig. 6.5. The neural data stream is converted into a manchester encoded signal which is used to control a switch in series with the resonating capacitor. Binary phase shift keying (BPSK) modulation is thus used to toggle between 2 states (resonance and open load) thereby modulating the reflected RF wave to establish a wireless communication.

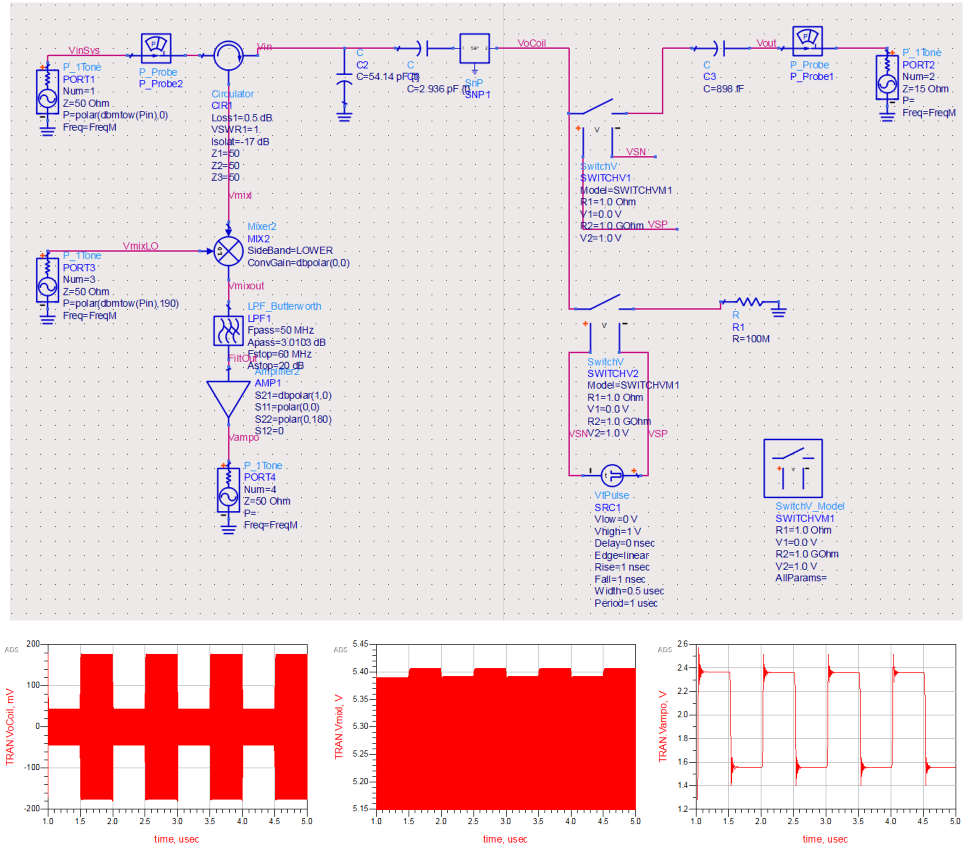

Figure 6.4: (Top) Backscattering system simulation setup. (Bottom) Simulated output waveforms of the backscattered signal before the mixer and after the amplifier.

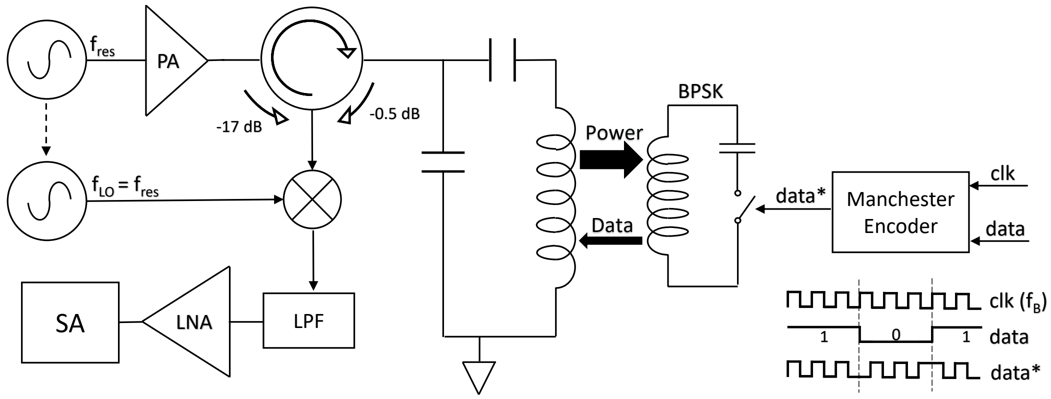

Figure 6.5: Proposed system architecture to transmit and read the backscattered neural data.

Bibliography

[1] A. L. Benabid, P. Pollak, D. Hoffmann, C. Gervason, M. Hommel, J. E. Perret, J. De Rougemont, and D. M. Gao, "Long-term suppression of tremor by chronic stimulation of the ventral intermediate thalamic nucleus," *The Lancet*, vol. 337, no. 8738, pp. 403–406, 1991.

[2] R. P. Michelson, "Electrical stimulation of the human cochlea: a preliminary report," *Archives of Otolaryngology*, vol. 93, no. 3, pp. 317–323, 1971.

[3] S. Nag and N. V. Thakor, "Implantable neurotechnologies: electrical stimulation and applications," *Medical & biological engineering & computing*, vol. 54, no. 1, pp. 63–76, 2016.

[4] A. M. Sodagar, G. E. Perlin, Y. Yao, K. Najafi, and K. D. Wise, "An implantable 64-channel wireless microsystem for single-unit neural recording," *IEEE Journal of Solid-State Circuits*, vol. 44, no. 9, pp. 2591–2604, 2009.

[5] X. Xie, L. Rieth, L. Williams, S. Negi, R. Bhandari, R. Caldwell, R. Sharma, P. Tathireddy, and F. Solzbacher, “Long-term reliability of al2o3 and parylene c bilayer encapsulated utah electrode array based neural interfaces for chronic implantation,” *Journal of neural engineering*, vol. 11, no. 2, p. 026016, 2014.

[6] S. Ha, A. Akinin, J. Park, C. Kim, H. Wang, C. Maier, G. Cauwenberghs, and P. P. Mercier, “A 16-channel wireless neural interfacing soc with rf-powered energy-replenishing adiabatic stimulation,” *VLSI Circuits*, p. C107, 2015.

[7] P. Troyk, S. Bredeson, S. Cogan, M. Romero-Ortega, S. Suh, Z. Hu, A. Kanneganti, R. Granja-Vazquez, J. Seifert, and M. Bak, “In-vivo tests of a 16-channel implantable wireless neural stimulator,” in *2015 7th International IEEE/EMBS Conference on Neural Engineering (NER)*. IEEE, 2015, pp. 474–477.

[8] L. Karumbaiah, T. Saxena, D. Carlson, K. Patil, R. Patkar, E. A. Gaupp, M. Betancur, G. B. Stanley, L. Carin, and R. V. Bellamkonda, “Relationship between intracortical electrode design and chronic recording function,” *Biomaterials*, vol. 34, no. 33, pp. 8061–8074, 2013.

[9] V. S. Polikov, P. A. Tresco, and W. M. Reichert, “Response of brain tissue to chronically implanted neural electrodes,” *Journal of neuroscience methods*, vol. 148, no. 1, pp. 1–18, 2005.

[10] R. Chen, A. Canales, and P. Anikeeva, “Neural recording and modulation technologies,” *Nature Reviews Materials*, vol. 2, no. 2, p. 16093, 2017.

[11] I. Dvorak and A. V. Holden, *Mathematical approaches to brain functioning diagnostics*. Manchester University Press, 1991.

[12] W. M. Grill, S. E. Norman, and R. V. Bellamkonda, “Implanted neural interfaces: biochallenges and engineered solutions,” *Annual review of biomedical engineering*, vol. 11, pp. 1–24, 2009.

[13] A. Campbell and C. Wu, “Chronically implanted intracranial electrodes: Tissue reaction and electrical changes,” *Micromachines*, vol. 9, no. 9, p. 430, 2018.

[14] D. A. Schwarz, M. A. Lebedev, T. L. Hanson, D. F. Dimitrov, G. Lehew, J. Meloy, S. Rajangam, V. Subramanian, P. J. Ifft, and Z. Li, “Chronic, wireless recordings of large-scale brain activity in freely moving rhesus monkeys,” *Nature methods*, vol. 11, no. 6, pp. 670–676, 2014.

[15] D. A. Borton, M. Yin, J. Aceros, and A. Nurmikko, “An implantable wireless neural interface for recording cortical circuit dynamics in moving primates,” *Journal of neural engineering*, vol. 10, no. 2, p. 026010, 2013.

[16] S. L. Bressler and V. Menon, “Large-scale brain networks in cognition: emerging methods and principles,” *Trends in cognitive sciences*, vol. 14, no. 6, pp. 277–290, 2010.

[17] A. P. Alivisatos, M. Chun, G. M. Church, R. J. Greenspan, M. L. Roukes, and R. Yuste, “The brain activity map project and the challenge of functional connectomics,” *Neuron*, vol. 74, no. 6, pp. 970–974, 2012.

[18] R. Eckhorn, H. J. Reitboeck, M. Arndt, and P. Dicke, “Feature linking via synchronization among distributed assemblies: Simulations of results from cat visual cortex,” *Neural computation*, vol. 2, no. 3, pp. 293–307, 1990.

[19] W. W. Seeley, R. K. Crawford, J. Zhou, B. L. Miller, and M. D. Greicius, “Neurodegenerative diseases target large-scale human brain networks,” *Neuron*, vol. 62, no. 1, pp. 42–52, 2009.

[20] G. A. Tabot, J. F. Dammann, J. A. Berg, F. V. Tenore, J. L. Boback, R. J. Vogelstein, and S. J. Bensmaia, “Restoring the sense of touch with a prosthetic hand through a brain interface,” *Proceedings of the National Academy of Sciences*, vol. 110, pp. 18 279–18 284, 2013.

[21] D. Seo, J. M. Carmena, J. M. Rabaey, M. M. Maharbiz, and E. Alon, “Model validation of untethered, ultrasonic neural dust motes for cortical recording,” *Journal of neuroscience methods*, vol. 244, pp. 114–122, 2015.

[22] J. S. Ho, A. J. Yeh, E. Neofytou, S. Kim, Y. Tanabe, B. Patlolla, R. E. Beygui, and A. S. Poon, “Wireless power transfer to deep-tissue microimplants,” *Proceedings of the National Academy of Sciences*, vol. 111, pp. 7974–7979, 2014.

[23] P. Yeon, S. A. Mirbozorgi, B. Ash, H. Eckhardt, and M. Ghovanloo, “Fabrication and microassembly of a mm-sized floating probe for a distributed wireless neural interface,” *Micromachines*, vol. 7, no. 9, p. 154, 2016.

[24] M. Mark, Y. Chen, C. Sutardja, C. Tang, S. Gowda, M. Wagner, D. Werthimer, and J. Rabaey, “A 1mm 3 2mbps 330fj/b transponder for implanted neural sensors,” pp. 168–169, 2011.

[25] J. Charthad, T. C. Chang, Z. Liu, A. Sawaby, M. J. Weber, S. Baker, F. Gore, S. A. Felt, and A. Arbabian, “A mm-sized wireless implantable device for electrical stimulation of peripheral nerves,” *IEEE transactions on biomedical circuits and systems*, vol. 12, no. 2, pp. 257–270, 2018.

[26] S. Lee, A. J. Cortese, A. P. Gandhi, E. R. Agger, P. L. McEuen, and A. C. Molnar, “A 250μm $\times$ 57μm microscale opto-electronically transduced electrodes (motes) for neural recording,” *IEEE transactions on biomedical circuits and systems*, vol. 12, no. 6, pp. 1256–1266, 2018.

[27] D. K. Freeman, J. M. O’Brien, P. Kumar, B. Daniels, R. A. Irion, L. Shraytah, B. K. Ingersoll, A. P. Magyar, A. Czarnecki, and J. Wheeler, “A sub-millimeter, inductively powered neural stimulator,” *Frontiers in neuroscience*, vol. 11, p. 659, 2017.

[28] D. Seo, R. M. Neely, K. Shen, U. Singhal, E. Alon, J. M. Rabaey, J. M. Carmena, and M. M. Maharbiz, “Wireless recording in the peripheral nervous system with ultrasonic

neural dust," *Neuron*, vol. 91, no. 3, pp. 529–539, 2016.

[29] D. K. Piech, B. C. Johnson, K. Shen, M. M. Ghanbari, K. Y. Li, R. M. Neely, J. E. Kay, J. M. Carmena, M. M. Maharbiz, and R. Muller, "Stimdust: A 2.2 mm3, precision wireless neural stimulator with ultrasonic power and communication," *arXiv preprint arXiv:1807.07590*, 2018.

[30] P. Yeon, S. A. Mirbozorgi, J. Lim, and M. Ghovanloo, "Feasibility study on active back telemetry and power transmission through an inductive link for millimeter-sized biomedical implants," *IEEE transactions on biomedical circuits and systems*, vol. 11, no. 6, pp. 1366–1376, 2017.

[31] D. Szarowski, M. Andersen, S. Retterer, A. Spence, M. Isaacson, H. Craighead, J. Turner, and W. Shain, "Brain responses to micro-machined silicon devices," *Brain research*, vol. 983, no. 1-2, pp. 23–35, 2003.

[32] O. Veiseh, J. C. Doloff, M. Ma, A. J. Vegas, H. H. Tam, A. R. Bader, J. Li, E. Langan, J. Wyckoff, W. S. Loo *et al.*, "Size-and shape-dependent foreign body immune response to materials implanted in rodents and non-human primates," *Nature materials*, vol. 14, no. 6, p. 643, 2015.

[33] A. Khalifa, J. Zhang, M. Leistner, and R. Etienne-Cummings, "A compact, low-power, fully analog implantable microstimulator," *2016 IEEE International Symposium on Circuits and Systems (ISCAS)*, pp. 2435–2438, 2016.

[34] A. Khalifa, Y. Karimi, Q. Wang, S. Garikapati, W. Montlouis, M. StanaÄeviÄ, N. Thakor, and R. Etienne-Cummings, “The microbead: A highly miniaturized wirelessly powered implantable neural stimulating system,” *IEEE Transactions on Biomedical Circuits and Systems*, vol. 12, no. 3, pp. 521–531, June 2018.

[35] A. Khalifa, Y. Karimi, Q. Wang, E. Greenwald, S. Chiu, M. Stanaćević, N. Thakor, and R. Etienne-Cummings, “In-vivo tests of an inductively powered miniaturized neural stimulator,” *2017 IEEE International Symposium on Circuits and Systems (ISCAS)*, pp. 1–4, 2017.

[36] Y. Karimi, A. Khalifa, M. Stanaćević, and R. Etienne-Cummings, “Coil array design methods for maximizing power transfer to miniaturized on-chip coil,” *IEEE Biomedical Circuits and Systems Conference (BioCAS)*, 2017.

[37] A. Khalifa, Y. Karimi, Y. Huang, M. StanaÄevic, and R. Etienne-Cummings, “The challenges of designing an inductively coupled power link for ÎŒm-sized on-chip coils,” in *2018 IEEE Biomedical Circuits and Systems Conference (BioCAS)*. IEEE, 2018, pp. 1–4.

[38] A. Khalifa, Y. Karimi, M. Stanaćević, and R. Etienne-Cummings, “Novel integration and packaging concepts of highly miniaturized inductively powered neural implants,” *Proceedings of the 39th IEEE Engineering in Medicine and Biology Society (EMBC)*, pp. 234–237, 2017.

[39] S. Kerzenmacher, J. Ducrée, R. Zengerle, and F. Von Stetten, “Energy harvesting by implantable abiotically catalyzed glucose fuel cells,” *Journal of Power Sources*, vol. 182, no. 1, pp. 1–17, 2008.

[40] R. Venkatasubramanian, C. Watkins, D. Stokes, J. Posthill, and C. Caylor, “Energy harvesting for electronics with thermoelectric devices using nanoscale materials,” in *Electron Devices Meeting, 2007. IEDM 2007. IEEE International*. IEEE, 2007, pp. 367–370.

[41] J. Charthad, M. J. Weber, T. C. Chang, and A. Arbabian, “A mm-sized implantable medical device (imd) with ultrasonic power transfer and a hybrid bi-directional data link,” *IEEE Journal of Solid-State Circuits*, vol. 50, no. 8, pp. 1741–1753, 2015.

[42] H. Basaeri, D. B. Christensen, and S. Roundy, “A review of acoustic power transfer for bio-medical implants,” *Smart Materials and Structures*, vol. 25, no. 12, p. 123001, 2016.

[43] A. S. Poon, S. O’Driscoll, and T. H. Meng, “Optimal frequency for wireless power transmission into dispersive tissue,” *IEEE Transactions on Antennas and Propagation*, vol. 58, no. 5, pp. 1739–1750, 2010.

[44] M. Ettorre and A. Grbic, “A transponder-based, nonradiative wireless power transfer,” *IEEE Antennas and Wireless Propagation Letters*, vol. 11, pp. 1150–1153, 2012.

[45] M. A. Adeeb, A. B. Islam, M. R. Haider, F. S. Tulip, M. N. Ericson, and S. K. Islam, "An inductive link-based wireless power transfer system for biomedical applications," *Active and Passive Electronic Components*, vol. 2012, 2012.

[46] M. Zargham and P. G. Gulak, "Fully integrated on-chip coil in 0.13μm cmos for wireless power transfer through biological media," *IEEE transactions on biomedical circuits and systems*, vol. 9, no. 2, pp. 259–271, 2015.

[47] W. Biederman, D. J. Yeager, N. Narevsky, A. C. Koralek, J. M. Carmena, E. Alon, and J. M. Rabaey, "A fully-integrated, miniaturized (0.125 mm^2) 10.5 μw wireless neural sensor," *IEEE Journal of Solid-State Circuits*, vol. 48, no. 4, pp. 960–970, 2013.

[48] P. Feng, T. G. Constandinou, P. Yeon, and M. Ghovanloo, "Millimeter-scale integrated and wirewound coils for powering implantable neural microsystems," in *Biomedical Circuits and Systems Conference (BioCAS), 2017 IEEE.* IEEE, 2017, pp. 1–4.

[49] M. Zargham and P. G. Gulak, "Maximum achievable efficiency in near-field coupled power-transfer systems," *IEEE Transactions on Biomedical Circuits and Systems*, vol. 6, no. 3, pp. 228–245, 2012.

[50] L. Mcilvoy, "Comparison of brain temperature to core temperature: a review of the literature," *Journal of Neuroscience Nursing*, vol. 36, no. 1, p. 23, 2004.

[51] I. Schoen and P. Fromherz, "Extracellular stimulation of mammalian neurons through repetitive activation of na channels by weak capacitive currents on a silicon chip," *Journal of neurophysiology*, vol. 100, no. 1, pp. 346–357, 2008, pmid:18463183.

[52] C. Kim, S. Ha, A. Akinin, J. Park, R. Kubendran, H. Wang, P. P. Mercier, and G. Cauwenberghs, "Design of miniaturized wireless power receivers for mm-sized implants," in *Custom Integrated Circuits Conference (CICC), 2017 IEEE.* IEEE, 2017, pp. 1–8.

[53] X. Chen, W. G. Yeoh, Y. B. Choi, H. Li, and R. Singh, "A 2.45-ghz near-field rfid system with passive on-chip antenna tags," *IEEE Transactions on Microwave Theory and Techniques*, vol. 56, no. 6, pp. 1397–1404, 2008.

[54] V. W. Leung, J. Lee, S. Li, S. Yu, C. Kilfovle, L. Larson, A. Nurmikko, and F. Laiwalla, "A cmos distributed sensor system for high-density wireless neural implants for brain-machine interfaces," in *ESSCIRC 2018-IEEE 44th European Solid State Circuits Conference (ESSCIRC).* IEEE, 2018, pp. 230–233.

[55] N.-C. Kuo, B. Zhao, and A. M. Niknejad, "Equation-based optimization for inductive power transfer to a miniature cmos rectenna," *IEEE Transactions on Microwave Theory and Techniques*, vol. 66, no. 5, pp. 2393–2408, 2018.

[56] R. Gerwig, K. Fuchsberger, B. Schroeppel, G. S. Link, G. Heusel, U. Kraushaar, W. Schuhmann, A. Stett, and M. Stelzle, "Pedotcnt composite microelectrodes for

recording and electrostimulation applications: Fabrication, morphology, and electrical properties," *Frontiers in neuroengineering*, vol. 5, p. 8, 2012.

[57] E. Castagnola, A. Ansaldo, E. Maggiolini, T. Ius, M. Skrap, D. Ricci, and L. Fadiga, "Smaller, softer, lower-impedance electrodes for human neuroprosthesis: a pragmatic approach," *Frontiers in neuroengineering*, vol. 7, p. 8, 2014.

[58] H. Fang, J. Zhao, K. J. Yu, E. Song, A. B. Farimani, C.-H. Chiang, X. Jin, Y. Xue, D. Xu, and W. Du, "Ultrathin, transferred layers of thermally grown silicon dioxide as biofluid barriers for biointegrated flexible electronic systems," *Proceedings of the National Academy of Sciences*, vol. 113, no. 42, pp. 11 682–11 687, 2016, pmid:27791052.

[59] X. T. Cui and D. D. Zhou, "Poly (3, 4-ethylenedioxythiophene) for chronic neural stimulation," *IEEE Transactions on Neural Systems and Rehabilitation Engineering*, vol. 15, no. 4, pp. 502–508, 2007.

[60] E. Greenwald, C. Maier, Q. Wang, R. Beaulieu, R. Etienne-Cummings, G. Cauwenberghs, and N. Thakor, "A cmos current steering neurostimulation array with integrated dac calibration and charge balancing," *IEEE transactions on biomedical circuits and systems*, vol. 11, no. 2, pp. 324–335, 2017.

[61] H. Lyu, J. Wang, J.-H. La, J. M. Chung, and A. Babakhani, "An energy-efficient wirelessly powered millimeter-scale neurostimulator implant based on systematic

codesign of an inductive loop antenna and a custom rectifier," *IEEE transactions on biomedical circuits and systems*, no. 99, pp. 1–13, 2018.

[62] Y. Tanabe, J. S. Ho, J. Liu, S.-Y. Liao, Z. Zhen, S. Hsu, C. Shuto, Z.-Y. Zhu, A. Ma, C. Vassos *et al.*, "High-performance wireless powering for peripheral nerve neuromodulation systems," *PloS one*, vol. 12, no. 10, p. e0186698, 2017.

[63] A. Wickens, B. Avants, N. Verma, E. Lewis, J. C. Chen, A. K. Feldman, S. Dutta, J. Chu, J. O'Malley, M. Beierlein *et al.*, "Magnetoelectric materials for miniature, wireless neural stimulation at therapeutic frequencies," *bioRxiv*, p. 461855, 2018.

[64] K. L. Montgomery, A. J. Yeh, J. S. Ho, V. Tsao, S. M. Iyer, L. Grosenick, E. A. Ferenczi, Y. Tanabe, K. Deisseroth, S. L. Delp *et al.*, "Wirelessly powered, fully internal optogenetics for brain, spinal and peripheral circuits in mice," *Nature methods*, vol. 12, no. 10, p. 969, 2015.

[65] S.-H. Cho, N. Xue, L. Cauller, W. Rosellini, and J.-B. Lee, "A su-8-based fully integrated biocompatible inductively powered wireless neurostimulator," *Journal of Microelectromechanical Systems*, vol. 22, no. 1, pp. 170–176, 2013.

[66] J. Zhang, S. Mitra, Y. Suo, A. Cheng, T. Xiong, F. Michon, M. Welkenhuysen, F. Kloosterman, P. S. Chin, S. Hsiao *et al.*, "A closed-loop compressive-sensing-based neural recording system," *Journal of neural engineering*, vol. 12, no. 3, p. 036005, 2015.

[67] K. A. Ng and Y. P. Xu, “A compact, low input capacitance neural recording amplifier with cin/gain of 20ff. v/v,” in *Biomedical Circuits and Systems Conference (BioCAS), 2012 IEEE.* IEEE, 2012, pp. 328–331.

[68] P. H. Cole, D. C. Ranasinghe, and B. Jamali, “Coupling relations in rfid systems ii: practical performance measurements,” in *Auto-ID Center workshop*, 2003.

[69] B. Zhao, N.-C. Kuo, and A. M. Niknejad, “A gain boosting array technique for weakly-coupled wireless power transfer,” *IEEE Transactions on Power Electronics*, 2016.

[70] G. Yang, M. R. V. Moghadam, and R. Zhang, “Magnetic beamforming for wireless power transfer,” pp. 3936–3940, 2016.

[71] A. Ludwig, C. D. Sarris, and G. V. Eleftheriades, “Near-field antenna arrays for steerable sub-wavelength magnetic-field beams,” *IEEE Transactions on Antennas and Propagation*, vol. 62, no. 7, pp. 3543–3556, 2014.

[72] S. Stanslaski, P. Afshar, P. Cong, J. Giftakis, P. Stypulkowski, D. Carlson, D. Linde, D. Ullestad, A.-T. Avestruz, and T. Denison, “Design and validation of a fully implantable, chronic, closed-loop neuromodulation device with concurrent sensing and stimulation,” *IEEE Transactions on Neural Systems and Rehabilitation Engineering*, vol. 20, no. 4, pp. 410–421, 2012.

[73] W.-M. Chen, H. Chiueh, T.-J. Chen, C.-L. Ho, C. Jeng, M.-D. Ker, C.-Y. Lin, Y.-C. Huang, C.-W. Chou, T.-Y. Fan *et al.*, "A fully integrated 8-channel closed-loop neural-prosthetic cmos soc for real-time epileptic seizure control," *IEEE journal of solid-state circuits*, vol. 49, no. 1, pp. 232–247, 2014.

[74] O. Tabata, R. Asahi, H. Funabashi, K. Shimaoka, and S. Sugiyama, "Anisotropic etching of silicon in tmah solutions," *Sensors and Actuators A: Physical*, vol. 34, no. 1, pp. 51–57, 1992.

[75] J. P. Icenhower and P. M. Dove, "The dissolution kinetics of amorphous silica into sodium chloride solutions: effects of temperature and ionic strength," *Geochimica et Cosmochimica Acta*, vol. 64, no. 24, pp. 4193–4203, 2000.

Vita

Adam Khalifa received the B.S and MPhil degrees in electronic and computer engineering from Hong Kong University of Science and Technology, Hong Kong, China, in 2011 and 2013, respectively. He enrolled in the Ph.D program at Johns Hopkins University in 2014. His research interests include low power mixed-signal CMOS circuit design for neural interfaces, wireless power transfer systems, microfabricated electrodes and packaging of implantable systems. In March 2019, Adam will be working as a Research Fellow in the Department of Neurology at Massachusetts General Hospital and Harvard Medical School.